

## Sinking Yangon

Detection of subsidence caused by groundwater extraction using SAR interferometry and PSI time-series analysis for Sentinel-1 data

T. (Teije) van der Horst



### **On the cover**

The cover shows an image looking not to different from an oil spill, but it is actually the visual representation an interferogram over the city Yangon. The coloured values relate to the phase-difference between two radar acquisitions and the grey values indicate the multiplication of their amplitudes. The interferogram was calculated using images that were acquired on *February 19<sup>th</sup>, 2016* and *March 14<sup>th</sup>, 2016* by the Sentinel-1 satellite.



# Sinking Yangon

Detection of subsidence caused by groundwater extraction using SAR interferometry and a PSI time-series analysis for Sentinel-1 data

by

T. van der Horst

to obtain the degree of Master of Science  
at the Delft University of Technology, and the National University of Singapore,  
to be defended publicly on Friday February 17<sup>th</sup>, 2017 at 09:00 a.m. (GMT+1)

Student number: 4115104  
Project duration: April 4, 2016 – February 17, 2017  
Thesis committee: Dr. ir. M. M. Rutten, TU Delft, Water Resource Management  
Prof. dr. ir. N.C. van de Giesen, TU Delft, Water Resource Management  
Prof. dr. ir. R.F. Hanssen, TU Delft, Geodesy and Satellite Earth Observation  
Dr. ir. Pat Yeh J.F., NUS, Department of Civil and Environmental Engineering  
Ir. G. Mulder, TU Delft, Geoscience and Remote Sensing

An electronic version of this thesis is available at <http://repository.tudelft.nl/>.



# Contents

<b>Preface</b>	<b>vii</b>
<b>Abstract</b>	<b>ix</b>
<b>Nomenclature</b>	<b>xi</b>
<b>1 Introduction</b>	<b>1</b>
1.1 Research motivation . . . . .	1
1.2 Interferometric SAR . . . . .	2
1.3 Current knowledge on subsidence in Yangon . . . . .	2
1.4 Aim of this research . . . . .	2
1.5 Thesis outline and guides for reading . . . . .	3
<b>2 Myanmar and Yangon</b>	<b>5</b>
2.1 Myanmar . . . . .	5
2.2 Yangon City . . . . .	6
2.2.1 Geology and geography . . . . .	7
2.2.2 Climate . . . . .	8
2.2.3 Water resources . . . . .	9
2.2.4 City expansion . . . . .	9
<b>3 Radar Interferometry</b>	<b>13</b>
3.1 Imaging radar: SAR . . . . .	13
3.2 Radar interferometry: InSAR . . . . .	14
3.3 Persistent Scatterers . . . . .	16
3.4 Unwrapping . . . . .	17
<b>4 Materials and Methods</b>	<b>19</b>
4.1 Materials . . . . .	19
4.1.1 SAR data selection . . . . .	19
4.1.2 Orbital information . . . . .	20
4.1.3 Digital Elevation Model . . . . .	20
4.1.4 Doris . . . . .	20
4.1.5 StaMPS . . . . .	20
4.1.6 SNAPHU . . . . .	21
4.1.7 Interface . . . . .	21
4.2 Methods . . . . .	21
4.2.1 InSAR processing using Doris . . . . .	21
4.2.2 PSI processing with StaMPS . . . . .	24
4.2.3 Decomposition . . . . .	25
4.2.4 Groundwater extraction analysis. . . . .	26
4.2.5 Water demand survey . . . . .	26
<b>5 Results</b>	<b>29</b>
5.1 Line-of-sight velocity . . . . .	29
5.2 Decomposition . . . . .	33
5.3 Ground water extraction . . . . .	35

---

<b>6 Discussion</b>	<b>41</b>
6.1 S1 processing output . . . . .	41
6.2 PSI and decomposition assessment . . . . .	41
6.3 Fieldwork validation . . . . .	43
6.4 Groundwater extraction analysis . . . . .	45
6.5 Correlation of subsidence and groundwater extraction . . . . .	45
6.6 Qualitative analysis on the measured subsidence . . . . .	46
<b>7 Conclusions and recommendations</b>	<b>51</b>
<b>References</b>	<b>53</b>
<b>A Short recent history of Myanmar</b>	<b>57</b>
<b>B Maps of Yangon and Myanmar</b>	<b>59</b>
<b>C Pre study on subsidence in Yangon</b>	<b>61</b>
<b>D Additional PSI results</b>	<b>69</b>
<b>E Additional decomposition results</b>	<b>75</b>
<b>F Water Demand Survey</b>	<b>77</b>

# Preface

This thesis is the product of several months of research in the final stage of the double degree Hydraulic Engineering and Water Resources Management at Delft University of Technology and the National University of Singapore. Although Water Resource Management is represented in this thesis, the Hydraulic Engineering was substituted by remote sensing which covered the majority of my thesis work. This derived from my curiosity for this specific subject which I will introduce briefly.

Myanmar is currently experiencing rapid transformations while adjusting to recent democratic reforms. Because of the relatively unspoiled nature of the country, relative to its surroundings, any contribution that leads to possible sustainable development is worth the effort. Moreover, contributions are worth their while as insight gathered by research is often new and useful for this particular area. The specific point of interest lies in subsidence due to groundwater extraction which is found in many delta areas and cities in South-East Asia. The original plan was to focus on the Irrawaddy delta area and the Yangon region, but quick evaluation showed that this turned out to be more suitable for a PhD research than a master's thesis because of the complexity, size, data availability and the inability to perform measurements using InSAR in the delta (at this point in time). These were some of the considerations why this thesis was directed towards an assessment on Yangon city.

The space-geodetic technique -InSAR- presents the ability to do large scale surface deformation measurements with millimeter accuracy from nearly 800 km out in space using radio detection and ranging (radar) imagery. This subject was completely new for me and I was quite happy to be introduced to it. The opportunity to gain knowledge in an unexplored and quite abstruse field of research does not present itself often. The master's thesis is suitable for such an opportunity as a little extra time can be spend on stepping out of the comfort zone and diving into the unknown.

One special feature of this research was working with the Sentinel-1 data for interferometric processing. For this, the beta version of the Doris software package, developed at the TU Delft, was used. This software is not yet available for the scientific community, but I was allowed to make use of it for testing its functionality. This was both exciting and frustrating, for it allowed me to use state of the art technology while also having to deal with unexpected software problems.

I especially take great pride in extracting useful information from the interferograms using the time-series algorithm StaMPS. One and a half month I spend on writing Python and bash scripts that enabled for this post-processing step. This was necessary as StaMPS was not yet configured to work with Sentinel-1 interferograms since it relies on InSAR processors such as Doris. This time I spend coding felt as non-productive, especially since I did not yet know if it would possibly work or not. Fortunately, this was not a wasted effort as I eventually got it to work properly. Moreover, through this I was able to produce some nice results.

I am grateful to all those who supported me during this research. First of all, the members of my thesis committee, who were of significant importance. Many thanks to Martine Rutten and Nick van de Giesen, who provided me with this interesting subject in the first place and also allowed me to work in a completely new area of expertise. My sincerest gratitude goes out to Ramon Hanssen, who not only inspired me with his lectures on radar interferometry, but also took much of his valuable time to personally assist me in times of need. I really appreciate the hands-on support I received from Gert Mulder whose help proved to be indispensable. His contributions, together with all his predecessors, to the Doris software package are of great value to the scientific community. One more special thanks goes out to Martine who, amongst other thing, manages to guide countless students interested in combining water management and/or other disciplines in developing areas of South-East Asia without compromising in time for daily supervision.

This research also benefited greatly from contributions of several others who helped me during my graduation. I therefore thank Joana Martins for teaching me the StaMPS software basics, which could have taken me ages to figure out. Moreover, I appreciate the nice conversations we had. Furthermore I would like to thank Freek van Leijen for helping me set-up with the processing part. The generation of the DEM and set up of the automatic Sentinel download were real time savers. In addition, many thanks to Sami Samiei-Esfahany who was kind enough to help me interpret some of the results I could not quite yet understand. I would also like to thank Winmin Oo who supplied me with the dataset on YCDC extraction wells, something that I could not have obtained on my own. I have appreciated working together at both of our subjects. In the final stage, even after handing in my draft thesis, I received some photos from Boy-Santhos van der Sterre, who was residing in Myanmar at the time. He took it upon him to go on fieldwork to the severest subsiding area in search for signs. I want to thank him for taking a day to supply me with some very helpful visuals.

My thesis benefited incredibly by careful reading and reviewing of my work. I would hereby like to thank the members of my assessment committee for their critical review and helpful remarks. I would also like to thank Dorien Lugt and Lexy Ratering Arntz for their incredible helpful suggestions. The perfection of the academic English can be contributed to Odile Smith and Diane Butterman. All of you have carried this thesis to a higher level.

This research would not have been possible without the following tools and datasets. The radar data and orbital information used in this research was provided by the European Space Agency (ESA). The image catalog tool from SkyGeo was used to select all available data. The administrative boundaries and several other useful map layers were obtained from the Myanmar Information Management Unit (MIMU). The digital elevation map were obtained from the National Aeronautics and Space Administration (NASA). The processing software package for Sentinel-1 data, Doris, was provided by the TU Delft. The StaMPS software for time-series analysis is provided by the University of Leeds, although it was made with contributions from other institutions. Various scripts, analysis and visualization tools have been used or developed with Python, Matlab and ArcGIS. Finally this document has been typeset using  $\LaTeX$ . Except for the academic licenses for Matlab and ArcGIS, all data and software were used free of charge.

Aside from contributions obtained from all stated above, the pleasure in graduating is highly contributed to all the students from 4.84. The atmosphere in this rapidly changing collection of students in this room has always been very positive, both inside and outside the University. Moreover, intensive collaboration really makes for a productive environment through both content wise, process wise, and emotional support from students who are all experiencing the same phases in their graduation.

I would very much like to thank my girlfriend, Odile, for her unconditional love and support during my studies. She encouraged me to always reach for the sky (which often resulted in less time together). Especially during my time abroad, which took over a major part of my masters degree, there were some difficult times to overcome. Lastly, I would like to thank my parents for their moral and financial support which made studying a whole lot more comfortable.

*T. van der Horst  
Delft, 3<sup>rd</sup> February, 2017*

# Abstract

Inhabitants and ecosystems in delta areas are becoming increasingly vulnerable to the effects of subsidence, triggered both by natural causes and anthropogenic causes. Yangon is a city in the Irrawaddy delta in Myanmar where little is known about the true extent of this hazard, while its effects can potentially harm millions of its inhabitants. The aim of this research was, therefore, to assess if any subsidence is occurring, and to determine if groundwater extraction could be the cause of it. The city Yangon has a large urban extent and is expanding rapidly towards the north, west and east. In the current water supply system, nearly half of the domestic water use is supplied from reservoirs managed by the city council while the other half is obtained by other means. From the latter group, close to 80% extracts this water from aquifers beneath their home. This amounts to two million inhabitants of Yangon extracting their domestic water from the subsoil, that is excluding industrial water use. To assess if subsidence is occurring, surface deformation measurements were performed using Synthetic Aperture Radar interferometry (InSAR) with data from the recently launched Sentinel-1. This technique relies on the calculation of phase differences between two imaging radar acquisitions which were ultimately related to differences in surface motion on an interval scale. The direct derivation of surface deformation from two radar acquisitions was limited by noise interference from atmospheric signals and the measuring of temporally-unstable land surface. To overcome these limitations, a persistent scatterer interferometry (PSI) algorithm was used that selects stable scattering pixels with low noise contributors from a stack of interferograms through which deformation could be extracted. Resulting from the InSAR and PSI analysis, this thesis presents remotely sensed surface-level displacement using InSAR with Sentinel-1 data. Ascending and descending SAR image stacks over Yangon were processed into interferograms with the InSAR processing software, Doris, and next, the time series and line-of-sight velocities of phase stable pixels were extracted using the PSI algorithm StaMPS. The line-of-sight velocities that were decomposed into vertical and horizontal motion, reveal that parts of the city are subsiding at rates over 9 cm/y. Currently, these values cannot be validated due to the unavailability of ground-based measurements, but the consistency in the independent acquisition tracks supports their quality. To relate the surface deformation with subsidence, the domestic extraction of groundwater was mapped on the townships of Yangon. This involved combining various data sources among which a survey on water demand which was performed specifically for the benefit of this research. Although the relation between subsidence and groundwater extraction is more complex than simply their co-occurrence, this method was chosen to get a first order estimate of their causal relation. Additionally, there was not enough information available to employ a more extensive or complex approach. Through mapping water extractions onto the townships of Yangon, extraction rates up to 9 mm/y were found. The spatial patterns of measured subsidence and estimated groundwater extraction do not correlate and therefore no indication for a causal relation between the two could be established. Future research should first be directed at identification of the mechanisms involved causing surface deformation. An extension on this research could be done with the suggested improvements on the extraction estimation, but assessing subsidence caused by groundwater pumping through a more extensive approach might be required. Though a relation between surface deformation and groundwater extraction is not established in this thesis, a recommendation is given to mitigate negative effects caused by groundwater pumping.



# Nomenclature

## List of Acronyms

<b>ALD</b>	Azimuth Look Direction
<b>APS</b>	Atmospheric Phase Screen
<b>AOE</b>	Atmosphere and Orbit Error
<b>csk</b>	COSMO-Skymed
<b>CPOD</b>	Copernicus Precise Orbit Determination
<b>d-InSAR</b>	differential InSAR
<b>DEM</b>	Digital Elevation Model
<b>Doris</b>	Delft object-oriented radar interferometric software
<b>DS</b>	Distributed scatterers
<b>Envisat</b>	Environmental Satellite
<b>ERS-1</b>	European remote sensing satellite 1
<b>ERS-2</b>	European remote sensing satellite 2
<b>ESA</b>	European Space Agency
<b>ESD</b>	Enhanced Spectral Diversity
<b>GPS</b>	Generic Mapping Tools
<b>GPS</b>	Global Positioning System
<b>InSAR</b>	Interferometric Synthetic Aperture Radar
<b>IW</b>	Interferometric Wide Swath
<b>LOS</b>	line-of-sight
<b>MSL</b>	mean sea level
<b>NLD</b>	National League for Democracy
<b>PS</b>	Persistent Scatterers
<b>PSI</b>	Persistent Scatterer InSAR
<b>radar</b>	radio detection and ranging
<b>Rsat-2</b>	Radar satellite 2
<b>SAR</b>	Synthetic Aperture Radar
<b>S1A</b>	Sentinel-1A
<b>S1B</b>	Sentinel-1B
<b>S1</b>	Sentinel-1
<b>SCLA</b>	Spatially-Correlated Look Angle
<b>SLC</b>	Single Look Complex
<b>SLORC</b>	State Law and Order Restoration Council
<b>SNAP</b>	Sentinel Application Platform
<b>SNAPHU</b>	Statistical-Cost, Network-Flow Algorithm for Phase Unwrapping
<b>SRTM3</b>	Shuttle Radar Topography Mission 3''
<b>StaMPS</b>	Stanford Method for Persistent Scatterers
<b>SULA</b>	Spatially-Uncorrelated Look Angle
<b>TOPS</b>	Terrain Observation by Progressive Scans
<b>TU Delft</b>	Delft University of Technology
<b>USGS</b>	United States Geological Survey
<b>YCDC</b>	Yangon City Development Committee

## Glossary

<b>Atmospheric Phase Screen</b>	Atmospheric phase delays; resulting mainly from temporal and or spatial changes in humidity
<b>Azimuth</b>	Used to indicate the direction parallel to the flight direction of the satellite
<b>Baseline, spatial</b>	Projection of the distance perpendicular to repeat-pass orbits, see also Fig. 3.2
<b>Coherence, interferometric</b>	Measure of correlation with a value ranging from 0.0 to 1.0 serving as a quality indicator of an interferogram
<b>Coherent, imaging</b>	An imaging system that preserves the phase of the received signal
<b>Fringe</b>	complete phase cycle of one wavelength in the spatial domain of an interferogram
<b>Incidence angle</b>	The angle defined by the incoming radar beam vector and the normal vertical to the global surface
<b>In-phase</b>	The signal component that has the same phase as the reference frequency, in complex representation the real number and often represented by the letter <i>I</i>
<b>Look angle</b>	See 'Off nadir angle'
<b>Nadir</b>	Nadir is a single point on the surface of the Earth directly below a sensor as it progresses along its line of flight
<b>Off nadir angle</b>	The angle defined by the nadir direction and outgoing radar beam. Also referred to as 'Look angle' or 'Elevation angle'
<b>Orbit</b>	The path of a satellite as it revolves around the Earth
<b>Parallel Baseline</b>	Difference in range from a point on the Earth's surface to the orbital tracks, see also Fig. 3.2
<b>Perpendicular Baseline</b>	Projection of the 'Baseline' onto the slant-range, see also Fig. 3.2
<b>Phasors</b>	phase vector, a complex number representing both a signal's amplitude and phase
<b>Range, distance</b>	line of sight distance between a radar system and each reflecting object (scatterer)
<b>Range, direction</b>	Used to indicate the direction perpendicular to the flight direction
<b>Repeat-pass, interferometry</b>	Configuration in which two radar images of the same area are acquired by the same antenna after a certain revisit time-interval. The alternative for repeat-pass is single pass in which two antennas are used simultaneously.
<b>Scatterer</b>	Object that reflect radiation back towards the satellite
<b>Sentinel-1</b>	The first of ESA's new fleet of satellites, carrying an advanced C-band SAR radar instrument. Sentinel-1 is a constellation of two satellites (S1a and S1b) orbiting 180° apart, covering the entire Earth every six days.
<b>Single Look Complex</b>	Compressed radar data in complex format containing amplitude and phase information at the largest possible ground geometry
<b>Swath</b>	Strip on the Earth's surface from which remotely sensed data is collected. The Swath width refers to the swath dimension in the direction perpendicular to the orbital motion
<b>Temporal baseline</b>	temporal separation of two acquisition
<b>Quadrature phase</b>	The signal component that is 90° out of phase with respect to the reference frequency, in complex representation the imaginary component and often represented by the letter <i>Q</i>
<b>Unwrapped, phase</b>	Phase value in the set of real numbers for which the $2\pi$ -moduli of the wrapped phase values have been resolved to form a continuous phase
<b>Wrapped, phase</b>	Principal value of the measured phase in the interval $(-\pi, \pi]$ or $[0, 2\pi)$ outside of which phase cannot be measured.

## List of Symbols and operators

$\lambda$	[m]	Wavelength
$\phi$	[rad]	Phase wrapped in $[-\pi, \pi)$
$\phi_I$	[rad]	Interferometric phase
$\phi_{flat}$	[rad]	'Flat Earth' phase
$\phi_{topo}$	[rad]	Topographic phase
$\phi_{defo}$	[rad]	Deformation phase
$\phi_{APS}$	[rad]	Atmospheric Phase Screen
$\phi_{scat}$	[rad]	Scattering phase (caused by different motions within cell)
$\phi_{noise}$	[rad]	Phase noise contributors
$\phi_r$	[rad]	Reference phase, incorporating both $\phi_{flat}$ and $\phi_{topo}$
$\psi$	[deg]	Off nadir angle
$r$	[m]	Slant range
$\theta$	[deg]	Incidence angle
$I$	[-]	Complex interferogram
$I_R$	[-]	Complex subtracted reference interferogram
$M$	[-]	Complex master image
$S$	[-]	Complex slave image
$R$	[-]	Complex reference image with $ R  = 1$
$B$	[m]	Baseline
$B_{\perp}$	[m]	Perpendicular Baseline
$B_{\parallel}$	[m]	Parallel Baseline
$H_p$	[m]	Topographic height
$D_A$	[-]	Amplitude dispersion index (Interferometric time-series)
$\sigma_A$	[-]	Amplitude standard deviation (Interferometric time-series)
$\mu_A$	[-]	Amplitude mean (Interferometric time-series)
$v_{LOS}$	[mm/y]	Line-of-sight surface velocity
$v_u$	[mm/y]	Up component of the surface velocity
$v_n$	[mm/y]	North component of the surface velocity
$v_e$	[mm/y]	East component of the surface velocity
$v_x$	[mm/y]	Local $x$ -component of the surface velocity in chosen direction $\gamma$
$v_y$	[mm/y]	Local $y$ -component of the surface velocity in a direction $\perp \gamma$
$\gamma$	[deg]	Horizontal deformation direction assumption
$P$	[-]	Population
$C_{yyyy}$	[%]	Coverage ratio of year 'yyyy'
$D$	[L/p/d]	Daily water demand per inhabitant
$f_{priv}$	[-]	Private groundwater extraction factor
$h_i$	[m]	Soil layer thickness
$C_s$	[-]	Coefficient of secondary settlement
$\Delta t$	[days]	time difference between change in effective stress
$\sigma_i$	[Pa]	Effective vertical soil stress
$\{.\}^*$		Complex conjugate
$Re(.)$		Real part of input
$Im(.)$		Imaginary part of input
$\arctan_2(\Re, \Im)$		Four-quadrant arctangent with real and imaginary input



# Introduction

All around the world major river deltas are sinking relative to the local mean sea level. On the one hand this is caused by local mean sea level rise in the order of a few millimetres per year. On the other hand the ground surface in delta regions is susceptible to subsidence as a result of both natural and human-induced causes (Syvitski, 2008). Natural causes for land subsidence include: sediment compaction, peat oxidation, and crustal motion (Higgins, 2015), which are often found to be in the same order of magnitude as sea level rise (Syvitski, 2008). Human-induced land subsidence is mainly caused by excessive groundwater extraction as a result of rapid urbanization or extraction of other resources. Human-induced subsidence can outpace sea-level rise by one (Syvitski, 2008) or in extreme cases even two orders of magnitude (Higgins, 2015). Among the problems that can arise as a result of land subsidence are an increased vulnerability to flooding and storm surges, (infra)structural failures, aquifer salinization and permanent geological deformation (Syvitski et al. 2009, Wang, Miao & Lu, 2013)

Water-based transportation and rich agricultural soils create an environment that is suitable for rapid economic growth and urbanization in delta areas (NASA, 2000). The level of human influence throughout this rapid urbanization requires detailed examination in order to prevent man-made disasters and irreparable damage being caused to the environment. This holds especially for river deltas since areas with compressible substrates, low gradients and large populations are particularly vulnerable (Higgins, 2015). Subsidence is a key contributing factor to flood risk from sea-level rise and extreme weather events and so it needs to be better evaluated, especially in areas with large exposed populations (Bally, 2012).

## 1.1. Research motivation

The Irrawaddy delta is an example of such a delta system that is in peril because sea level rise and accelerated soil compaction form a significant threat to the people living in it. As much as 1100 km<sup>2</sup> of the delta is located two meters below sea level while the storm-surge area covers up to as much as 15000 km<sup>2</sup> exposing over five million people in the city of Yangon alone (Syvitski et al., 2009). Subsidence geo-hazards are seldom managed and in most cases the symptoms are treated rather than the causes (Bally, 2012). This might also be the case for Myanmar where large political reforms recently took place and where coordination towards sustainable development is still in its early stages (RVO Netherlands, 2014).

The city of Yangon is of specific interest in connection with subsidence hazards as it satisfies many of the conditions that make an area prone to subsidence; it is situated in a delta area in Asia; there is rapid ongoing urbanization with a large expected population growth; large parts of the city have very low elevation; the soil layers consist of compressible substrates and groundwater is used by a significant part of its citizens (Chen et al., 2012). Moreover the risks of such hazards are most likely higher in Yangon than anywhere else in the country as the city is so densely populated and situated very close to the sea. Therefore the focus of this research will be directed towards the vulnerability to subsidence of the Yangon city in Myanmar, focusing on subsidence rates and their possible sources.

## 1.2. Interferometric SAR

Synthetic Aperture Radar (SAR) is an active microwave imaging system, which is capable of measuring the Earth's surface regardless of local cloud conditions. Space-based radar satellites have been continuously monitoring the Earth since the early 90's. An increasing number of satellites are available (WMO, 2016) which show many improvements over time in terms of resolution and the revisit time. Because of the coherent imaging technique used in SAR, the radiometric phase and amplitude are preserved during measurements.

The SAR satellites revisit each area after a number of days observing from a slightly different 'look angle'. This revisiting property ensures the interferometric configuration of the sensor allowing for radiometric calculations. Such a technique in which radio interferometry is performed using SAR satellites, is also known as Interferometric Synthetic Aperture Radar (InSAR) (Ferretti et al., 2007). The difference in radiometric phase between two acquisitions can ultimately be related to surface deformation.

The launch of Sentinel-1 (S1), as a successor to ERS-2 and Envisat, provides many new opportunities for monitoring land and ocean. The S1 mission is a two-satellite constellation with a 12-day repeat cycle of 175 orbits for each satellite. The Interferometric Wide Swath (IW) mode records an amazing 250 km swath width while maintaining a resolution of 5 x 20 m in terms of ground geometry. Even so, one of the most interesting features of this mission is the open and free data access as provided by Copernicus<sup>1</sup> (ESA, 2016).

## 1.3. Current knowledge on subsidence in Yangon

Subsidence is a typical geohazard for low elevated coastal areas and river basins, especially when densely populated (Bally, 2012). In many cases subsidence is only detected when the effects are already visible. It was only recently that the potential for hazards in the Irrawaddy delta was acknowledged, but the rates and extent of such hazards remain unknown (Higgins, 2015).

Only one previous study by Aobpaet et al. (2014) on surface displacement in the city of Yangon is known in which 15 ascending orbit Radar satellite 2 (Rsat-2) images were processed using a Persistent Scatterer InSAR (PSI) analysis. The report suggests that there were non-seismic activities causing vertical displacement rate differences up to roughly 12 cm/y with a likely source contributor to be groundwater extraction. Unfortunately there is a lack of validation of these values and the number of images for a time series analysis is also low since the recommended amount of images is usually around 25 (Hooper et al., 2007). These are reasons why the stated subsidence rates have to be interpreted with caution. Furthermore only ascending orbits are considered which makes the assumption that there is only vertical displacement questionable. Besides, Persistent Scatterers (PS) pixels that have poor connection to other scatterers are not rejected which seriously affects the quality of these individual points as they are likely to result in unwrapping errors. Virtually nothing is known in any other urban or rural area throughout the Irrawaddy delta.

## 1.4. Aim of this research

In this research, the aim is to assess whether any subsidence is currently occurring in Yangon, and to identify whether groundwater extraction is the main cause, if subsidence is detected. This research can provide insight into the degree of sustainability in relation to the extraction of georesources such as the groundwater in Yangon. Considerations in present and future policy regarding extraction of georesources are vital as most of the undesired effects resulting from subsidence are non-reversible and usually affect a large number of people. The goal of this research is to answer the following research question:

**Can InSAR be used for measuring subsidence in Yangon and is there a correlation between subsidence and groundwater extraction?**

---

<sup>1</sup>Copernicus is the European Programme for the establishment of a European capacity for Earth Observation for the support of a sustainable European information network.

To solve this research question, three sub-questions have to be answered to make the main question more transparent.

1. Can InSAR be applied for the area of Yangon?

A question that might seem trivial, but the answer to it is rather essential and location dependent. Data products need to be acquired over the area of interest, temporal stability in scattering objects is required for the technique to be successful and finally, a suitable InSAR processor is necessary for delivering the desired results.

2. Is it possible to extract surface deformation from the interferometric output?

In the ideal case where noise terms, such as atmosphere, are significantly smaller than deformation, the desired information can be derived from the interferograms directly. In the more general (not ideal) case, deformation needs to be derived using a more sophisticated approach often involving the processing of big stacks of data. This adds to the requirement for the amount of InSAR data products being available.

3. Where are significant amounts of water extracted from the ground?

In order for a correlation to be determined, the extraction of groundwater needs to be mapped on Yangon. Although the relation between groundwater extraction and subsidence is highly complex, their correlation can serve as a first order indicator to determine if they indeed have a causal relation. Especially the 'where' and 'how much' of groundwater extraction need to be addressed.

## 1.5. Thesis outline and guides for reading

In Chapter 2 the country Myanmar is introduced and an extensive description is given on Yangon concerning the points of interest relevant to this thesis. Those who are interested in reading about the ongoing change the country has recently gone through should refer to Appendix A. For readers not familiar with the concepts of radar interferometry and PSI time-series analysis, Chapter 3 will be of interest as it covers most of the basics necessary to comprehend the subsequent chapters. Be aware to check the glossary for unknown concepts, as most of them might be explained in there. Chapter 4 essentially consists of two parts: First, a list of used data and software will be presented in the materials section and finally, the methods section elaborates on how these materials were combined to extract the desired results. Many considerations of this chapter have been based on an unpublished pre-study which is included in Appendix C. The most important results regarding InSAR and the assessment on water extraction are presented in Chapter 5. Results less relevant for this research, but important for evaluation of the quality of the main results can be found in appendices D and E. Subsequently, the main topics of discussion that concern implications on the presented results and points of improvement will be discussed in Chapter 6. In conclusion, Chapter 7 will present brief answers to all of the research questions. Appendix B contains additional maps of digital elevation in Yangon and yearly average precipitation in Myanmar. The survey set-up and results from which the water demand was derived is included in Appendix F.



# 2

## Myanmar and Yangon

### 2.1. Myanmar

Officially “the Republic of the Union of Myanmar” is a country with the second largest land surface in south east Asia with an area over 670000 km<sup>2</sup> and a population that has grown to about 60 million people. Because of the recent political reforms, present day Myanmar is encountering rapid transformation in many sectors such as infrastructure, economy, and technology. Large investments in infrastructures are being made that will stimulate the economy in the near future. The official capital is Naypyidaw although in many parts of the world the old capital, Yangon (also known as Rangoon), is still considered as the capital. This is understandable as the city is home to the country’s largest population and even has one of the largest spatial extents of cities in South East Asia (Morley, 2013). Myanmar has transformed extensively over the past few years because of democratic reforms in 2011. If one wants to understand how the historic and current situation of Myanmar came to be, the short version of Myanmar’s recent history as provided in Appendix A might present some insight.

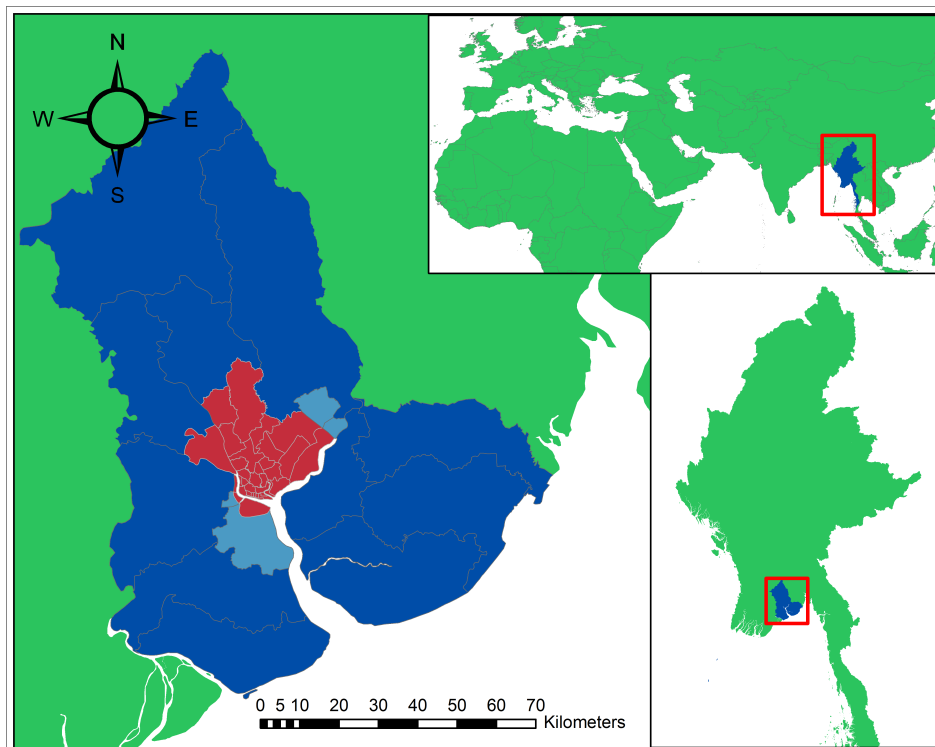


Fig. 2.1: Geographic location of Myanmar in the world (top-right), Yangon region in Myanmar (bottom-right) and in red the 33 townships of Yangon city within Yangon region highlighted in red (left).

Myanmar is located between 10 deg and 28 deg N, and 92 deg and 101 deg E, and is sandwiched between Thailand, Bangladesh, India and China as shown in Fig. 2.1. The country is trapped in between two foothills of the Himalaya Mountains with Hkakabo Razi as its highest point (5881 m) in the most northern part of the country. In between these two foothills is the catchment of the Irrawaddy river and its delta. Large parts of the Irrawaddy deltas are flat and below five meters in elevation as seen in Fig. 2.2. Yangon is situated on the eastern periphery of the delta.

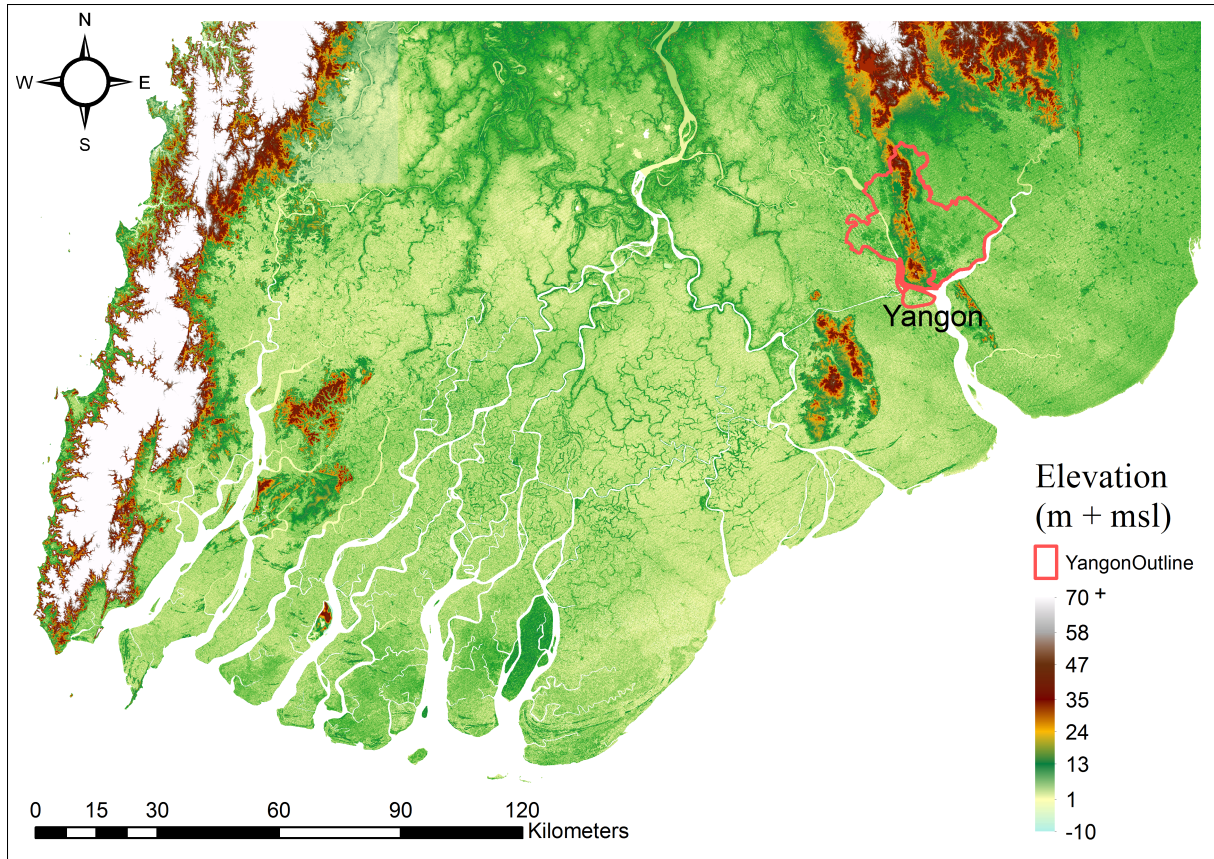


Fig. 2.2: Elevation profile of the Irrawaddy delta made with the SRTM-1" digital elevation model data that was created by NASA and was obtained through the USGS EarthExplorer.

Myanmar is situated in the monsoon region of Asia with its coastal regions receiving over 5000 mm/y. Annual rainfall in the delta region accounts for nearly 2500 mm while the average rainfall in the dry zone in central Myanmar is less than 1000 mm per year. The northern part of the country is the coolest area where 21 °C is the regional average compared to a maximum of 32 °C in the delta region.

There is large spatial and temporal variability in the precipitation levels as seen in Fig. B.2 that can be found in Appendix B. The largest amount of annual precipitation is observed between May and November with only very little precipitation after a rainy season. In view of the spatial distribution, there is an enormous amount that precipitates in the coastal regions of Myanmar with annual precipitation values reaching over 6 m. The Irrawaddy delta and the Yangon region annually receive up to 3 m of precipitation. The central part of the country receives the least precipitation with values ranging from 600 to 1100 mm annually.

## 2.2. Yangon City

Yangon region's capital, Yangon, the country's former capital, is currently home to more than 5.2 million people. The Yangon Region is subdivided into 4 districts and 44 townships, 33 of which are in Yangon city managed by Yangon City Development Committee (YCDC). A layout of the Yangon city townships with their population densities is shown in Fig. 2.3. For a map including all township names, refer to Fig. 5.13 and Table 5.1. The spatial extent of the city has increased to 600 km<sup>2</sup> (measured in 2008) and is still expanding to

the north and in east-west direction because of high population growth (YCDC & JICA, 2013). The city is very densely populated with an average of 8500 p/km<sup>2</sup> and local peaks up to 70000 p/km<sup>2</sup> (MIMU et al., 2014).

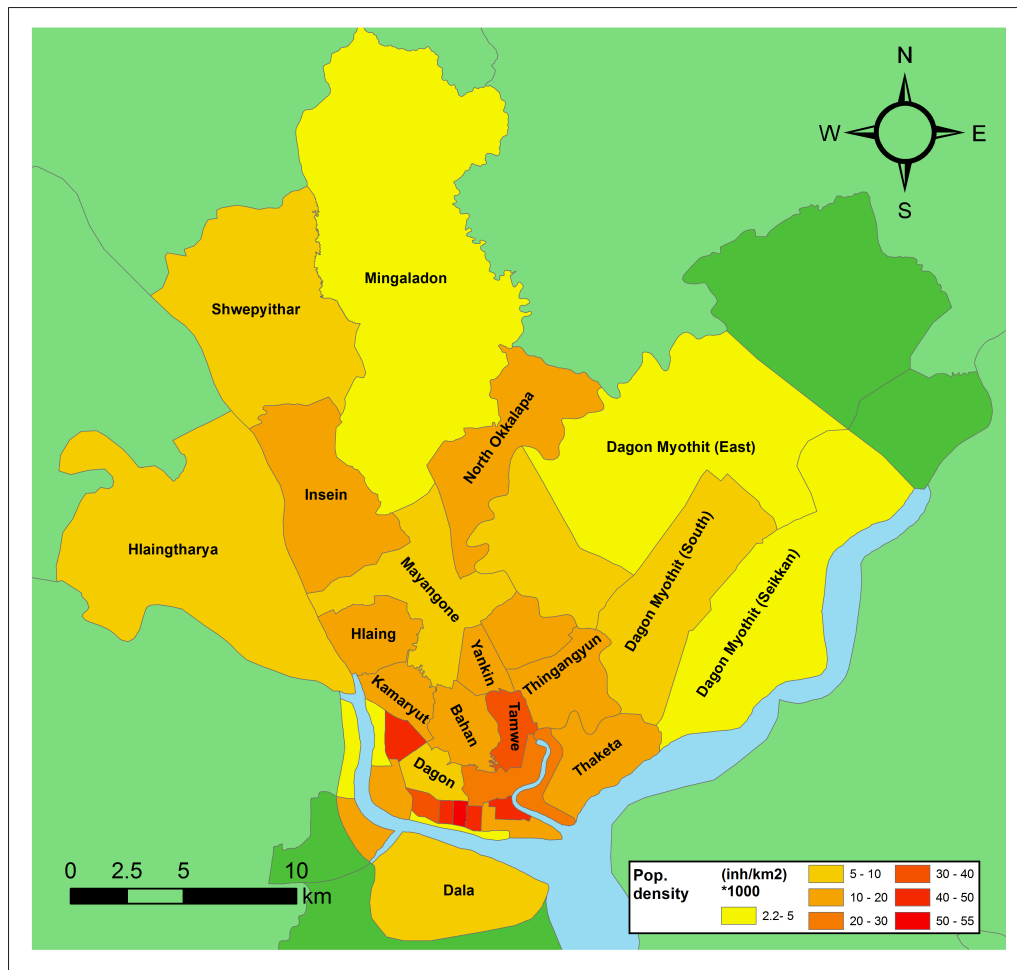


Fig. 2.3: 33 Townships of Yangon City with population density per township (MIMU et al., 2014). Only fitting township names are shown. For the names of all townships consult Fig. 5.13 and Table 5.1. Light blue areas belong to townships that have an ill defined city boundary.

### 2.2.1. Geology and geography

Not much is known about the geology of Yangon. A soil map of Yangon can be found in Fig. 2.4 showing basically two different types of soils that are found in and around the city: meadow alluvial soils and lateritic soils. Meadow alluvium is most commonly found in and around the city and has a silty clay loam texture and high nutrient content making it very suitable for a large range of agricultural products. Lateritic soils are found in the higher central and northern parts of Yangon and have formed the foundation on which the city has been built. The soil is rich in iron and iron oxide which gives its characteristic yellow or reddish brown colour (Ministry of Agriculture and Irrigation, 2013). Unfortunately no information is available regarding the different layers in the subsoil and their characteristics. The subsiding potential for both soil types greatly depends on these characteristics and therefore no qualitative description can be given.

The original settlement of Yangon was located on a ridge running from the north of the region to the upper side of the Yangon river located on the south side of the city, as seen in Appendix B Fig. B.1. This ridge has a height of approximately 30 m and is located almost entirely at the lateritic soil zone. The city has expanded from this ridge to the lower alluvial parts of the delta situated between 3 and 15 m above mean sea level (MSL).

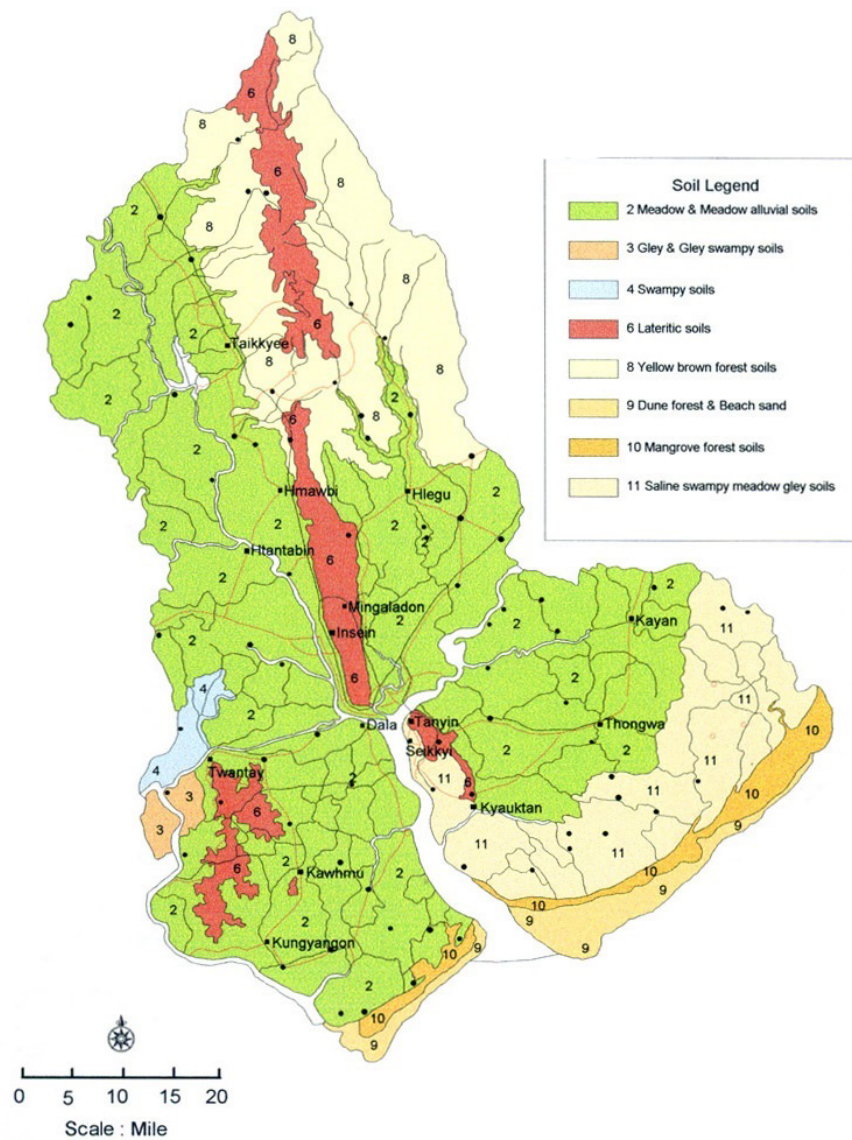


Fig. 2.4: The geology map of Yangon source: (Ministry of Agriculture and Irrigation, 2013).

### 2.2.2. Climate

Yangon has a tropical savanna climate with distinct wet and dry seasons of a relatively equal duration. Most of the annual rainfall occurs between May and October while very little is observed between November and April. The evaporation is much less than the precipitation and is most notoriously present in the dry season as both the temperature and the radiation are then higher. The monthly averaged values of precipitation, evaporation, temperature, wind speed, relative humidity and cloud cover are presented in Fig. 2.5. The presented data is derived from monthly data logged between 1984 and 2016 at the one and only weather station in the city, 'Kabaaye station'.

### 2.2.3. Water resources

Several sources report on the amount of water that is supplied to the population of Yangon. The number derived from these sources combined are shown in Fig. 2.6. The 'household survey' (YCDC & JICA, 2013) suggests that around 40 % is connected to the city's water supply managed by the Yangon City Development Committee (YCDC) while as much as 60 % is connected to this water supply (YCDC, 2014). Whichever is the case, a large part of the city is connected through non-YCDC supplied water and nearly 80 % of this group receives water from a personal or public groundwater well (YCDC, 2014). Nearly 10 % of the water that is supplied by the YCDC is extracted from groundwater sources through more than 440 tube wells, amounting to 90 000 m<sup>3</sup> daily. The amount of water extracted from personal tube wells could easily be ten times as much because of the large amount of personal wells, but unfortunately very little data is available on the exact numbers.

Table 2.1: Current and projected performance indicators of the Yangon water supply system (Mon, Htay, Tun & Aung, 2013).

Performance indicators	Target year		
	2013	2025	2040
Leakage rate	50%	25%	10%
Demand coverage	30%	60%	80%
Water consumption (L/cap/d)	135	160	180
Supply duration	8 hours	24 hours	24 hours
Water quality	Non-drinkable	Drinkable	Drinkable
Non-revenue	66%	35%	15%

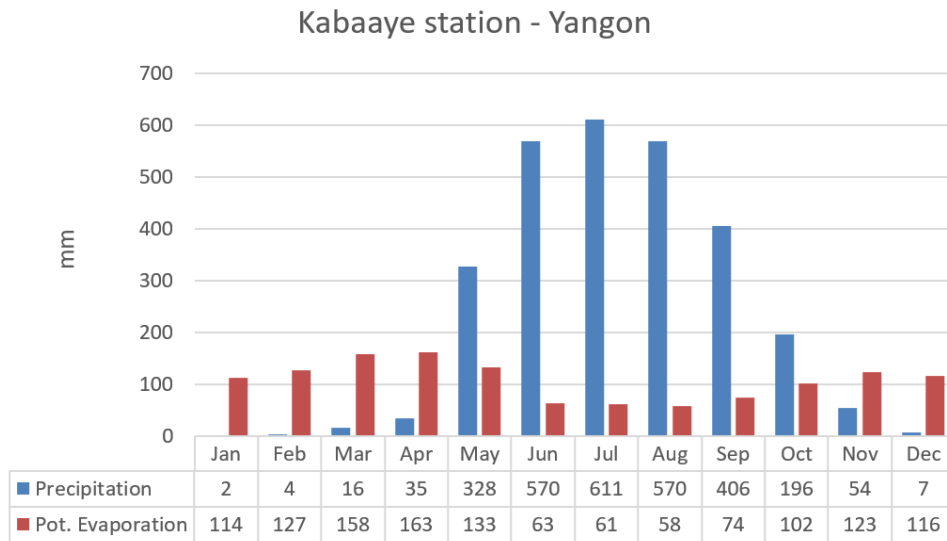
The YCDC has constructed a long-term plan for the management of water supply to the citizens of Yangon. Some target levels are stated in Table 2.1 which indicates the current state and projections for the future. A few remarkable numbers are worth mentioning from this table. Firstly, the enormous leakage rate of 50 % in the current supply system gives an indication of its physical state. Secondly, another demand coverage of only 30 % is displayed, which is even lower than the first two estimates stated at the begin of this section. Thirdly, current water consumption seems high and will continue to rise to 180 L/cap/d which is an increase of 1/3 of the current situation. Finally, the service level projections seem very ambitious and they need incredible investments in order to be achieved.

If the projected performance indicators are met, this will mean that most of non-YCDC wells can be replaced and groundwater usage will drop significantly, especially when personal wells are made superfluous. However, the ever growing population together with the need for considerable investments make this a rather challenging exercise without the financial aid of other countries. While the long-term plan for the management of water supply shows that there is a will to improve the sustainable use of groundwater, messages stating that high-rise buildings will have to continue the practice of digging for their own water (Minn, 2014) show otherwise. Such messages show that the current policy does not promote the projected performance indicators. Moreover, the dropping of the groundwater table and salinization of aquifers require more urgent action to prevent negative effects caused by them (Wyne Khin, 2016).

To summarize, the water supply to the inhabitants of Yangon is partially managed by the YCDC providing piped water from a series of reservoirs. Around 10 % of YCDC supplied water is extracted from the ground using wells. At locations with poor coverage by the YCDC managed supply, inhabitants often rely on private water supply. The amount extracted by private wells could be far greater than the extraction through YCDC wells, but there is a lack of accurate statistics on the private extraction. Projected performance indicators are ambitious, but do guarantee that Yangon will not rely on groundwater extraction once they are achieved.

### 2.2.4. City expansion

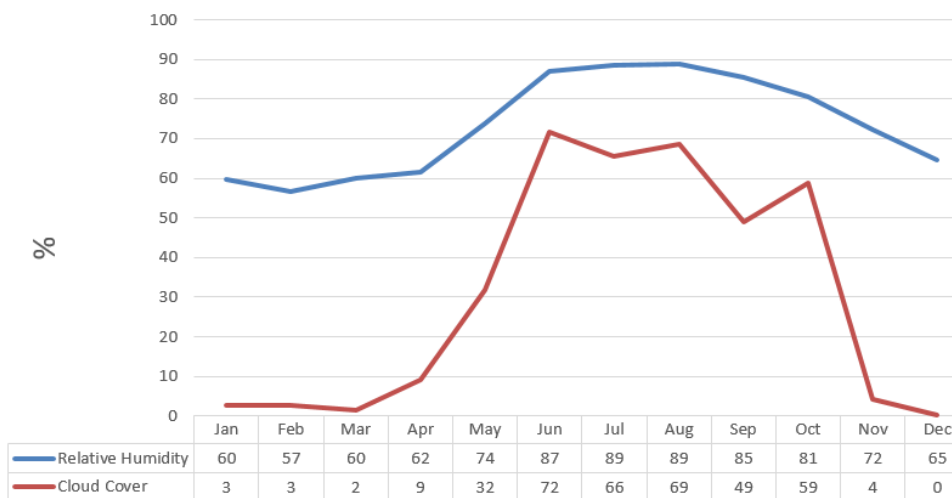
The population growth in the past decades resulted in a vast increment in urban area. Since the expansion of the city in 1983, both the amount of inhabitants and the size of the city have doubled and continue to increase rapidly (JICA, 2014a). Optical satellite images of Yangon city taken from 1984 onwards are presented in Fig. 2.7 clearly showing how the inner core of the city densifies, new townships arise in the east-west direction, and expansion towards the North intensifies.



(a) Long term monthly averaged precipitation and evaporation, values in mm/month



(b) Long term monthly averaged temperature in °C and wind speed in kn



(c) Long term monthly averaged relative humidity and cloud cover data

Fig. 2.5: Climatologic parameters of Kabaaye weather station, Yangon city. Source: Department of Meteorology and Hydrology, Myanmar.

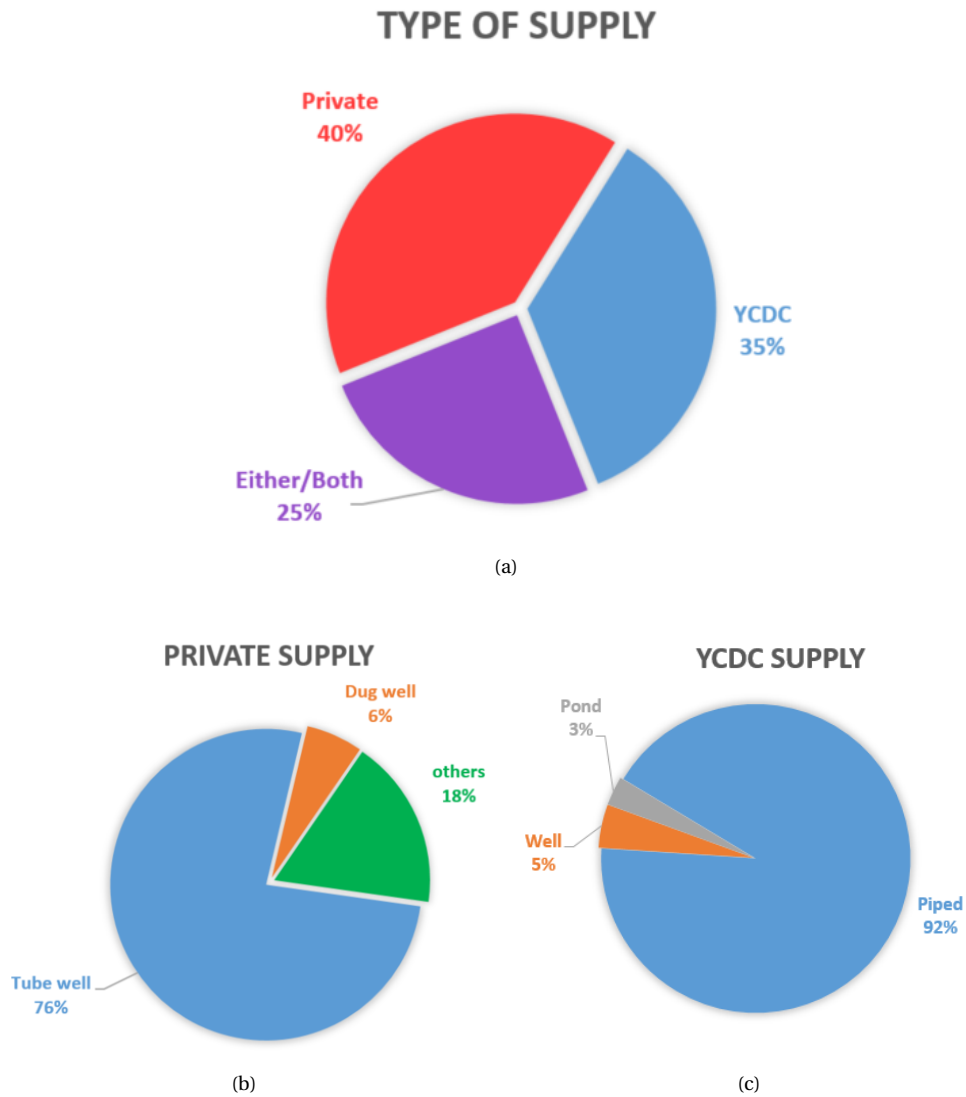


Fig. 2.6: Distribution of the source of water according to (YCDC & JICA, 2013; YCDC, 2014; Mon et al., 2013). The source of delivery distribution is shown in (a) with an uncertainty shown in purple. The type of water supply within the users that receive water from private sources or the YCDC is shown in (b) and (c) respectively. The main type of YCDC supply is piped reservoir water while private supply is mainly extracted from the ground.

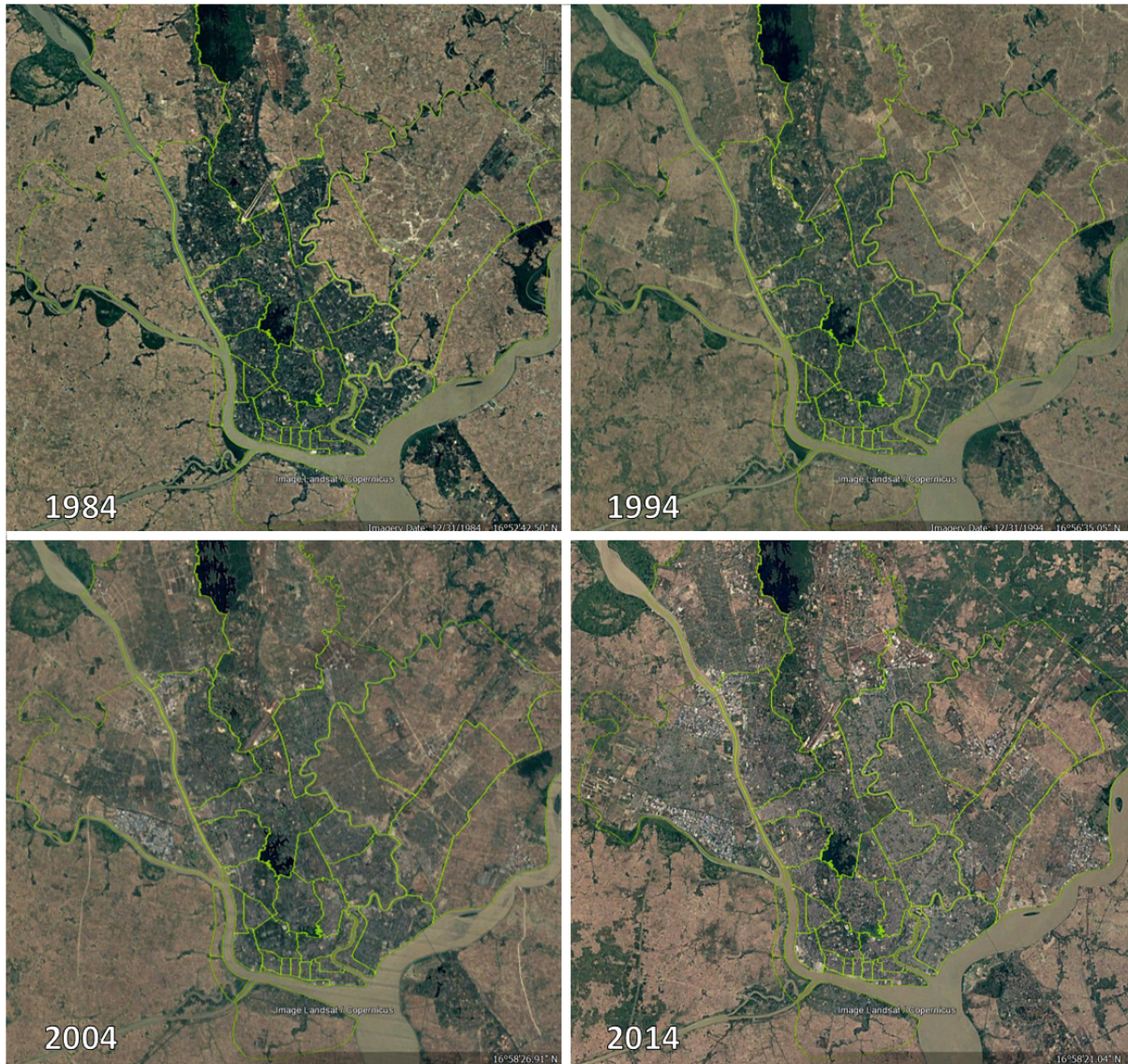


Fig. 2.7: Composite of four images showing historic optical space observations of Yangon city. The current township boundaries are highlighted in yellow. Source: Google Earth, retrieved on December 20<sup>th</sup>, 2016

# 3

## Radar Interferometry

A significant part of this research consists of using the InSAR technique for deformation monitoring. The technique utilizes radiometric phase differences between two radio detection and ranging (radar) satellite acquisitions for the assessment of surface deformation. The basic concepts of InSAR and interferogram formation will be explained in this chapter. Note that only repeat-pass interferometry will be discussed. For a detailed description of imaging radars and an in-depth explanation of radar interferometry, the reader is referred to (Hanssen, 2001).

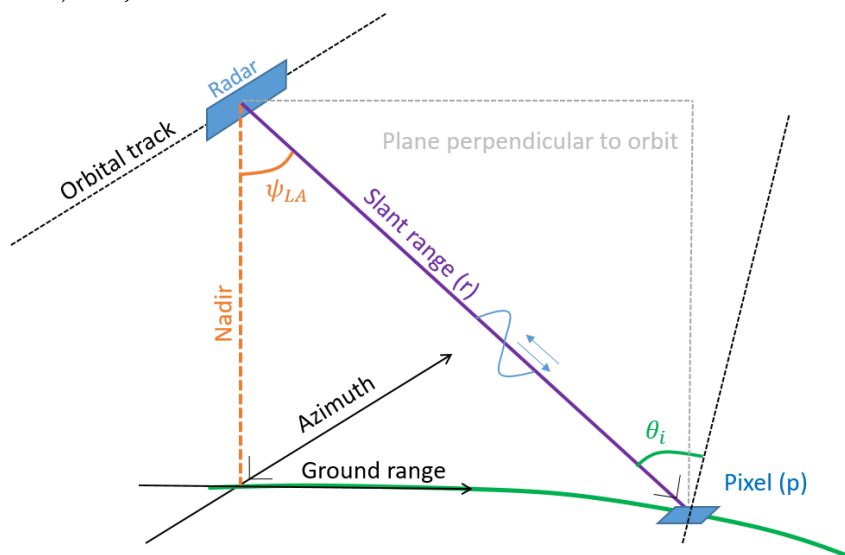


Fig. 3.1: Side looking geometry of an imaging radar with its antenna directed towards the right with the off nadir angle  $\psi_{LA}$  and the incidence angle  $\theta_{inc}$  which are unequal because of the curvature of the Earth. Nadir refers to the point on the Earth directly below the observation platform and slant range denotes the distance from the point of observation to the illuminated objects.

### 3.1. Imaging radar: SAR

Radar refers to both an instrument and a technique. A radar instrument emits electromagnetic waves and receives the reflection of these pulses. Through the two-way travel time it is possible to map these reflections on a stretch in its line-of-sight (LOS). From reflection intensities it is possible to deduce physical quantities such as surface roughness, size and orientation. Imaging radars belong to a specific class of radar systems where the antenna is mounted onto a moving platform perpendicular to its displacement direction so that it records data in two dimensions as illustrated in Fig. 3.1. The antenna has a side looking geometry making the radar system sensitive in the range direction. The high azimuth resolution is achieved by combining information obtained through continuously sending and receiving radar pulses. This results in an artificially large antenna which is where the terms synthetic and aperture from the acronym SAR are derived from (Hanssen, 2001).

The transmitted radio waves travel from the satellite to the Earth's surface and back again. Scatterers reflect the radiation from different distances with respect to the radar system. Current imaging radar use coherent imaging, which means they are capable of retrieving phase and amplitude information associated with small areas on the Earth's surface also referred to as 'resolution cell' or 'pixel'. The phase and amplitude information can be derived from the in-phase and quadrature phase measurements which are stored as real and imaginary numbers respectively into a complex data format. The phase information of this pixel is proportional to the two-way travel distance of all objects within this pixel according to

$$\phi_s = \frac{2\pi}{\lambda} 2r = \frac{4\pi}{\lambda} r \quad (3.1)$$

with the SAR image phase  $\phi_s$  having a linear dependence with the two-way travel distance  $2r$  over the wavelength  $\lambda$  (Ferretti et al., 2007). The phase variable can only be measured in the interval  $[-\pi, \pi)$  thus only the phase of the final incoming wave is measured and the unknown integer number of waves in the two-way travel distance remains unknown.

### 3.2. Radar interferometry: InSAR

InSAR can be used for deformation monitoring using SAR satellites. It is not the distance measurement resulting from time observations that provides the opportunity to measure deformation since this is only accurate to a scale of several meters. Also the phase measurement from a single satellite pass does not provide any useful information as the values are essentially uniform distributed. Only when a second SAR image is considered, the desired information can be extracted (Hanssen, 2001).

By using two SAR images of the same area, the pixels have been recorded at least twice from a slightly different 'look angle' as presented in Fig. 3.2. The phase difference between these two acquisitions can be calculated for each of these pixels by first aligning and resampling them to the same grid and consequent performing of complex image multiplication. The resulting image is known as the complex interferogram which is calculated according to

$$I = M \cdot S^* \quad (3.2)$$

in which the complex interferogram  $I$  is created by multiplication of the master image  $M$  with the slave image  $S$  with the  $\{.\}^*$  denoting the complex conjugate. The interferometric phase is now the difference in phase between the master and slave image for each pixel whereas the amplitude of the interferogram is the result of a multiplication of master and slave amplitudes (TU Delft, 2008; Hanssen, 2001).

The interferometric phase is composed of multiple phase contributors of which the most important ones are summarized as

$$\phi_I = \phi_{flat} + \phi_{topo} + \phi_{defo} + \phi_{APS} + \phi_{scat} + \phi_{noise} \quad (3.3)$$

with the interferometric phase<sup>1</sup>  $\phi_I$  equal to the summation of the flat Earth<sup>2</sup> reference phase  $\phi_{flat}$ , the topographic phase contribution  $\phi_{topo}$ , the surface deformation phase  $\phi_{defo}$ , the contribution by atmospheric delay  $\phi_{APS}$  also referred to as Atmospheric Phase Screen (APS), the phase caused by differences in scatterers within a pixel  $\phi_{scat}$ , and several noise terms combined into  $\phi_{noise}$  (Van Leijen, 2014; Maljaars, 2015). The reference phase incorporating both  $\phi_{flat}$  and  $\phi_{topo}$  is defined as

$$\phi_r \equiv -\frac{4\pi}{\lambda} (r_M - r_S) = -\frac{4\pi}{\lambda} B_{\parallel} \quad (3.4)$$

where  $r_M$  and  $r_S$  denote the slant range distance from the master and slave satellite respectively to the considered pixel on the reference surface whose difference results in the parallel baseline  $B_{\parallel}$  also visible in Fig. 3.2. A reference image can be made using the reference phase and amplitude

$$R = a \cdot e^{i\phi_r} \quad (3.5)$$

<sup>1</sup>The interferometric phase relates to the complex interferogram through  $\phi_I = \arctan_2(\text{Real}(I), \text{Imag}(I))$ .

<sup>2</sup>The author realizes that the Earth is not flat, however this term accounts for the reference surface without considering elevation hence 'flat' is used.

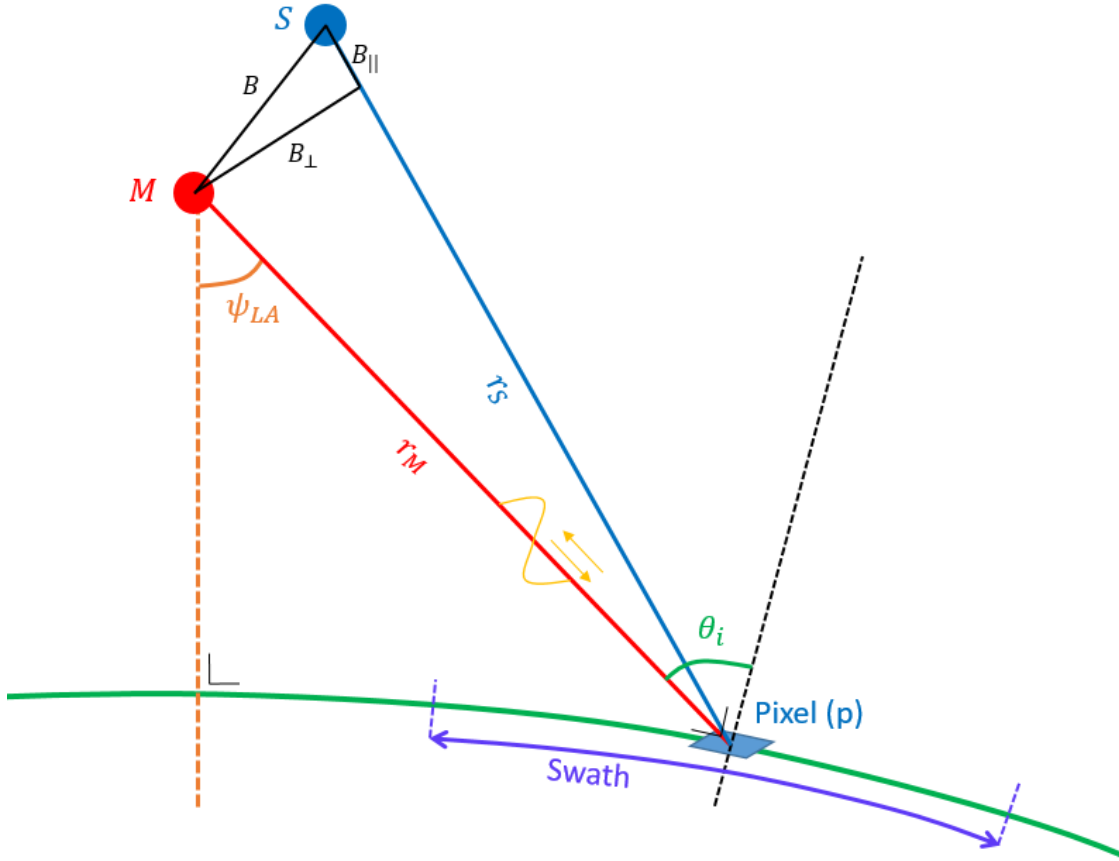


Fig. 3.2: Interferometric geometry in the plane perpendicular to the orbit vectors in which the master (M) and slave (S) acquisition for one pixel (p) are highlighted in red and blue respectively. The difference in  $r_M$  and  $r_S$  results in  $B_{\parallel}$ ,  $B$  is the absolute perpendicular distance between the orbit vectors, and  $B_{\perp}$  results from the squared relation of sides in a right angles triangle according to Pythagoras' Theorem. The ground range section which is recorded by each imaging radar is referred to as swath. Furthermore the 'Look angle',  $\psi_{LA}$ , and the incidence angle,  $\theta_{inc}$ , are both with respect to the global surface normal vectors. Note that the figure is not to scale since  $\vec{MP}$  and  $\vec{SP}$  should be in near-parallel configuration as  $B \ll r$ .

where the amplitude  $a \equiv 1$  by definition, and the reference phase  $\phi_r$  results from equation (3.4). Using complex multiplication once more, the reference phase can be subtracted from the interferogram without modifying the amplitude through

$$I_R = I \cdot R^* \quad (3.6)$$

resulting in the complex subtracted reference interferogram  $I_R$  whose phase does not contain contributions from  $\phi_{flat}$  and  $\phi_{topo}$  (TU Delft, 2008). The subtraction of the reference phase is, thus, necessary to reveal  $\phi_{defo}$  and is usually performed in two steps because  $\phi_{flat}$  and  $\phi_{topo}$  are conveniently modelled separately.

InSAR for deformation monitoring is best applied under coherent conditions in which the reflected signals of different acquisitions correlate strong. Non-coherent conditions arise mainly as a result of temporal or geometric decorrelation. Geometric decorrelation is the result of non-overlapping spectral bands caused by a large  $B_{\perp}$  separation in repeating orbits (Hanssen, 2001). Temporal decorrelation occurs when the scattering characteristics of the Earth's surface change over time within a resolution cell (Van Leijen, 2014), for instance by a change in land-use or in vegetated areas. Even when the conditions for coherence are met, the spatially and temporally varying APS introduces a signal that is hard to distinguish from deformation. In the ideal case where the deformation signal predominates the APS under highly coherent conditions, the deformation can directly be deduced from the subtracted reference interferogram. In the less ideal cases in which either, or all, of these factors are unfavourable, additional processing using advanced time-series analysis algorithms such as Persistent Scatterer InSAR (PSI) as described in the next section.

### 3.3. Persistent Scatterers

The previous section elaborated on the limitations in conventional InSAR consisting of decorrelation and variable atmospheric delay. Since the late 90's, some algorithms for time series analysis have been developed to (partially) overcome these two limitations by selecting pixels with the least decorrelation noise and estimating the non-deformation phase contributors. One of these algorithm categories is widely known as PSI and focusses on pixels that have a dominant scatterer present, which ensures that the least amount of temporal decorrelation occurs. The concept of dominant scatterers is briefly discussed below (Hooper et al., 2012). The time series set-up corresponding to this method uses a single master image combined with several slave images to form a single master stack.

As previously indicated, all objects within a resolution cell contribute to the scattering phase  $\phi_{scatt}$  of equation (3.3). Let's assume that the considered cells are coherent in time, then there are two extreme cases possible in scatterer characteristics: point scattering (or PS) in which one stable high amplitude scatterer is present that dominates all other scattering objects, and Distributed scatterers (DS) in which multiple equally strong and stable scatterers combined ensure phase-stability. These different scattering characters are best exemplified in Fig. 3.3 where two abstract representations of a scattering composition within a resolution cell are shown. Temporal decorrelation caused by relative motion of scatterers within a cell is greatly reduced when there is a significant stable scatterer present (Van Leijen, 2014).

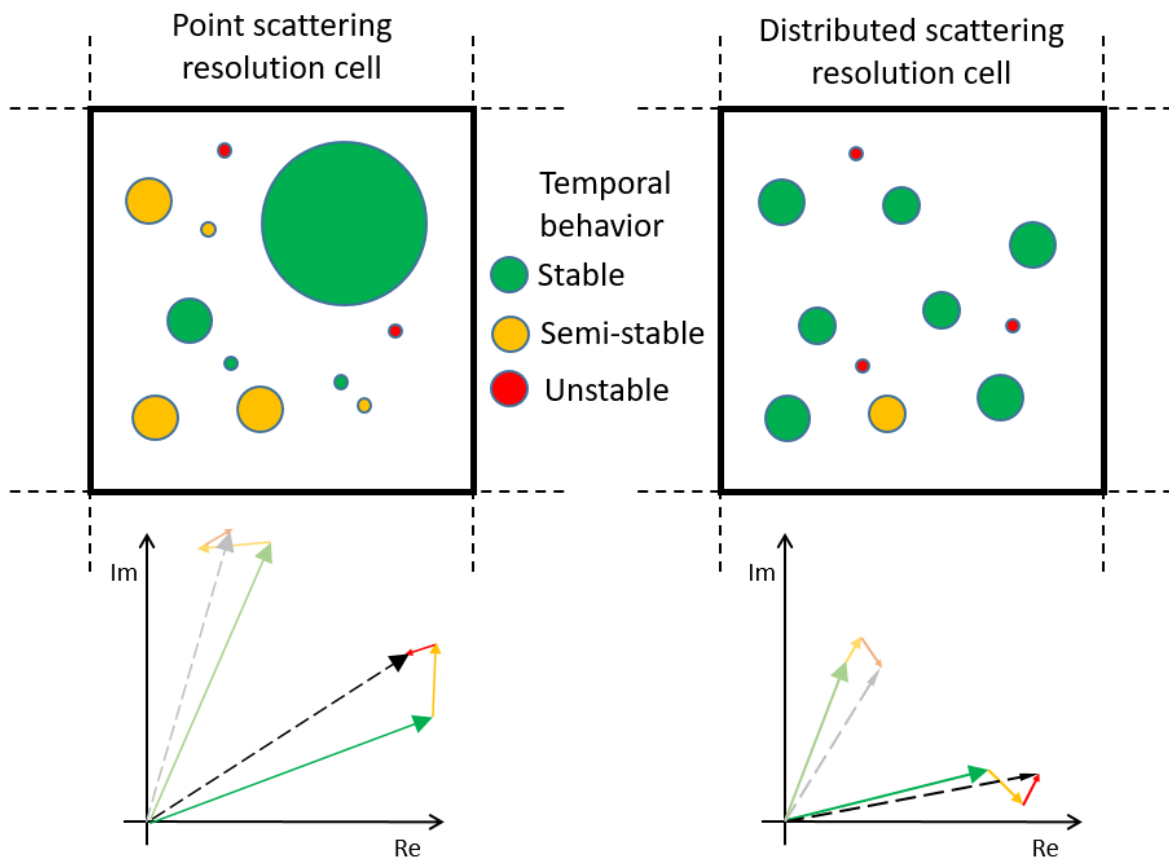


Fig. 3.3: Coherent scatterer examples with a PS resolution cell on the left and a DS resolution cell on the right. The size of each dot in the top corresponds with the amplitude of the reflected signal and the colour relates to the temporal stability of these scatterers. The corresponding phasors can be found at the bottom of the figure. The PS cell has one dominant scatterer present which determines the major part of both the amplitude and phase of the full resolution cell while the DS cell has multiple scatterers that are equally important in terms of amplitude in phase. In order to be coherent in time, the first needs the largest scatterer to be phase-stable while the latter needs stability in most of the scatterers. The amplitude dispersion is generally lowest in the PS and higher in the DS cell

Obviously not all cells are coherent in time, which is the reason for using the PSI technique in the first place. Therefore it is a matter of determining which cells can be used for a PSI time series analysis. Although it is ultimately the level of decorrelation noise (or deformation phase-stability) that determines if a pixel is suitable for PSI, the amplitude dispersion serves as a great initial estimate for filtering out noisy pixels and selecting the appropriate PS candidates (Ferretti et al., 2001).

After a first selection of candidates, there are essentially two approaches for determining which candidate PS pixels are in-fact well correlated. The first relies on modelling the deformation of nearby candidate pixel phase-differences in time by assuming a temporal model of evolution which significantly reduces the atmospheric and orbital effects. In the second approach, spatially correlated terms such as deformation, atmosphere, and orbit error are estimated for each PS candidate and subtracted from the time series leaving residuals representative for noise estimates. For both approaches the deformation phase is separated from the atmospheric phase and noise using correlation characteristics; deformation is assumed to be correlated in time; atmosphere is uncorrelated in time but correlated in space and noise is uncorrelated both in time and space (Hooper et al., 2012).

### 3.4. Unwrapping

Whether PSI is used or the phases from the interferograms are directly inferred, it is usually not possible to interpret these phases directly in terms of absolute range because relative phase is wrapped into the  $[-\pi, +\pi)$  interval. Nonetheless, it is possible to evaluate the relative range change for two points within an interferogram by integrating the number of  $2\pi$  fringes between them. This process of estimating the relative phase change outside the wrapped domain is called unwrapping. Without any additional information on the unwrapping output, the results will never be completely reliable as they are inferred using a fair amount of assumptions (Hanssen, 2001; Hooper et al., 2012).



# 4

## Materials and Methods

The data, tools and methods that were used in this research are discussed in this chapter. This chapter has been split into two sections, the first of which describes the materials in terms of used data and software and consecutively, the latter explains how these materials were combined to extract the desired results. Some of the considerations were adopted from a pre-study done for this thesis which is included in full in Appendix C.

### 4.1. Materials

This section describes the data and software that is used to conduct this research. The data selection for InSAR is described in great detail for easier reproducibility, whereas the other datasets and used software are briefly discussed.

#### 4.1.1. SAR data selection

The feasibility of performing deformation analysis using InSAR is largely determined by the available data. Data series of five satellites have been reviewed; European remote sensing satellite 1 (ERS-1), Environmental Satellite (Envisat), Radar satellite 2 (Rsat-2), COSMO-SkyMed (csk) and Sentinel-1 (S1). A summary of the available datasets is presented in Fig. 4.1. Only tracks covering the entire spatial domain of Yangon having more than ten acquisitions were selected. The series were split into ascending and descending orbits since they require separate processing. Note that there is a gap in acquisitions between 1999 and 2003.

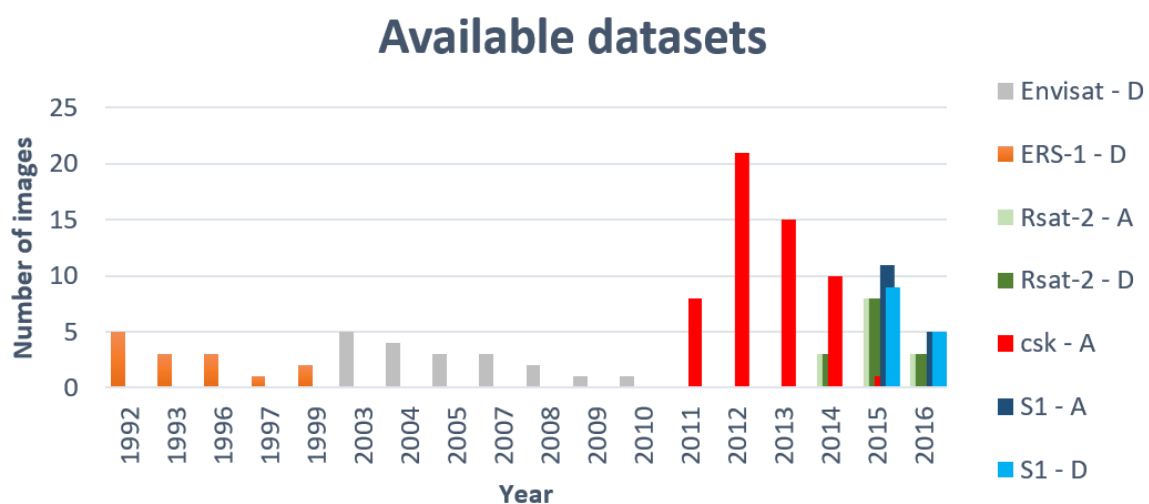


Fig. 4.1: Number of available images per year for the Envisat, Radarsat-2, COSMO-SkyMed, and Sentinel-1 satellites split into ascending and descending orbits. Source: SkyGeo

The S1 satellites were favoured because of their recent acquisitions, fast updating data stack and both ascending and descending orbits recordings. In addition, it is free for anyone to use. Although not presented in this graph, Radar satellite 2 only has acquisitions outside the monsoon period, but does have both ascending and descending orbits recorded. Finally, the csk has a dense amount of images between 2011 and 2015 but getting these images proved to be tricky<sup>1</sup> and could have possibly been expensive. ERS-1 and Envisat are too early in time, before 2010, to be of interest for the current study and will thus be disregarded.

The data was collected as level-1 Single Look Complex (SLC) data with a  $5 \times 20$  m ground geometry as provided by Copernicus' scientific data hub. All data is collected in the IW with a single 'VV' polarisation for the ascending orbits and a dual 'VV + VH' polarisation for the descending orbits. The dates range from *May 11<sup>th</sup>, 2015* until *Oct 20<sup>th</sup>, 2016* and a total of 21 ascending and 19 descending images were used. Although the S1A and S1B satellites were both operational during the course of this research, only images from S1A were used as no data was recorded over the area of interest by the S1B satellite.

#### 4.1.2. Orbital information

The orbital information for the S1 satellite was used as an input for InSAR processing. In the annotation of the SAR images, there is also orbital information added which has found to be inaccurate by several users, most likely the result of not having reached the final reference orbit (Schubert et al., 2014). Therefore more precise orbital data is desired which is handled by Copernicus Precise Orbit Determination (CPOD) service as a part of the Copernicus ground segment. Orbital information is released in near real time with a latency of 180 min at an accuracy of 10 cm and a latency of 20 days at an accuracy of 5 cm (Fernandez et al., 2016). In general, the most accurate and available of these two was used for the processing of each image.

#### 4.1.3. Digital Elevation Model

A Digital Elevation Model (DEM) is necessary for co-registration and phase subtraction when InSAR is used. The creation of a DEM using S1 would have been difficult as no tandem missions exist making the temporal baseline too high while the perpendicular baseline is too small. Therefore a DEM was extracted from Shuttle Radar Topography Mission 3'' (SRTM3) with a ground resolution of 90 m. For the use of this data for SAR processing, the Unix and Generic Mapping Tools (GMT) based utility 'construct\_dem.sh' (part of the Doris package) was used to create a merged and void-less DEM suitable for further processing using Delft object-oriented radar interferometric software (Doris) (see 4.1.4). Notable benefits of using this utility are that the format is instantly correct, and that file input information is automatically generated.

#### 4.1.4. Doris

Selected SAR images were processed using the Doris software package for InSAR processing. Doris is an object-oriented modular processor which is freely available for the scientific community. The InSAR processor initially developed by Kampes et al. (2003), handles the processing from level-1 SLC data through the computation of complex interferograms. The program is UNIX based and mainly coded in C++ which can be compiled using a freely available compiler. The publicly available version did not yet incorporate the possibility to process S1 data, while the beta version of Doris v5 was already equipped with this feature. Doris version 5 was still being developed over the course of this master thesis. The new shell of Doris is coded in Python while the base of the program remains the same. A more detailed description of the steps necessary for S1 processing will be given in section 4.2.1.

#### 4.1.5. StaMPS

The complex interferograms resulting from the processing using Doris was used as input for processing using Stanford Method for Persistent Scatterers (StaMPS) which is a tool for PSI processing. This software package was originally developed at Leeds by Hooper et al. (2012), with subsequent contributions from Iceland and Delft. The software package consists of C++ and Matlab scripts which can identify coherent and phase-stable pixels in a single-master stack of interferograms and ultimately extract the deformation signal from it. Though the program also has a small baseline method implemented, it was not used since it was not yet developed for S1. This software package also implements external programs called Statistical-Cost, Network-

---

<sup>1</sup>The author has tried getting these images free of charge for academic purposes, unfortunately with nothing to show for it.

Flow Algorithm for Phase Unwrapping (SNAPHU) and Triangle which perform the phase unwrapping step on Delaunay triangulation respectively. Although SNAPHU performs unwrapping in two space dimensions, StaMPS has a slight different approach incorporating also the temporal dimension. In section 4.2.2 the processing steps of StaMPS are explained in greater detail.

The choice for using StaMPS was based on two important considerations. Firstly, the method works without assumption of variation in displacement rate which might be present in the case of Yangon where strong seasonality is found in its climate and possibly in the sources of subsidence. Secondly, the amount of data required to extract results can be as little as fourteen images, though more images would lead to significantly better results (Hooper et al., 2007).

#### 4.1.6. SNAPHU

SNAPHU is a two-dimensional phase unwrapper able to retrieve the ambiguity from reference phase subtracted interferograms (Chen & Zebker, 2000). The program developed by C.W. Chen is written in C and functions on UNIX platforms. One important reason (other than being implemented into StaMPS) for the usage of this software is the author's claim that it performs comparable or better than other available algorithms. How this program is implemented, is explained in section 4.2.2 together with the concept of unwrapping.

#### 4.1.7. Interface

Since StaMPS relies on available software for InSAR processing, it was not yet suitable for S1 processing as they (Doris and others) were not yet available for the scientific community. To couple the wrapped output of Doris to the PSI unwrapper, a series of UNIX and Python based scripts were developed specifically for the purpose of this research. These scripts combined, form the interface (hence the name) between these two software packages through setting up the correct file and folder structure, cropping all necessary files to the area of interest, calculating the correct baseline parameters, and preparing the patched PS computations. The development of the Interface was directed towards PSI only because the addition of the small baseline approach would be too time consuming.

## 4.2. Methods

Previously mentioned data and software were combined measure subsidence and assess their connection to groundwater extraction. The structure of data and software for obtaining the subsidence results is shown in Fig. 4.2. This section will elaborate on the InSAR processing, StaMPS post-processing and spatial water resources analysis.

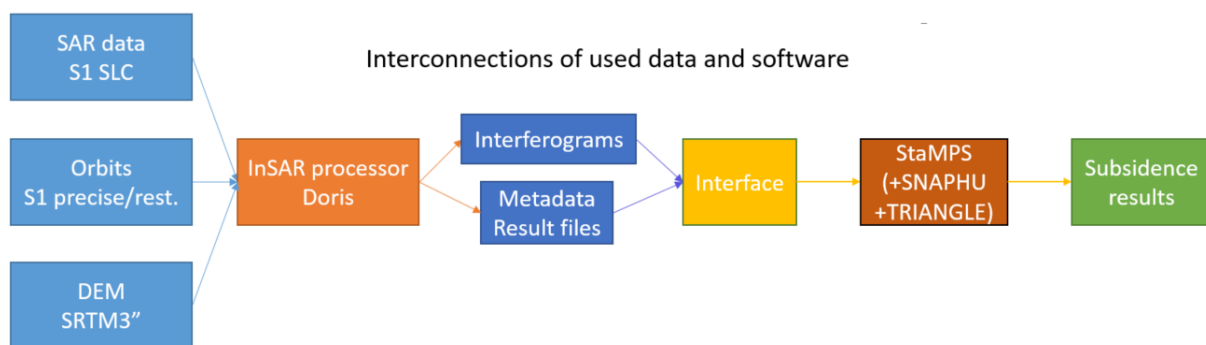


Fig. 4.2: The diagram shows how the data and software are connected to produce the subsidence results.

#### 4.2.1. InSAR processing using Doris

For the processing of SLC data to interferograms, the beta version of Doris v5 was used for S1 processing. Stated here are the important processing choices that were made and processing structures that were used to combine the SAR data, orbits and DEM into interferograms. A pre-study with the same data provided more insight into the requirements for the current study regarding the choice for a master image (van der Horst, 2016).

To start with, the perpendicular and temporal baselines had to be optimized. Shown in Fig. 4.3(a) and Fig. 4.3(b) are the perpendicular baselines for ascending and descending orbits respectively. Perpendicular baselines of the S1 are generally small as the satellite is steered quite accurately into the same orbital track. Each image pair that can be made has a baseline far below the critical baseline. The master images were chosen based on van der Horst (2016) stating the dry season is most suitable for coherent interferograms. Optimizing temporal baseline over perpendicular baseline with a master image in the dry season were the decisive factors for the chosen master images.

Considering the height ambiguity, the sensitivity for errors made by DEM phase subtraction of the final interferogram is less for small values of  $B_{\perp}$ . This holds because the topographic phase,  $\phi_{topo}$ , scales proportional to the perpendicular baseline according to the phase-topography relation

$$\Delta\phi_{topo} = -\frac{4\pi}{\lambda} \left( \frac{B_{\perp}}{r \sin\psi} \Delta H_p \right) \quad (4.1)$$

with the topographic height  $H_p$ . For typical S1 values with  $r = 8 \times 10^5$ ,  $\psi = 45^\circ$  and a large  $B_{perp}$  of 150 m an error in the DEM of 5 m would lead to a phase error of 0.012 rad.

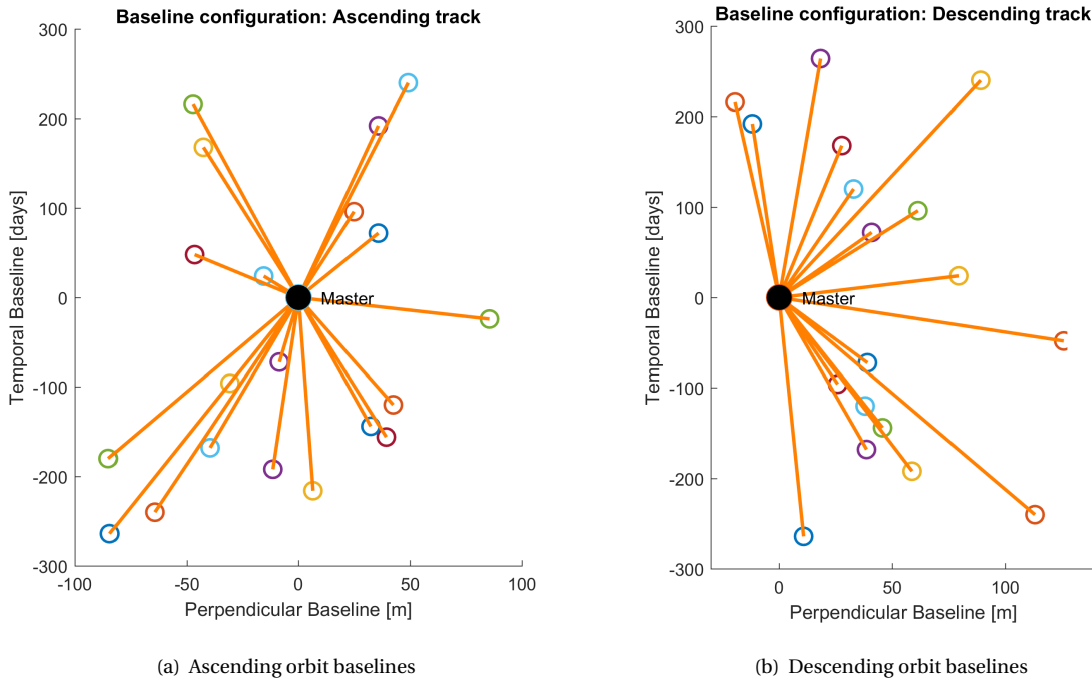


Fig. 4.3: Perpendicular baselines of all used ascending and descending orbit images. The circles represent SAR images and the lines indicate the interferograms that are formed.

Next, the processing structure for S1 data is somewhat different from other missions as its default acquisition mode uses TOPS instead of the frequently used Stripmap mode. The benefit of this mode is a large swath width of 250 km at the cost of azimuth resolution. Further benefits include a reduction of the revisit time to twelve days per satellite instrument<sup>2</sup> and large illuminated areas allowing for large area computations.

The TOPS acquisition mode captures in three range sub-swaths by steering the antenna in range and azimuth direction as illustrated in Fig. 4.5. Hereby the coverage in range direction is increased at the cost of azimuth resolution as the steering in azimuth direction, necessary to avoid scalloping, shrinks the footprint (De Zan & Guarnieri, 2006; Sakar, 2014). The sub-swaths are split into multiple bursts with marginal overlap and each burst is processed as a separate SLC image. The steps required for the processing of InSAR datasets using

<sup>2</sup>Though the S1 satellite passes by every twelve days for each track, it does not necessarily record at all times because of a maximum transfer capacity to the ground segment.

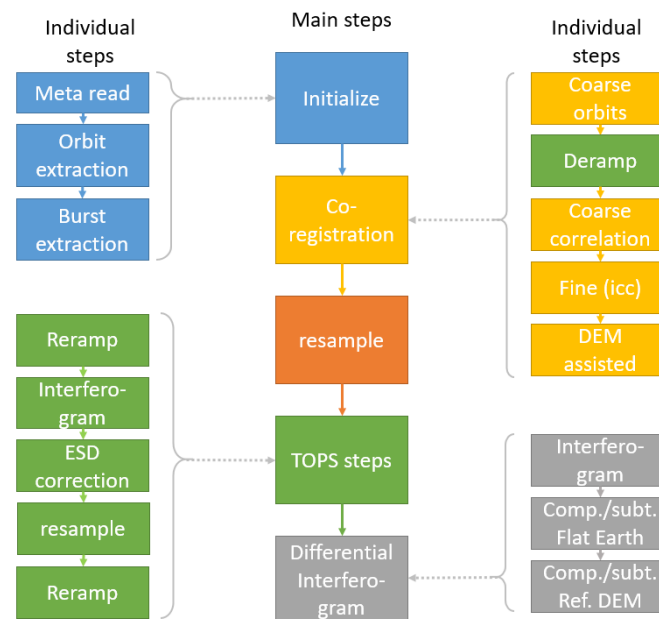


Fig. 4.4: Processing scheme for S1 Terrain Observation by Progressive Scans (TOPS) mode. The main steps are indicated in the centre column with their individual processing steps at the sides columns. The additional steps for S1 are highlighted in green. This scheme reflect the steps that were used in this research, but they might be subjected to change for future processing.

Doris is shown in Fig. 4.4, where additional steps required for TOPS are highlighted in green. More detailed information on Sentinel processing is given below as it differs from the regular stripmap processing steps.

**Initializing:** The SLC metadata are read. complete bursts covering the area of interest are extracted while the ones outside the domain of interest are rejected completely. The corresponding orbit files are read and the part covering the acquisition is extracted from the precise or restituted orbit file.

**Co-registration:** At the coarse correlation step, the master and slave image offsets are calculated on magnitude images in the space domain rather than the spectral domain since it performs much better in low-coherent areas. An extra step is introduced in the processing of TOPS data since a quadratic phase ramp is introduced because of the steering in azimuth direction of the radar beam during acquisition. Grandin (2015) has provided a method to remove this quadratic phase called 'deramping'.

**Resampling:** One additional resampling step is introduced for the creation of the first interferogram necessary for the TOPS processing steps. The first resampling has to be accurate to sub-pixel level for which the offsets are derived in the fine co-registration step.

**TOPS steps:** The precise alignment of the master and slave images has to be accurate to within  $1/1000^{th}$  of a pixel. This precise co-registration is necessary because the difference in squint angle to the ground targets during acquisition introduce a large Doppler centroid variation. A mis-registration leads to a phase jump at the burst boundaries. The accuracy is obtained by exploiting the spectral difference at the overlapping edges of the bursts; the interferometric phase difference between overlapping bust edges can be related to the mis-registration in azimuth direction (Sakar, 2014). Once the exact co-registration parameters are determined, the original deramped product is resampled and reramped again to the desired alignment accuracy.

**Differential Interferogram:** These steps do not differ much from regular differential interferogram formation. For each burst the interferometric phase is calculated and a continuous interferogram is created by mosaicking the bursts together. The reference and topographic phases are calculated and subtracted in two steps resulting in the differential interferogram.

After processing of all images within a stack into interferograms, quality checks were performed with subsequent reprocessing of faulty interferograms. For the purpose of PSI processing, no multi-looking has been performed throughout the processing, to retain the maximum resolution possible but more importantly not to average out existing PS pixels. The resulting interferogram stacks were used as input for the 'Interface' thereby preparing the PSI processing.

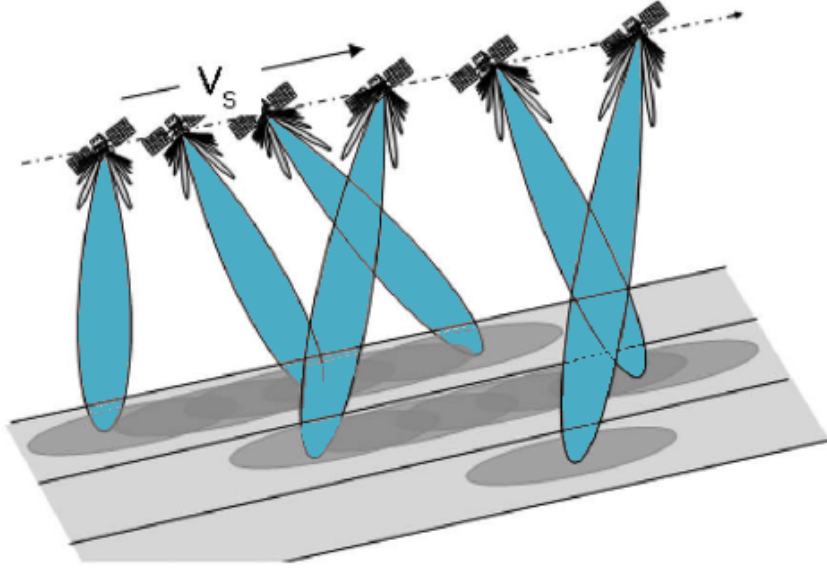


Fig. 4.5: TOPS acquisition, the three sub-swath scanning scheme by steering in both azimuth and range direction (De Zan & Guarnieri, 2006).

#### 4.2.2. PSI processing with StaMPS

The PSI processing was done using the StaMPS software which was able to process the Doris output through the Interface scripts which prepares processing in patches. First, the final step of the Interface consists of setting a threshold for the amplitude dispersion index defined by Ferretti et al. (2001) as

$$D_A \equiv \frac{\sigma_A}{\mu_A} \quad (4.2)$$

where  $\mu_A$  denotes the mean value and  $\sigma_A$  stands for the standard deviation of the interferometric pixel amplitude time series Hooper et al. (2007). The dispersion threshold value of 0.42 was chosen for a first selection of possible PS candidates. Subsequent processing steps that are typically applied can be summarized as follows:

- **Step 1** - Initial load of data
- **Step 2** - Estimate phase noise
- **Step 3** - Select PS pixels
- **Step 4** - Weeding of adjacent pixels
- **Step 5** - Correct Spatially-Uncorrelated Look Angle (SULA) and merging
- **Step 6** - Unwrapping
- **Step 7** - Calculation of Spatially-Correlated Look Angle (SCLA)
- **Step 8** - Filtering spatially correlated noise

The first step is too trivial to require further explanation, but the second one is rather important. In this iterative step, the wrapped interferometric phase contributors  $\phi_{defo}$ ,  $\phi_{APS}$ , and the residual phase due to 'look angle' error  $\Delta\phi_\psi$  were estimated and removed from the subtracted reference interferogram leaving the  $\phi_{noise}$  term. Pixels with a high  $|\phi_{noise}|$  were rejected from the candidate list in the third step. The successive fourth step performed weeding of adjacent cells which is essentially searching for pixels that are dominated by the scatterer that is in another physical location next to it. For groups of stable neighbouring pixels, only the pixel with the highest spatial coherence value is chosen as PS pixel. In step five, the wrapped phases are corrected for Spatially-Uncorrelated Look Angle (SULA), that is the part of the phase sensitive for  $B_\perp$  with no consideration regarding spatial correlation. Following after this is possibly the most difficult step of all, the phase unwrapping.

The only accurate unwrapping can be performed when neighbouring PS pixels have a difference less than  $\pi$  rad. In reality this is true for spatially correlated pixels that are sufficiently close to each other. Using the time-series of PS pixels, the unwrapping step was improved by unwrapping in three dimensions (two in space and

one in time) rather than two dimensions (solely space) which is best explained in Hooper & Zebker (2007). For this unwrapping step to perform satisfactory, some assumptions need to be made regarding the behaviour of the signal of interest. Especially the unwrapping pre-filter grid size and smoothing time are best set to match the expected subsidence signal with the grid size chosen such that expected deformation within this distance is less than  $\pi$  rad and the smoothing time small enough to account for possible seasonality effects. The grid size and time window were set to 200 m and 180 d respectively.

Finally step seven is performed in which the SCLA error is estimated to remove any effect of different  $B_{\perp}$  values on the phase values. The estimated SCLA is almost exclusively due to errors in the DEM consisting of a difference between the actual surface and elevation, errors in the DEM itself, and resampling errors of the DEM onto radar coordinates. The eighth and final step is not performed since it often results in poorly estimation of the slave atmospheric signal and can negatively influence the results in some cases.

### 4.2.3. Decomposition

The output from the PSI analysis is retained in sensor geometry with the surface deformation velocity defined onto the LOS vector. Using both ascending and descending stacks, PS pixels that have been observed by both can be decomposed into vertical and horizontal components. Note that a full decomposition into three dimensions is not possible since there is a maximum of two measurements for each pixel.

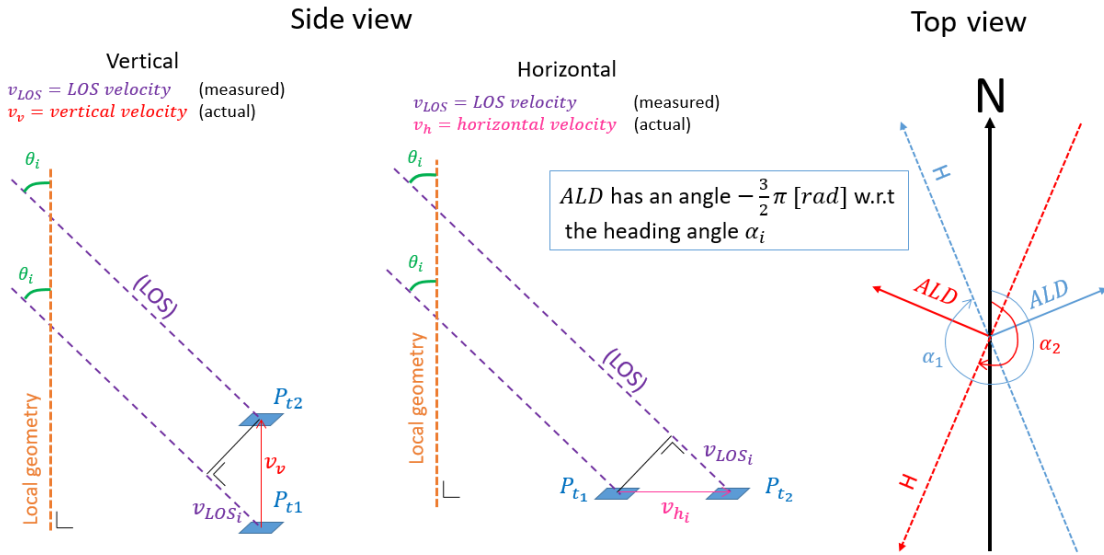


Fig. 4.6: Decomposition geometry with the side view showing how the vertical velocity,  $v_v$ , and horizontal velocity,  $v_{h_i}$ , are projected onto the LOS velocity through a surface displacement from  $p_{t1}$  to  $p_{t2}$  under an incidence angle,  $\theta_i$ . The Top view shows the heading direction,  $H$ , with the corresponding heading angle,  $\alpha_i$ , and the azimuth look direction (ALD) directed at  $-3/2\pi$  with respect to the heading direction for a right-looking sensor.

The satellite geometry with the line-of-sight (LOS) velocity,  $v_{LOS}$ , projected onto the horizontal and vertical deformation vectors is shown in Fig. 4.6. It is possible to rewrite the  $v_{LOS}$  in terms of vertical, north, and east velocity according to the relation described by Hanssen (2001) as

$$\begin{aligned} v_{LOS} &= [\cos(\theta_i), -\sin(\theta_i) \cdot \cos(\angle ALD_i), -\sin(\theta_i) \cdot \sin(\angle ALD_i)] \cdot [v_v, v_n, v_e]^T \\ v_{LOS} &= [\cos(\theta_i), -\sin(\theta_i) \cdot \sin(\alpha_i), -\sin(\theta_i) \cdot \cos(\alpha_i)] \cdot [v_v, v_n, v_e]^T \end{aligned} \quad (4.3)$$

with the  $ALD_i$  directed at  $-\frac{3}{2}\pi$  rad w.r.t. the heading direction with the angle,  $\alpha_i$ , and the index,  $i$ , denoting the track index for ascending or descending. This results in an ill-posed problem with only two  $v_{LOS}$  for three unknown variables, so additional information is needed. If an assumption can be made regarding the direction of the horizontal movement,  $\gamma$ , the north-east domain can be converted to a local  $x, y$ -system through a rotational matrix

$$\begin{bmatrix} v_e \\ v_n \end{bmatrix} = \begin{bmatrix} \sin(\gamma) & -\cos(\gamma) \\ \cos(\gamma) & \sin(\gamma) \end{bmatrix} \begin{bmatrix} v_x \\ v_y \end{bmatrix} \quad (4.4)$$

in which the surface velocity perpendicular to the assumed direction,  $v_y$  is set to zero

$$\begin{bmatrix} v_e \\ v_n \end{bmatrix} = \begin{bmatrix} \sin(\gamma) \\ \cos(\gamma) \end{bmatrix} v_x \quad (4.5)$$

which can be substituted into (4.3) resulting in

$$\begin{bmatrix} v_{LOS_a} \\ v_{LOS_d} \end{bmatrix} = \begin{bmatrix} \cos(\theta_a), -\sin(\theta_a) \cdot \sin(\alpha_a - \gamma) \\ \cos(\theta_d), -\sin(\theta_d) \cdot \sin(\alpha_d - \gamma) \end{bmatrix} \cdot \begin{bmatrix} v_v \\ v_x \end{bmatrix} \quad (4.6)$$

which can be solved for two measurements (Van Leijen, 2014).

Before the decomposition was at all possible, the measurements were aligned and sampled onto the same grid. The alignment was necessary since the master of the ascending and descending stacks are each defined on their own grid and are therefore not resampled onto the same extent. Assuming the stacks do not need to be rotated with respect to each other, only the longitude and latitude offsets needed to be determined. By optimizing the number of co-registered PS points for different offset values within a certain longitude and latitude tolerance, the correct offset values were found. The sampling of velocity values was done through creating a linear spaced grid in longitude and latitude with a spacing larger than the SLC pixel geometry, and sampling all data within each grid cell to a mean value. At the grid locations where both the ascending and descending stacks were defined, the decomposed velocities were calculated.

#### 4.2.4. Groundwater extraction analysis

After completion of the processing of radar data, an assessment was made regarding the extraction of groundwater. The focus was directed at the spatial distribution and used quantities of the different drinking water sources. To support earlier found literature values for daily consumption, which deviated significantly from each other, a survey was held for validation which is further explained in section 4.2.5. Subsequent analysis relies on spatial estimation of drinking water usage through groundwater extraction.

The inhabitants who do not receive any water from the YCDC were assumed to have a private water system from which they receive their water. The results from the 'Household survey' (JICA, 2014a) help to determine the percentage of inhabitants with private water supply who extract their water from the subsoil. There is some overlap between inhabitants receiving water from YCDC and inhabitants having a private source of water. An estimate of the extracted amount groundwater through private was made using the following relation

$$Q_{priv} = P \cdot \left(1 - \frac{C_{2014}}{100\%}\right) \cdot D \cdot f_{Priv} \cdot \frac{1}{1000} \quad (4.7)$$

with the extracted discharge  $Q_{priv}$  in  $m^3/d$ , the population  $P$ , the coverage ratios  $C_{2014}$ , the average water demand  $D$  in  $L/p/d$  resulting from the water demand survey as explained in the next section, and the private groundwater extraction factor which accounts for sources other than groundwater. The township population was derived from (JICA, 2014a), the coverage ratios can be estimated using (YCDC, 2015) and the  $f_{Priv}$  has been approximated using the results from the 'Water source by township' study in JICA (2014a) where water sources are expressed in percentages of inhabitants according to a large household survey. From this, inhabitants who do not receive piped water could be divided into inhabitants relying on groundwater extraction and inhabitants having other means of getting their water.

#### 4.2.5. Water demand survey

For supporting and validating various data sources and extending the knowledge on the usage of domestic water in Yangon, a survey was held. The main focus of this survey was to validate the amount of water used by inhabitants of Yangon. The secondary objective was to assess how these inhabitants received their water. The most important information about this survey is shown in this section. For a full description of the survey set-up consult Appendix F.

The survey was performed using a questionnaire that could be filled in digitally. Users were approached through fellow students from Yangon and through Facebook. The questionnaire was composed of mainly closed questions to prevent interpretation biases. Moreover, it could also be completed quickly using radio

buttons or drop-down menus and without supervision of an interviewer. This was easily implemented since mainly facts and figures were asked which do not require an open question style. Difficult questions were split into manageable bits with the aid of images to avoid the misinterpretation of questions. Most of the questions did offer space to fill in an answer that was not pre-compiled because a variety of answers was expected.

The questionnaire was available on Google forms and AppSheet, making it available on nearly all digital devices. The AppSheet application had the advantage of enabling the user to complete the questionnaire offline while Google forms had an easier user interface. A fragment of each of these interfaces is shown in Fig. 4.7.

The survey consisted of three parts: general information, type of delivery, and water demand. First, the general information part only regarded gender, age, approximate location and occupation. Second, The type of delivery part was based on a previous held questionnaire of which no results were found (ILHCA, 2006). This section was directed at the sources of water, the daily and seasonal availability, and the quality of delivered water. Third, the Water demand part, based on USGS (2016); de Moel et al. (2004), was meant to assess the amount of water that was used on average. Simple questions such as: 'How long do you shower?', and 'How often do you wash your hands?' were combined with an assessment of the flow rate.

The figure displays two side-by-side screenshots of a survey interface. The left screenshot is from a mobile application titled 'Domestic water survey: Yangon'. It features a large blue water drop icon and a question: 'Which colour corresponds best to your water? (look at the picture above)'. Below the question are five numbered options (1-5) representing water clarity from clear to murky. Another question asks 'Does the water taste saline (salty)?' with five numbered options from 'not at all' to 'very much'. The right screenshot is from a Google Forms survey titled '3 - Water demand (2/7)'. It includes a question 'Do you have a bath at home?' with a dropdown menu, 'How many times per week do you shower?' with a dropdown menu, and a question 'Which picture matches your shower best in terms of flow?' with radio button options for 'Picture 1', 'In between 1 and 2', 'Picture 2', 'In between 2 and 3', 'Picture 3', and 'Other:'. Below these options are three photographs of showerheads labeled 1, 2, and 3, showing different water flow patterns. A final question asks 'How long does an average shower take?' with a dropdown menu.

Fig. 4.7: Two fragments from the survey that was held. On the left, a section of the mobile app showing a fragment of water quality questions for determining the type of delivery. On the right, a section of the Google forms survey on water demand. Both the App and the Google forms consisted of exactly the same content, with a slight difference in layout.



# 5

## Results

In this chapter the main results are shown which are relevant to the research questions. In all of the maps the axis labels have been left out intentionally as they are all the same with longitude in degrees east and latitude in degrees north on the x and y axis respectively. For interferometry results regarding wrapped and unwrapped phases, the reader is referred to Appendix D.

### 5.1. Line-of-sight velocity

The mean LOS velocity after the choice of the reference PS location is shown in Fig. 5.1. Blue areas indicate motion towards the satellite whereas red areas reveal motion away from the satellite. Note that the reference velocity in both cases has a colour between blue and cyan. In the case both ascending and descending LOS velocity point out negative red values, this can be considered as subsidence. The velocity points in the townships of Dagon Myothit (indicated with '1' in the figure) show very significant signs of vertical surface displacement directed downwards. Less severe, but still significant displacements are found in the Dawbon and Thaketa townships (indicated with '2' in the figure). The actual vertical velocity rates will be disclosed under decomposition in the next section.

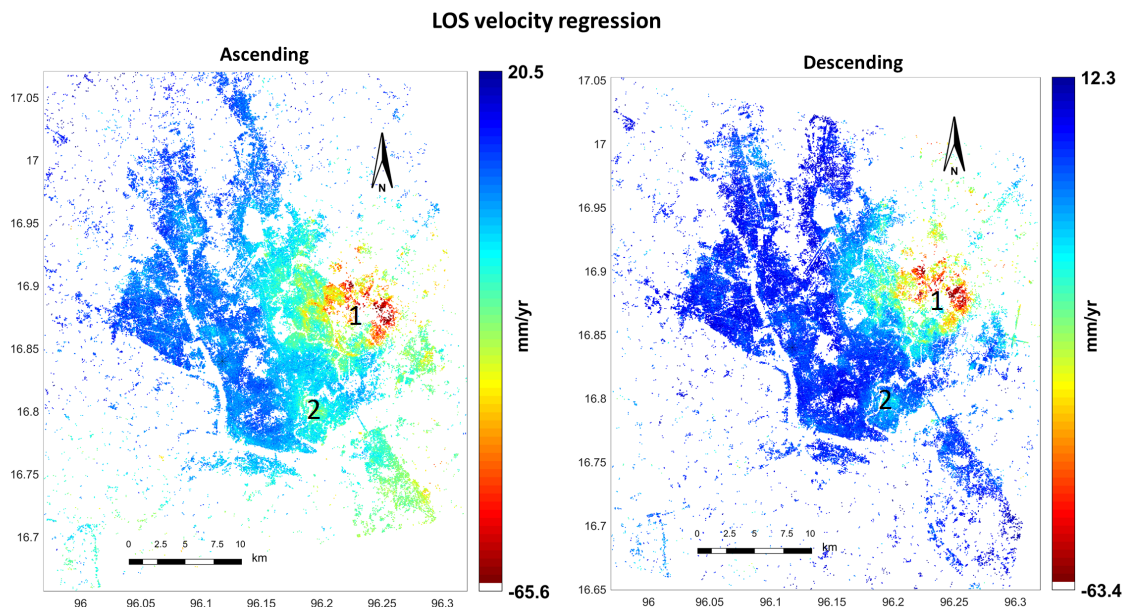


Fig. 5.1: The mean LOS velocity regression with subtracted DEM error for both ascending and descending data stacks for the period May 2015 to October 2016. The red and blue values indicate movement away from and towards the satellite respectively. The reference PS time series has been set as an average of the time series within a 250 m radius of  $96.1174^{\circ}\text{E}$ ,  $16.8398^{\circ}\text{N}$ . The most significant subsiding areas, Dagon Myothit and Dawbon, are denoted with numbers '1' and '2' respectively also used in further results.

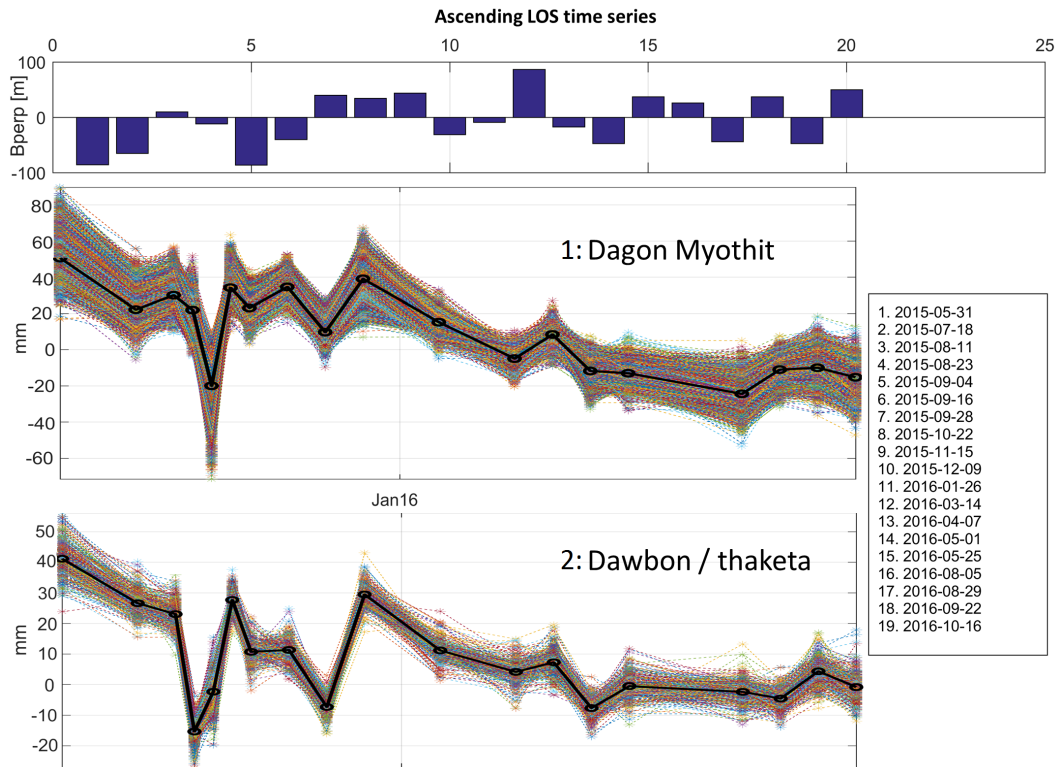


Fig. 5.2: Time series envelopes for the ascending track with displacement of scatterers in the LOS direction is plot against time. The coloured dashed lines show the individual point time-series, and the black solid line shows the mean of all considered scatterers. Also shown is the  $B_{\perp}$  plot (top) and the dates of acquisitions (right). The locations '1' and '2' correspond to the numbers in Fig. 5.1.

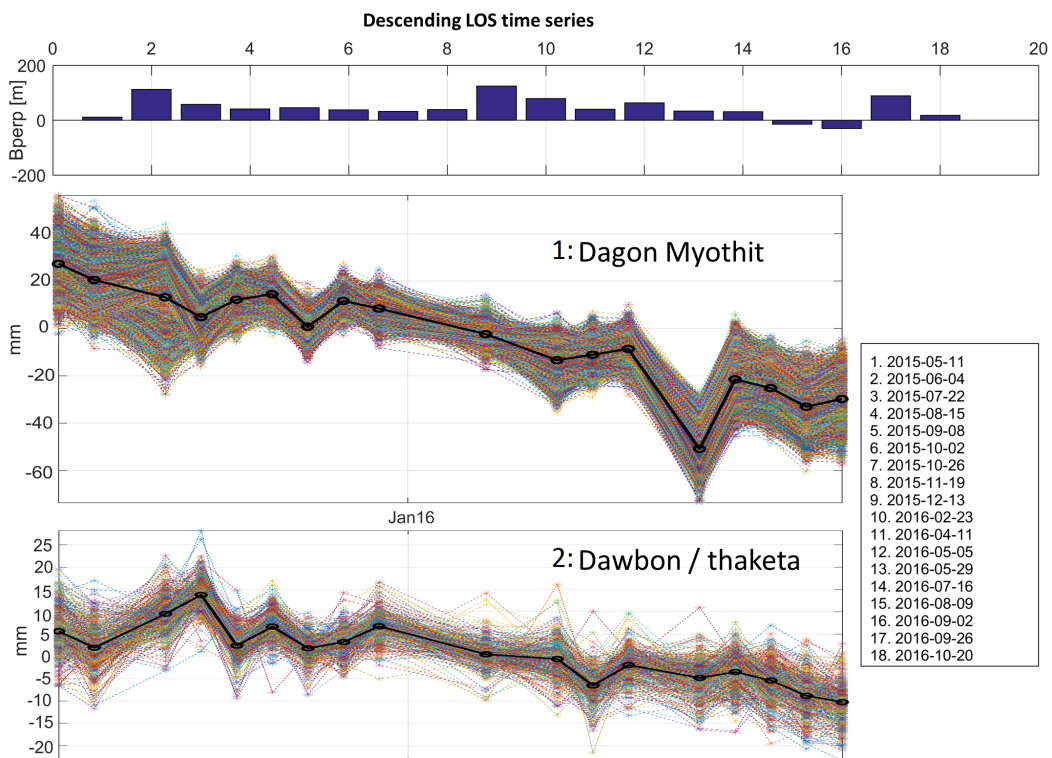


Fig. 5.3: Time series envelopes for the descending track with displacement of scatterers in the LOS direction is plot against time. The coloured dashed lines show the individual point time-series, and the black solid line shows the mean of all considered scatterers. Also shown is the  $B_{\perp}$  plot (top) and the dates of acquisitions (right). The locations '1' and '2' correspond to the numbers in Fig. 5.1.

The time series for the most significant displacement sites observed in Fig. 5.1 were extracted for the sites indicated with '1' and '2' and are plotted for ascending and descending tracks. The ascending time-series are shown in Fig. 5.2 and the descending time-series are shown in Fig. 5.3. The point selection radius for site '1' was set to 2500 m while the radius for site '2' was set to 500 m. The distances are measured on an interval scale which is why the difference in values should be considered rather than the absolute values. All of these individual time series show a significant directed down with several peaks that can be explained by atmospheric effects. Because of the relatively short acquisition period, it is hard to determine if any seasonal effects are present.

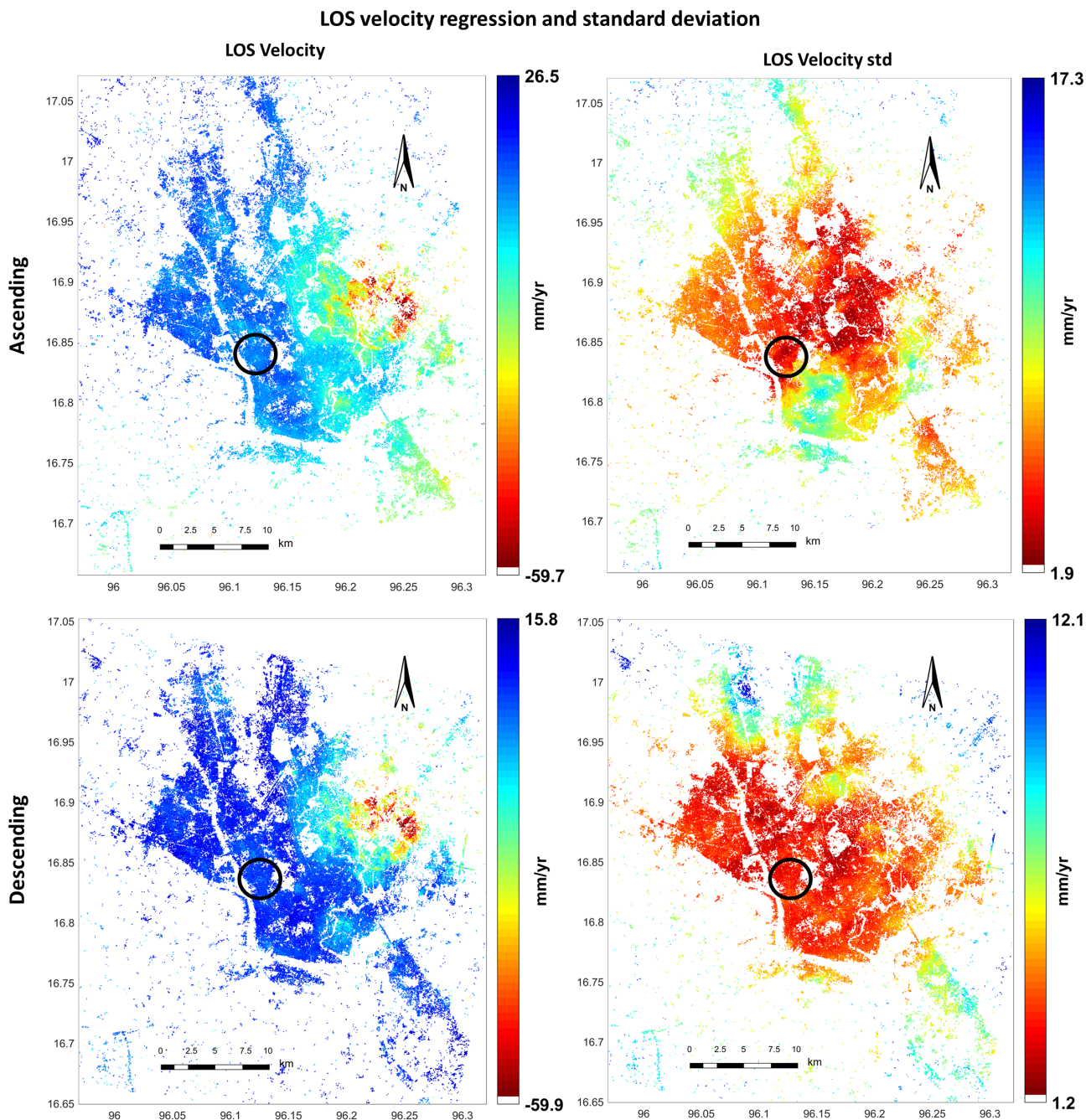


Fig. 5.4: On the left LOS velocity regression with subtracted DEM error where red and blue values indicate movement away from and towards the satellite respectively. On the right the standard deviation where red implies high quality scatterers with respect to the reference PS which consists of the time series averaged over the whole city. The black circle is placed over the area that was deemed suitable for the reference PS. In both standard deviation figures, the non-red areas reveal higher atmospheric influence or pixels behaving very different from the average city time series.

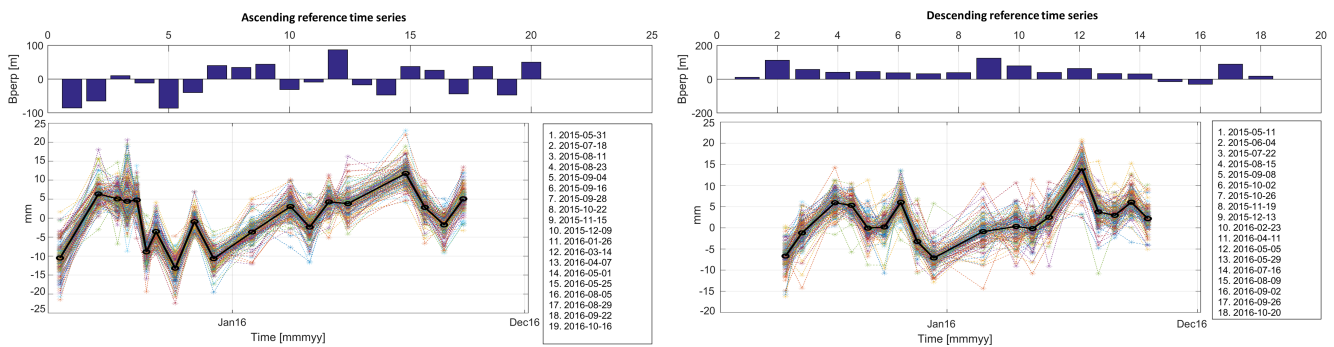


Fig. 5.5: Time series of the reference area within a 250 m radius of  $96.1174^{\circ}\text{E}$ ,  $16.8398^{\circ}\text{N}$  for the ascending track (left) and the descending track (right). The time series of all PS points within the reference area are plotted in coloured lines together with their mean value in black. All the used dates corresponding to the point number are listed on the right of each graphs. The graphs have a similar trend visible on the exact same location which contributes to the confidence in the data.

In the ascending stack, the interferogram of June 24th, 2015 was rejected as it was deemed too unreliable. The choice for the reference PS is based on a few criteria applied to the original results presented in Fig. 5.4, where the reference time-series was set to the city average PS. There is no reason for expecting major uplift, thus one of the blue LOS velocity areas on the left and a very low velocity standard deviation chosen from the right seemed the best available choice for a reference. Additionally an area with low expected groundwater extraction close to surface water finally led to the choice of  $96.1174^{\circ}\text{E}$ ,  $16.8398^{\circ}\text{N}$  with a 250 m radius as reference area for individual time series. The chosen reference time-series can be found in Fig. 5.5.

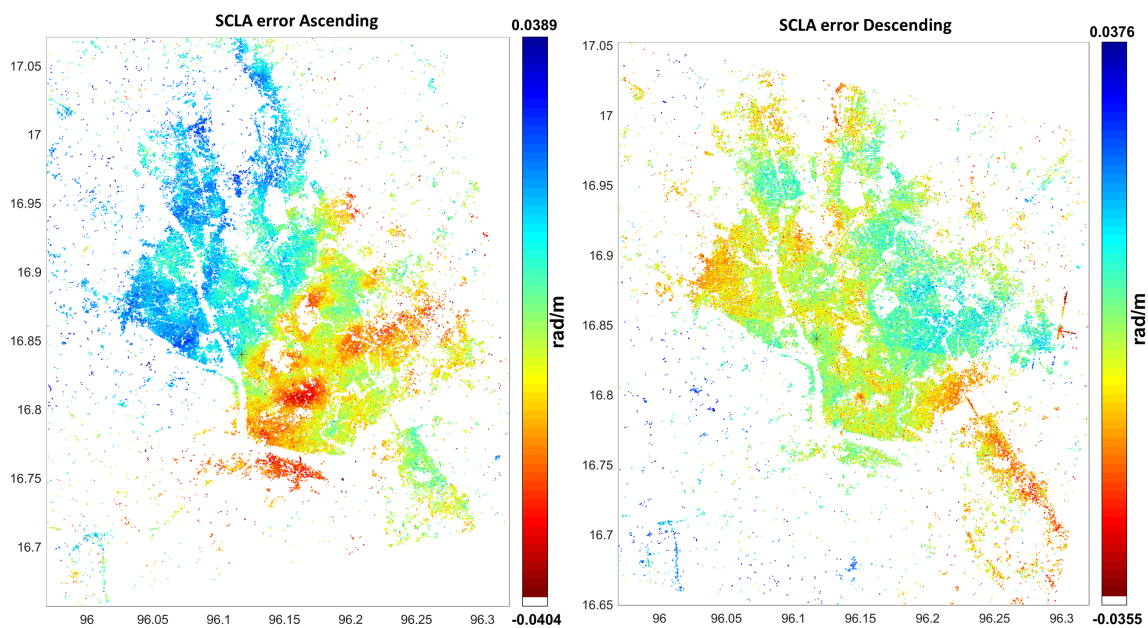


Fig. 5.6: SCLA error for both ascending (left) and descending (right) tracks with unit  $\text{rad}/m$  with  $m$  in the direction of  $B_{\perp}$ . Incorporated in this error is the error between the DEM and the measurement, the error in the DEM itself and incorrect mapping of the DEM into radar coordinates.

In the PSI analysis an estimate is made of the SCLA, also referred to as DEM error, which is the part of the phase that is both spatially correlated and scaling proportional to the  $B_{\perp}$ . This DEM error consists mainly of the spatially correlated part of: the difference in the measurement and the DEM, the DEM itself, and the incorrect mapping of the DEM into radar coordinates. Although referred to as DEM error, the SULA which also holds a small part of the DEM error is not incorporated in this results. The  $B_{\perp}$  varying SCLA error is presented in Fig. 5.6. One would expect the SCLA error to show similar results for the ascending and descending track, but this is clearly not the case when considering this figure. This is actually caused by an incorrectly

geo-referenced DEM into StaMPS for the descending track, which could not be corrected for easily. The ascending SCLA error is considered to be correct as no errors were detected in geo-referencing. These SCLA estimations were used for enhancing the velocity results by subtracting them from the unwrapped interferograms.

## 5.2. Decomposition

The decomposition of the LOS velocities into vertical velocity and horizontal surface velocity is shown in Fig. 5.7. On the right side of the figure, the ascending and descending data point locations are shown in red and blue with the overlapping points where the decomposition was calculated indicated in green. The actual decomposition of these green points is shown in the left of this figure where the colours indicate vertical displacement velocity and the vectors horizontal displacement velocity in the assumed displacement direction. The horizontal deformation is assumed to be directed in the Azimuth Look Direction (ALD) of the ascending satellite. An interesting observation can be made in the east of the city where relative displacements up to 90 mm/ y with respect to the reference are observed. The subsiding cone stretches out for a few kilometres and appears to be circular.

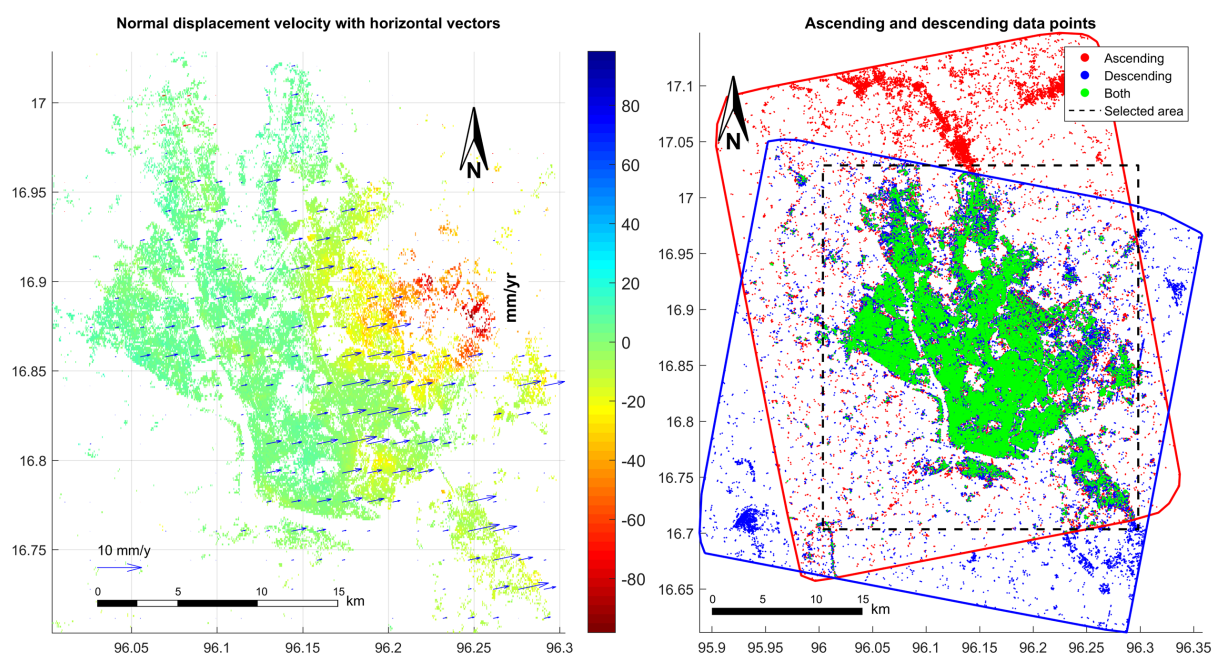


Fig. 5.7: Decomposition of the LOS velocities into horizontal and vertical displacement velocities. The figure on the left shows vertical displacement velocity in colour with horizontal displacement velocities as blue vectors in the assumed direction  $78^\circ$  clockwise with respect to north. The right figure shows the locations of ascending and descending PS points in red and blue with additionally green where they overlap.

Before the actual decomposition was performed, the offset was calculated using the 'quality of fit' of the descending stack onto the ascending stack. A visual representation of the offset determination is shown in Fig. 5.8 where different scales were used to determine the correct offset value. The normalized scores indicate the fit quality and the highest value was found at the correct x and y offset being  $-4 \times 10^{-4}^\circ$  Lon and  $3.6 \times 10^{-4}^\circ$  Lat respectively for which approximately 10 % more data was used than without using the offset.

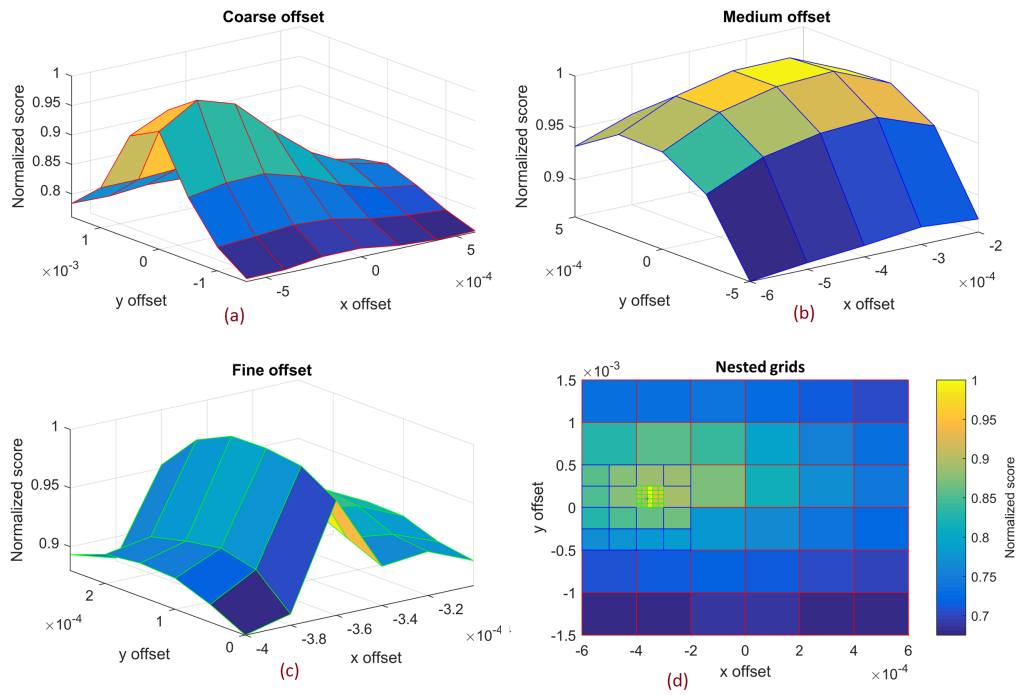


Fig. 5.8: The figure shows the normalized quality of fit scores versus x and y offset values at multiple scales. The coarse (a), medium (b), and fine (c) offsets were determined using a longitude spacing of  $1/5000^\circ$ ,  $1/10000^\circ$ , and  $1/50000^\circ$ , and a latitude spacing of  $1/2000^\circ$ ,  $1/4000^\circ$ , and  $1/20000^\circ$ . A top view of the nested coarse medium and fine offsets is shown in (d).

### 5.3. Ground water extraction

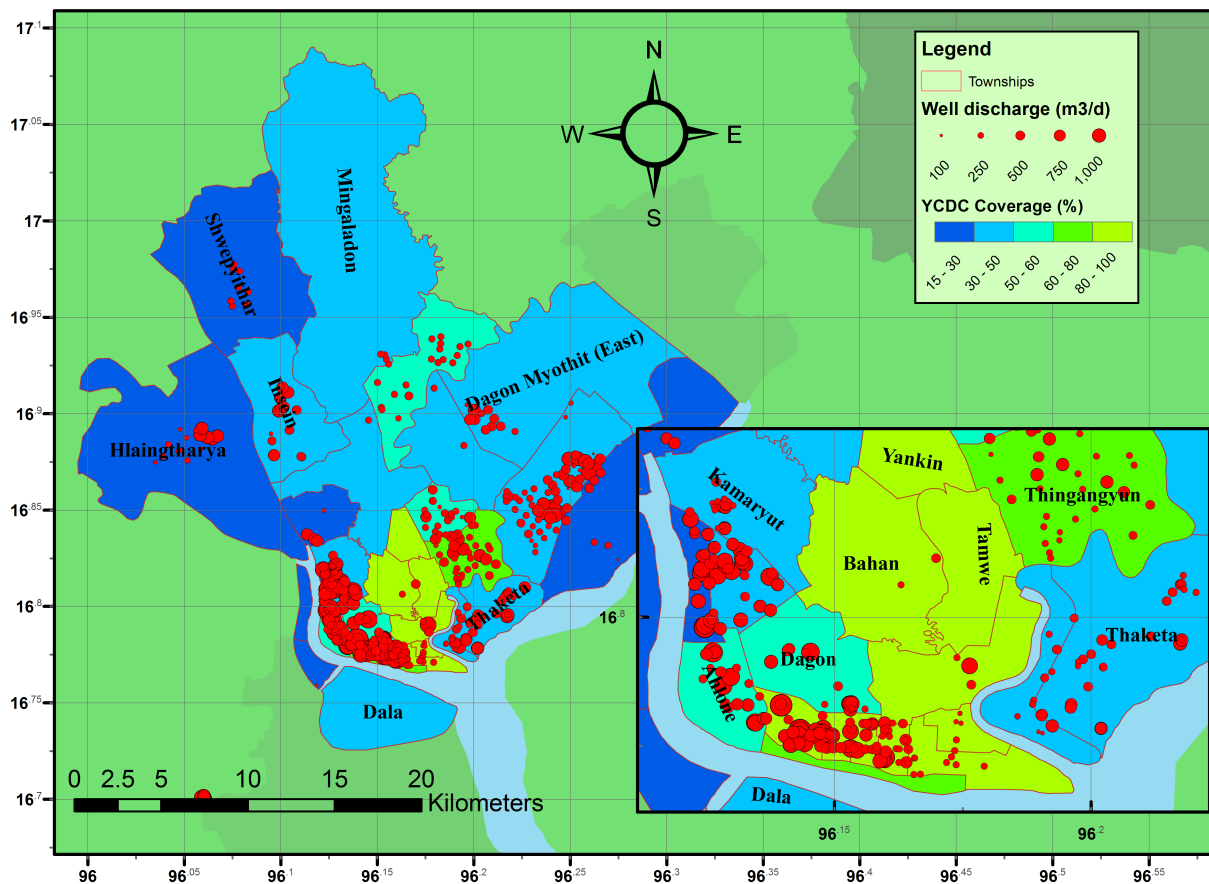


Fig. 5.9: Groundwater extraction capacity by YCDC tube wells highlighted with red dots and percentages of piped coverage specified by township in colour. The bottom right corner shows an enlarged view over the old town centre where the largest density of pumps is found and where most inhabitants rely on piped water.

The georeferenced YCDC-managed extraction wells with their discharge capacity are mapped as red dots on the townships of Yangon in Fig. 5.9. In this figure the townships are coloured based on the percentage of inhabitants receiving water from the piped reservoir system. Surprisingly, the amount of YCDC-managed wells is highest at the locations where inhabitants are connected to the reservoir system, which are the townships highlighted in green. This might be explained by the fact that the pumped water is not used locally but transferred to a treatment plant first. The expanded parts of the city are less well covered by the YCDC wells than the older parts of town.

The combined discharge capacity of the wells in Fig. 5.9 is much more than the actual extracted groundwater according to various sources (YCDC & JICA, 2013; YCDC, 2014; Mon et al., 2013). The actual extraction is therefore estimated by correcting the discharge capacity for idle time through scaling the total amount of extracted water to the 20 MGal/d. There is no additional information to support the extraction scheme for each pump, so the daily discharge is estimated by linear scaling of the discharge capacity. The values of capacity and estimated extraction per township are listed under 'Q YCDC' Table 5.1.

For the private well extraction, the estimate is derived from the complement of the YCDC piped system coverage through equation (4.7) using a water demand of 135 L/p/d as found in the 'water demand survey'. The combined information results into the discharge estimate for private-well owners such as listed under 'Q Priv' in Table 5.1. Both the extraction by YCDC-well and private-well estimates are mapped in pie-charts onto the townships of Yangon in Fig. 5.10.

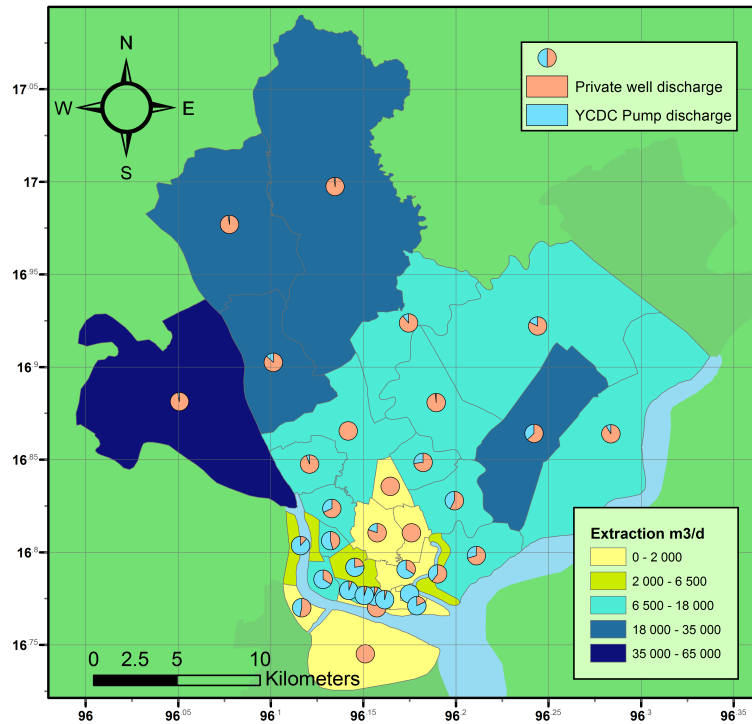


Fig. 5.10: Absolute groundwater extraction distribution estimate per township divided into residential (private) wells and YCDC managed wells presented as pie charts. The colour relates to the amount of groundwater that is extracted in each township. These results do not account for industrial water that may also be extracted.

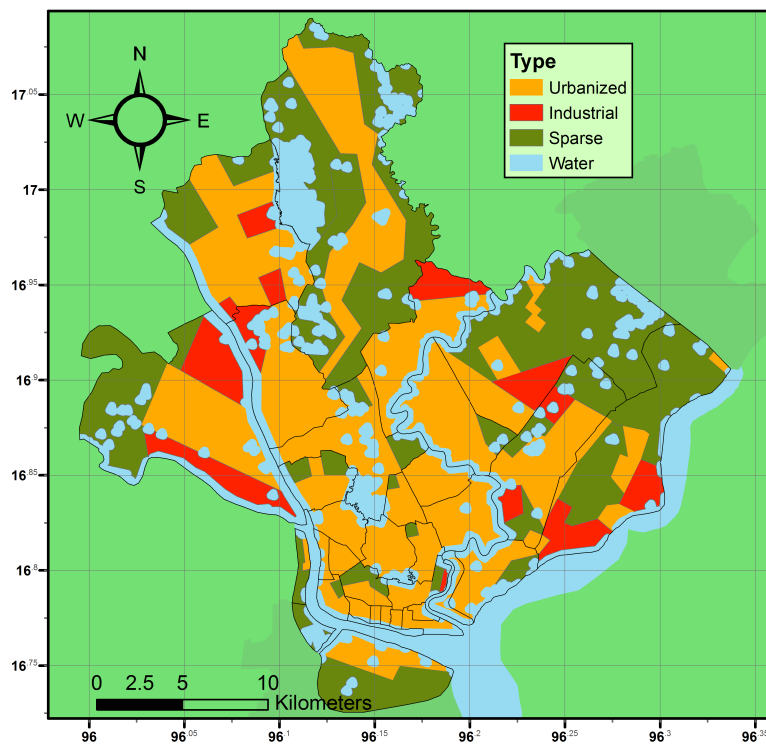


Fig. 5.11: Land use of Yangon divided into densely urbanized residential area in orange, industrial zones in red, sparsely inhabited or agricultural area in green and water body buffer in blue. This data was derived from visual inspection of Google Earth images acquired in 2016.

The absolute groundwater extraction as displayed in Fig. 5.10 does not allow for easy comparison since the townships each have a different area and population. Therefore the extracted daily discharges were normalized by area first, so a flux in mm/d was obtained. The division of Yangon into different land-use types is shown in Fig. 5.11 in which Urbanized is the land-use type where most extraction of both public and private wells is expected. The urbanized area is calculated for each township and listed under 'Area urb' in Table 5.1. In this table, the total discharge 'Q tot' composed of 'Q YCDC' and 'Q Priv' is divided by the urbanized area to obtain the normalized extracted discharge 'Q norm' which is also mapped onto the townships in Fig. 5.12.

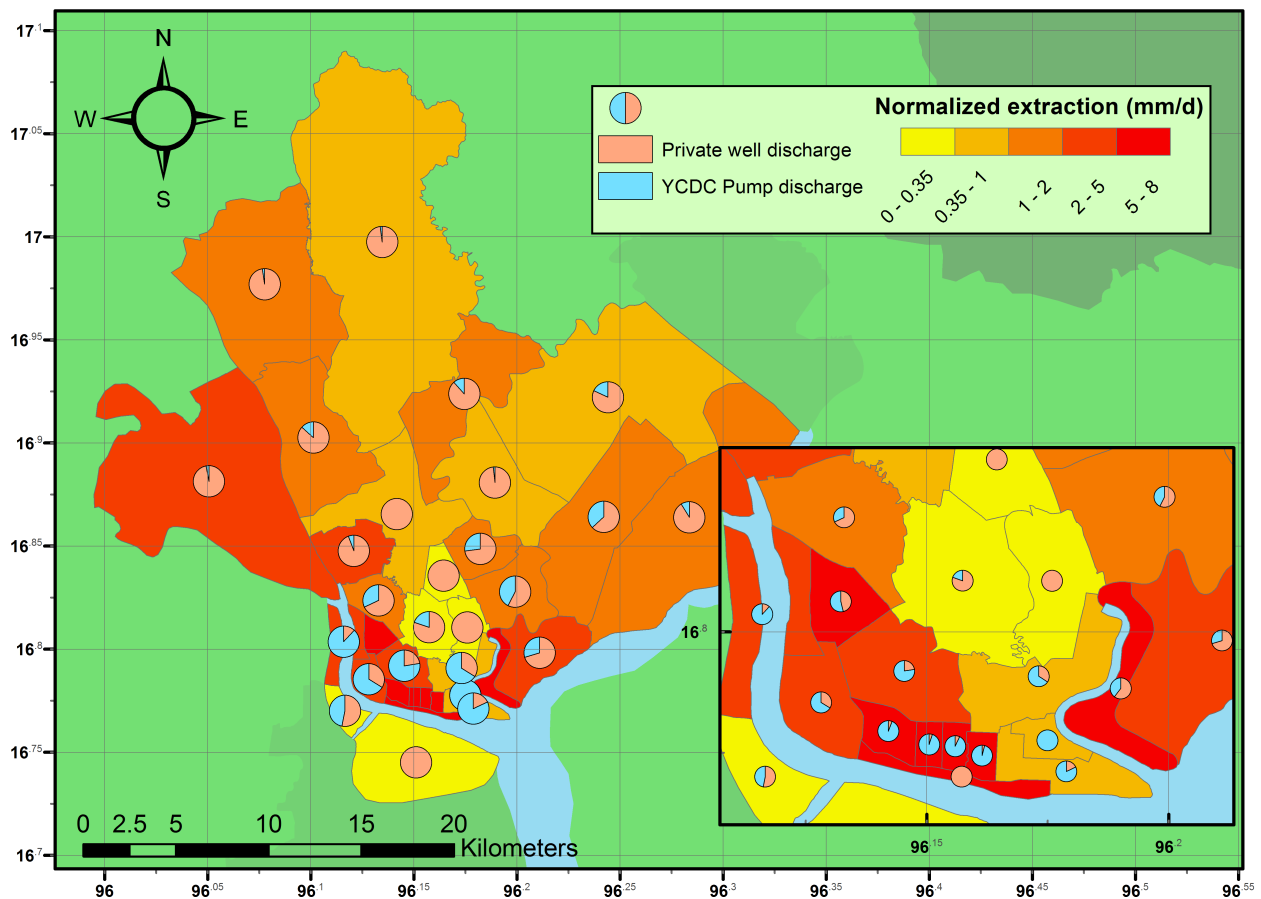


Fig. 5.12: Groundwater extraction estimation distributed over residential extraction and YCDC managed extraction normalized over the urbanized township area. In this figure, industrial groundwater extraction is not taken into account.

In Fig. 5.12, one observes that most of the groundwater is extracted in the old city centre near 16.78° N and 96.15° E as shown in the zoomed part of the figure. Most of this extraction is composed of YCDC well extraction and only very little private extraction. Towards the more recent expanded city areas, most of the extracted groundwater is composed of private wells. One possible significant contributor to groundwater extraction is the industrial component which is not taken into account in this research because of a lack in available data.

Table 5.1: Ground water usage in Yangon specified per township. The townships are mapped in Fig. 5.13 with their name or number for easy referencing. 'Coverage' specifies the percentage of inhabitants receiving piped water, 'Pop' stands for population, 'C YCDC' is the maximum capacity of YCDC pumps combined, 'Q YCDC' the estimated daily extraction, 'f\_priv' the estimated factor of private well owners, 'Q Priv' the estimated private well extraction, 'Area urb' the densely urbanized area, 'Q tot' the total daily extracted groundwater and 'Q norm' the urban-area normalized extraction

#	Township	Coverage %		Pop * 1000	C YCDC $m^3/d$	Q YCDC $m^3/d$	f Priv -	Q Priv $m^3/d$	Area urb ha	Q tot $m^3/d$	Q norm mm/d
		2011	2014								
1	Ahlonge	45	55	55.4	18330	6110	1	3116	192.34	9226	4.8
2	Bahan	80	90	96.7	760	253	0.85	1027	680.97	1280	0.2
3	Bothtaung	90	92	40.8	2780	926	0.5	203	164.7	1129	0.7
4	Dagon	57	60	25.6	13260	4420	1	1280	233.76	5700	2.4
5	Dagon My. (E)	18	40	165.5	5706	1902	0.7	8688	1306.27	10590	0.8
6	Dagon My. (N)	23	40	203.9	600	200	0.7	10704	1674.08	10904	0.7
7	Dagon My. (Sei.)	10	20	167.4	2900	966	0.6	10044	842.22	11010	1.3
8	Dagon My. (S)	24	45	371.6	29040	9680	0.65	16605	1680.91	26285	1.6
9	Dala	25	45	173.4	0	0	0.03	357	676.57	357	0.1
10	Dawbon	24	50	75.0	4590	1530	0.5	2343	73.56	3873	5.3
11	Hlaing	15	30	160.0	2420	806	0.95	13299	509.44	14105	2.8
12	Hlaingtharya	12	22	686.8	6100	2033	0.95	63614	2285.64	65647	2.9
13	Insein	24	40	305.7	10090	3363	0.95	21781	1944.57	25144	1.3
14	Kamaryut	13	40	84.4	9000	3000	1	6330	505.8457	9330	1.8
15	Kyauktada	95	96	29.8	11180	3726	1	148	59.26	3874	6.5
16	Kyeemyindaing	14	25	11.6	17050	5683	0.7	761	164.82	6444	3.9
17	Lanmadaw	84	90	47.1	24710	8236	0.9	529	114.24	8765	7.7
18	Latha	90	93	24.9	10530	3510	0.85	185	48.57	3695	7.6
19	Mayangone	34	45	198.0	330	110	0.95	12931	1423.21	13041	0.9
20	Mingaladon	14	45	332.5	1310	436	0.95	21716	4003.69	22152	0.6
21	Mingalartau.	92	96	132.2	3820	1273	1	660	271.86	1933	0.7
22	North Okkalapa	23	60	332.9	5890	1963	0.9	14980	1585.07	16943	1.1
23	Pabedan	92	94	33.3	10150	3383	1	249	53.31	3632	6.8
24	Pazundaung	94	96	48.2	1470	490	0	0	69.65	490	0.7
25	Sanchaung	40	45	99.8	24110	8036	1	6861	240.35	14897	6.2
26	Seikgyikan.	13	20	34.0	90	30	0.01	34	0	64	0.0
27	Seikkan	56	80	2.8	0	0	1	70	0.879	70	8.0
28	Shwepyithar	6	15	343.3	2620	873	0.95	34651	3106.96	35524	1.1
29	South Okkalapa	25	60	161.0	7170	2390	0.8	6440	695.29	8830	1.3
30	Tamwe	86	92	165.4	0	0	0.9	1488	407.02	1488	0.4
31	Thaketa	13	35	220.4	15820	5273	0.7	12535	721.31	17808	2.5
32	Thingangyun	48	70	209.3	13910	4636	0.8	6279	934.35	10915	1.2
33	Yankin	82	88	71.0	0	0	0.9	958	411.2	958	0.2

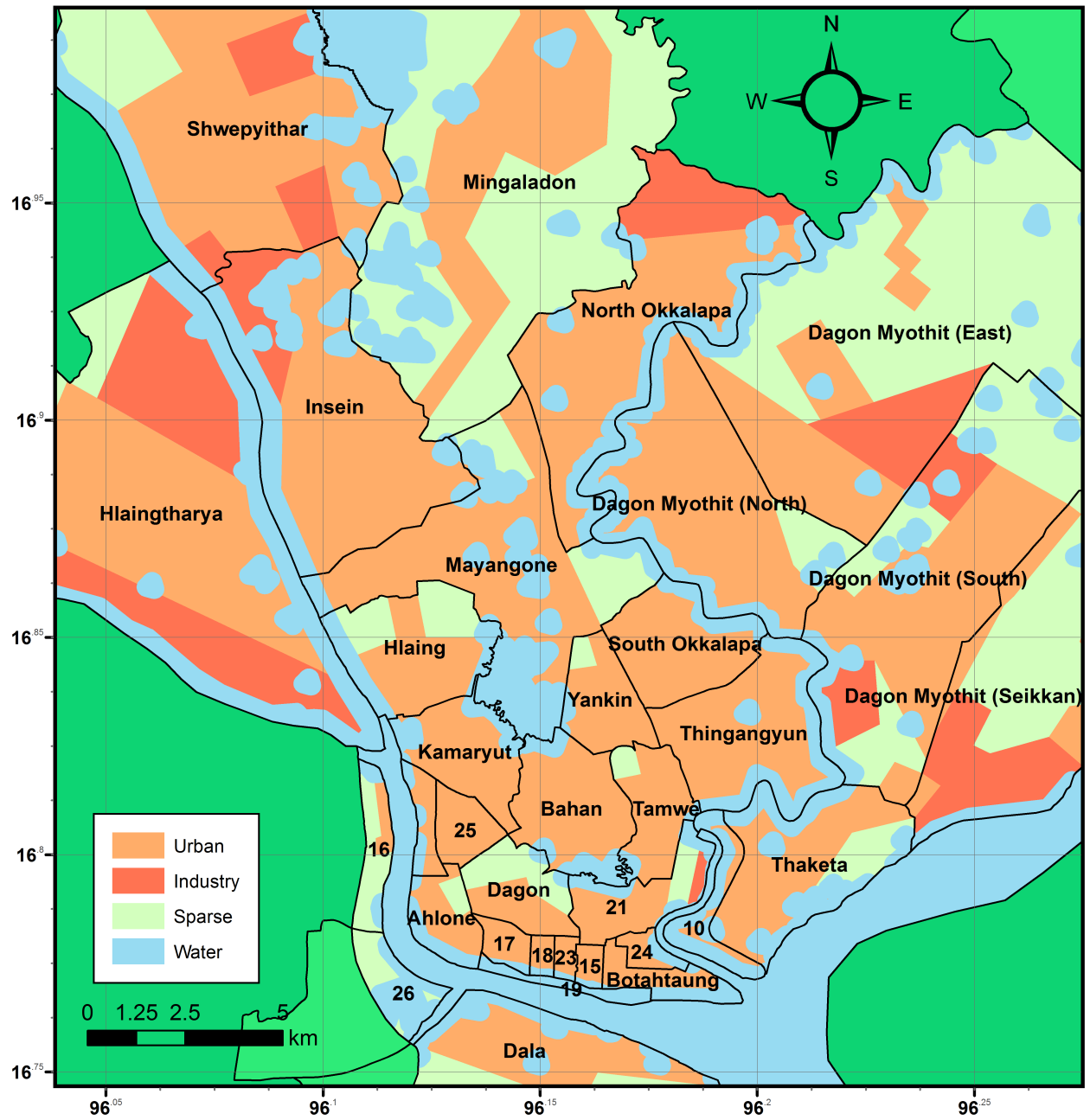


Fig. 5.13: Townships indicated with name or number corresponding to Table 5.1. The legend entries indicate the land-use classification which is the same as displayed in Fig. 5.11. The borders of the townships are delineated with a solid black line.



# 6

## Discussion

In this section, the acquired results will be reviewed for their quality and shortcomings with respect to the research question. The water resources and InSAR will also be connected in this chapter, and other possible source contributors to subsidence will be discussed. Where applicable, recommendations will be given for possible improvements.

### 6.1. S1 processing output

Applying InSAR for the city of Yangon results in coherent interferograms over the urban area. There is an increasing amount of SAR images available in ascending and descending tracks over the city of Yangon. Currently, once every 24 days a new image is available for each track, and once S1B starts acquiring alongside with S1A, new images will be available every 12 days. Furthermore, the required conditions under which InSAR can successfully be applied for the S1 sensors and the area of Yangon city are met. First of all, Geometric decorrelation is rarely an issue since the  $B_{\perp}$  is very small, almost never higher than 200 m. Second, Temporal decorrelation, due to varying motions of scatterers within pixels, appears to be the most dominant limitation for the use of InSAR. Especially measurements in the areas without stable buildings or infrastructures, often delta or agricultural areas, are affected by incoherent phase contributors dominating the pixel behaviour. In general, the urbanized area is coherent and bright scattering throughout the year while non-urbanized area is not. There is a clear influence of the monsoon, in agreement with (van der Horst, 2016) and visible in the delta areas as shown in Fig. 6.1 where strong phase-stability in the delta is found in the dry season which is absent in the wet season. Direct interpretation of subsidence from differential interferograms proved to be tricky since the APS dominates the subsiding signal.

The processing of S1 images posed several problems that needed to be overcome. Firstly, some of the images turned out corrupted because of stalling or incorrect downloads. Re-downloading solved this problem in all instances, since an alternative servers sometimes provided the desired product. Secondly, the co-registration occasionally failed when using the frequency domain cross-correlation offsets in incoherent areas. Therefore, the offset determination was performed using magnitude cross-correlation. Thirdly, the Enhanced Spectral Diversity (ESD) correction proved to be challenging for incoherent areas. Other means of refined co-registration such as spectral diversity are currently not available in the Doris v5 beta version while they might provide the solution for this problem. Currently, the only way of mitigating this problem is using different ESD settings based on visual inspection of phase jumps in differential interferograms.

### 6.2. PSI and decomposition assessment

PSI processor StaMPS served as an excellent tool for analysing PS time-series for Yangon, especially since the interferograms could not directly be interpreted for subsiding signals. The number of interferograms is usually the factor determining the success of PSI algorithms. In this research, the 19 ascending and 18 descending interferograms suffice to produce similar deformation patterns which confirm that the unwrapping output is consistent. As stated earlier, StaMPS succeeded to select PS candidates with only 12 images or less, but reliable output of the unwrapping requires more, preferably 25 or over (Hooper et al., 2007).

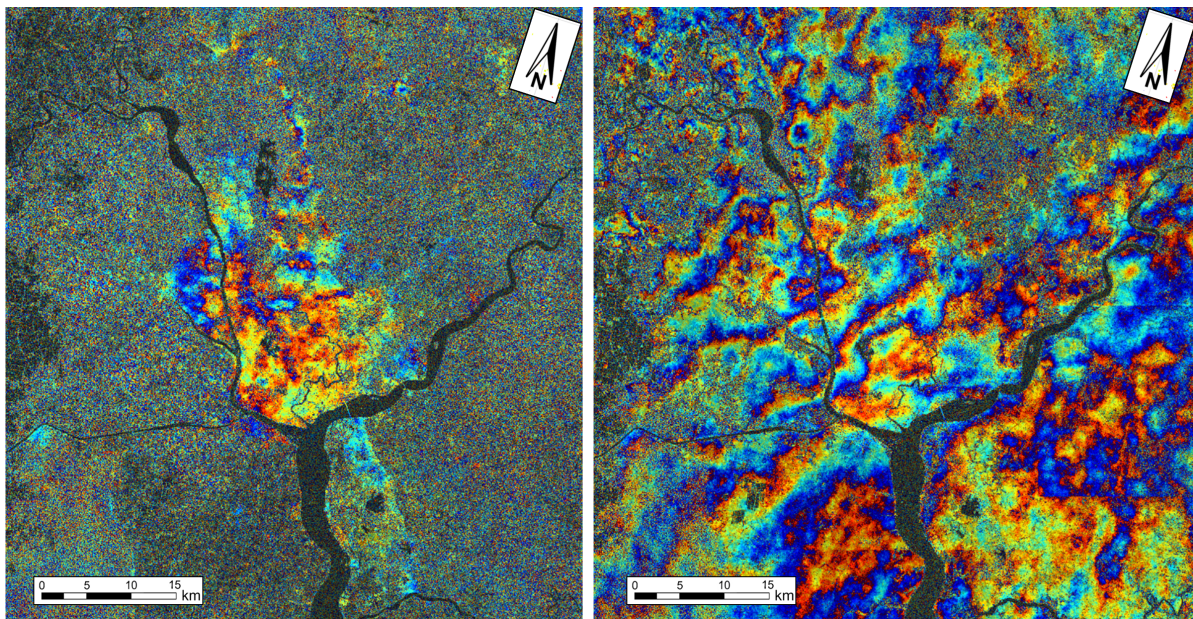


Fig. 6.1: Samples of cascaded interferograms of the ascending track with master and slave dates 2015-07-18 & 2015-08-11 during the monsoon on the left and 2016-04-07 & 2016-05-01 during the dry season on the right. The images were multi-looked with factors 20 in range and 4 in azimuth. Colours relate to wrapped phase values and the brightness relates to scattering intensity. A clear difference is observed outside the urbanized areas of Yangon where temporal decorrelation (randomly coloured areas) in the dry season is much less present than during or directly after the monsoon.

Another reason to interpret the presented values with caution is the fact that only little more than one year's worth of data has been analysed. It is therefore difficult to interpret yearly averaged subsidence rates as true average velocity. Instead of considering the velocity values, one should rather focus on the order of magnitude that is presented.

The choice for reference PS time-series was based on the best available option concerning velocity and standard deviation. An improved method would rely on correcting for a reference point of which the velocity is known using, for instance, Global Positioning System (GPS). The presented values can be considered as relative to the reference area within a 250 m radius from  $96.1174^{\circ}$  E and  $16.8398^{\circ}$  N. One should take in mind that this reference was not corrected for noise and atmospheric phases present in the slave images. This means that the subtraction of the reference PS introduces small errors in the individual time-series and the velocity estimation. There is no easy way of getting around this fact, but choosing a low standard deviation reference time-series will most likely result in a better estimation than using the default settings. Improved methods for setting the reference time-series have been developed at the TU Delft (R.F. Hanssen, personal communication, Jan 23, 2017), and could be of use for future research.

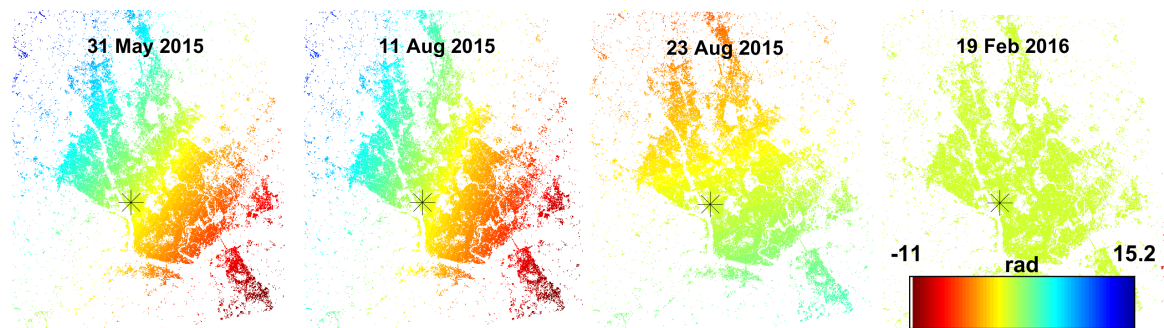


Fig. 6.2: Several orbital ramp estimations for the ascending orbit track. The direction and magnitude of the ramps do not correspond to typical ramps that can be expected from S1. The estimation seems to include ramps in the atmospheric contribution present in the slave images, which is supported by the fact that around 10 cm of phase delay is shown in these figures.

Implemented in StaMPS is a method to estimate the orbital ramps which can be subtracted from the unwrapped phases to improve the velocity results. In essence, this method estimates two-dimensional linear ramps in the unwrapped phase space. The results from this estimation are not used as they seem to be estimated incorrectly as shown for the ascending track in Fig. 6.2. It appears that in stead of orbital ramps, the atmospheric ramps are estimated considering the magnitude and direction of the phase-ramps. Since these are in general not linear, it would not be appropriate to correct for this estimation and it is therefore left out.

The decomposition accuracy is dependent on several of the above stated factors. First, the quality of decomposition depends largely on the accuracy of the velocity measurements. Second, the reference time-series influence the results as they could be moving themselves. The choice of reference especially affected the direction and magnitude of the horizontal velocity components while the vertical decomposed velocity was only slightly affected by the choice of reference location. Therefore, no conclusions will be based on the horizontal velocity decomposition. Another factor that influences the decomposition results is the assumed direction of motion,  $\gamma$ , which might be chosen incorrectly, but Fig. E.1 and Fig. E.1 in Appendix D show that the choice for the horizontal deformation direction does not influence the vertical velocity significantly as long as directions close to north are avoided. Using typical S1 values such as  $\theta = 40^\circ$  and  $\alpha_a = -12^\circ$ , the sensitivity to the chosen direction can be calculated by substituting these values into (4.3) obtaining

$$v_{LOS} = [0.76, 0.13, -0.63] \cdot [v_u, v_n, v_e]$$

which shows low sensitivity for the north direction. Therefore, avoiding the displacement direction assumption 'north' was done correctly.

### 6.3. Fieldwork validation

Near the end of this research, some visuals were collected in one of the townships showing significant subsidence. All of the pictures were taken in Dagon Myothit (South) and were georeferenced using a GPS application. Eight of these pictures were selected to be placed in this chapter for they might point to effects caused by subsidence. Each picture is labelled with a number and their corresponding location is shown in Fig. 6.3. Picture numbers one through three are shown in Fig. 6.4 and picture numbers four through eight are shown in Fig. 6.5. All of the visuals were collected by Boy-Santhos van der Sterre.

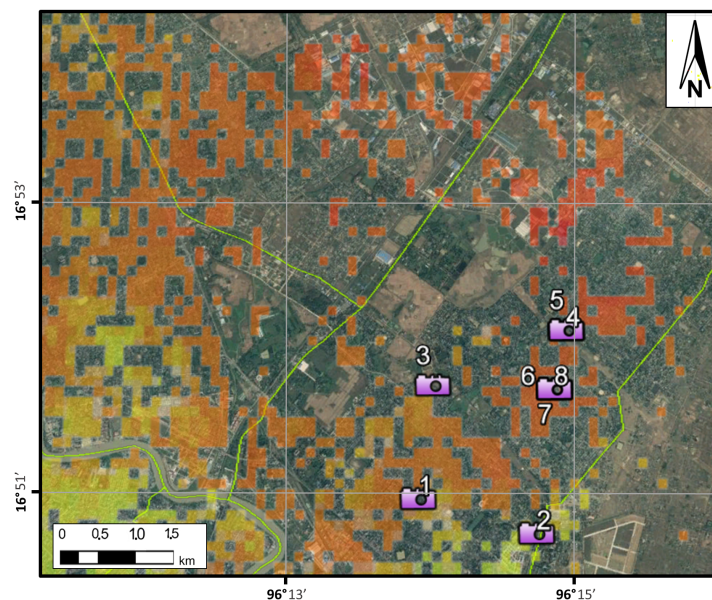


Fig. 6.3: The locations of the collected visuals presented in Fig. 6.4 and Fig. 6.5. The coloured raster corresponds to the decomposed subsiding velocities such as found in Fig. 5.7. The background image is optical satellite imagery supplied by Google Earth, 2017.



Fig. 6.4: Visuals on possible effects of subsidence. Picture one and three show sloped terrain near a possibly founded structure. In case of subsidence, the structures remain in place while the surrounding areas gradually go down. Picture two shows damage that may result from differential surface motion. The locations of each picture are shown in Fig. 6.3. Source: Boy-Santhos van der Sterre



Fig. 6.5: Visuals on possible effects of subsidence. Picture four shows differential surface motion in a road. In picture five, a level is indicated which might show a previous surface level. Pictures six and seven show parts of structures that are revealing because of a lower surrounding surface. Picture eight shows a possible effect of surface erosion. The locations of each picture are shown in Fig. 6.3. Source: Boy-Santhos van der Sterre

In the pictures shown in Fig. 6.4 and Fig. 6.5, one observes possible effects caused by subsidence. Especially the differential motion seen in several images could point to these effects. Though these pictures do not prove the existence of subsidence, they do show signs of deterioration. Because there is no information regarding the original situation, it is hard to determine the significance and deterioration speed.

One final remark stated that there was an incredible amount of recently constructed high-rise buildings and that many construction were still ongoing (Boy-Santhos van der Sterre, personal correspondence, 2017). This could be a possible contributor to measured surface displacement as increased stresses on the soil cause initial settlement to occur.

## 6.4. Groundwater extraction analysis

Very little quantitative data was available on sufficient quality to perform an accurate analysis. Many of the used data sources were not available on a scale smaller than township level and some were inconsistent or incomplete. This was one of the reasons to perform a survey which revealed very useful information. Especially the water demand analysis for private groundwater extraction was improved. The main considerations for the used datasets will be listed below.

For the YCDC tube well dataset, half of the wells were not geo-referenced. Around 200 wells of which the approximate location was known, have been put into their corresponding township. For this reason the assessment could not be made on a scale more detailed than township level. Another limitation within this dataset was that only the capacity for each tube well was listed rather than actual extraction amounts. The assumption that each well is active and extracts around 40% of its capacity is quite strong. Although this assumption leads to a correctly estimated total extraction, it is likely leading to errors in the spatial distribution of extraction. Especially in the old city centre, where the extraction is mainly composed of YCDC wells, it is questionable whether the stated amounts are actually extracted. Unfortunately, no applicable data was available to improve the estimate.

The private well estimation is based on several sources indicating coverage by the YCDC piped system, type of delivery, population, and water demand. For all of these datasets, the finest available scale again was township level. Although a finer scale would be desirable, it was hard to acquire using this approach. However, using the township scale is likely to result in better estimated extraction amounts since all datasets in this scale are provided in reasonable accuracy. The water demand has been set at a fixed value as found through the water demand survey, but in reality the demand depends on several factors including the income, and the ease of obtaining water.

Industrial groundwater extraction might be an important contributor to the total extracted amounts and was not taken into account in this research because the data was unavailable. To the author's knowledge, no governmental agency is occupied with managing industrial groundwater extraction and therefore it will be nearly impossible to assess these amounts without more detailed information from industries themselves.

## 6.5. Correlation of subsidence and groundwater extraction

To assess the relation between surface deformation and groundwater extraction, both have been simplified to one number per township for easy comparison. The normalized extraction as listed under 'Q norm' in Table 5.1 is plotted against the average decomposed subsiding velocity per township in Fig. 6.6. From this figure one observes that both parameters are not correlated. The correlation value corresponding to this figure is  $-0.19$  indicating that on a township level, there is no direct relation between extraction and subsidence. Interesting to see, however, is how all of the subsidence rates over  $10 \text{ mm/y}$  are found in the east of the city. All of these townships concern areas to which the city has recently expanded.

There are three explanations of interest for the non-correlating subsidence and groundwater extraction. Either the subsidence was measured incorrectly, the water extraction was assessed inadequately, or both do not affect each other. The fact that previous results supplied by (Aobpaet et al., 2014) and both ascending and descending tracks show the same pattern supports the confidence in the subsidence results, at least for the order of magnitude that was presented. Therefore, future research should be directed at improving the assessment on water resources or alternative methods to explore possible sources of subsidence. A key to better

understanding the current signal possibly lies in the subsoil. Data that seems essential, but was unavailable for this research is a qualitative description of the different soil types and layers beneath the city of Yangon. It matters significantly which aquifer is used in terms of subsiding potential when water is extracted from the subsoil. In conclusion, there are a lot of factors that might be of influence for subsidence. Groundwater extraction was used as a first order indicator but did not deliver a direct relation to subsidence. Therefore the assessment requires a higher order approach and a consideration for other possible contributors. The latter is discussed in the next section.

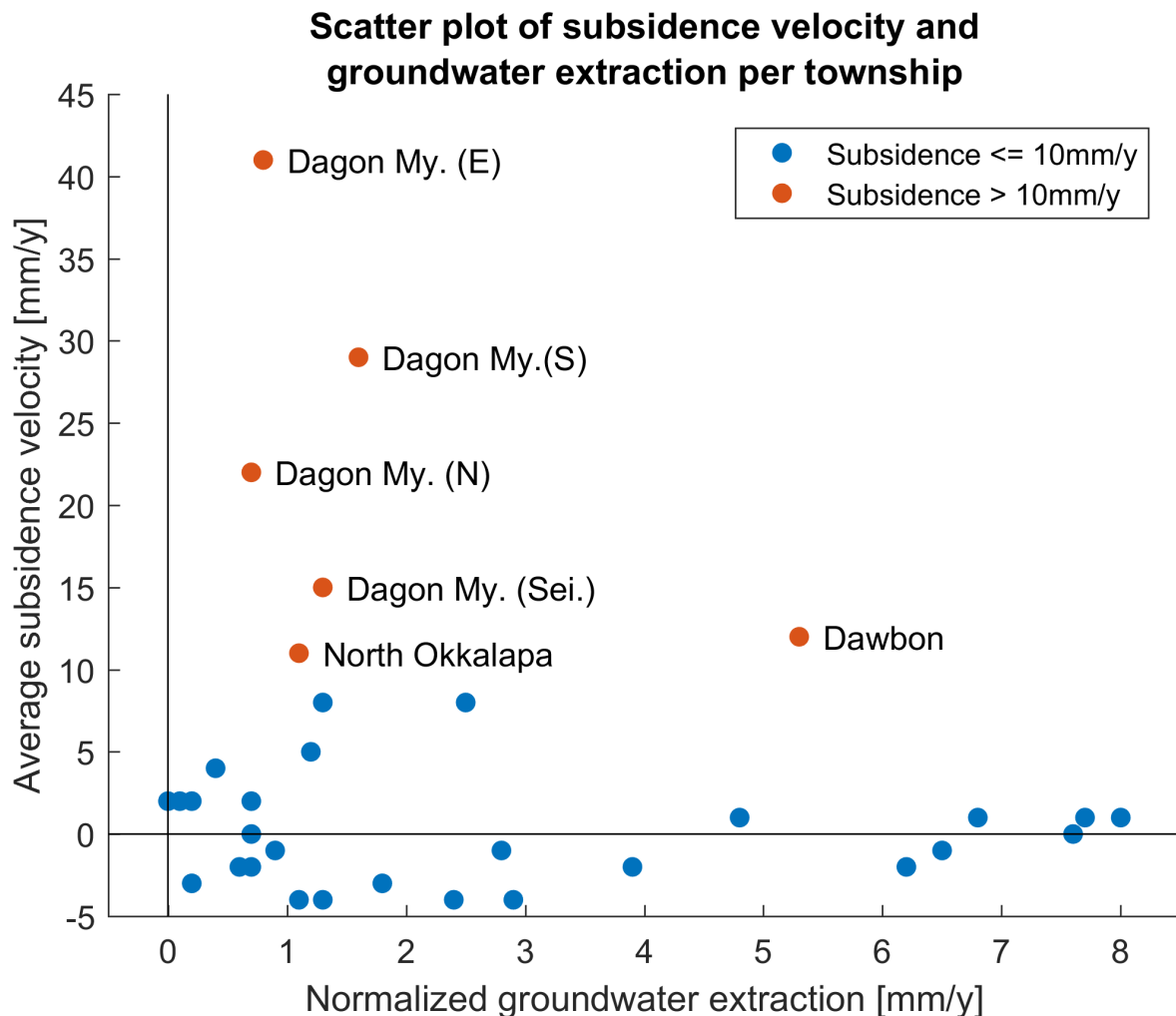


Fig. 6.6: Averaged subsidence versus normalized groundwater extraction on a township scale. The groundwater extraction does not account for industrial extraction. Both parameters do not seem to correlate well with each other.

## 6.6. Qualitative analysis on the measured subsidence

Although the groundwater extraction does not correlate directly with the subsidence, there must be something causing the surface deformation (assuming this is measured correctly). There are a few more considerations which might explain what is causing the observed pattern. In the next paragraph a few of these considerations will be discussed.

The subsidence is mainly found in the Dagon Myothit townships where the city has recently expanded to. Based on historical satellite images, the first expansion of Dagon Myothit North and Dagon Myothit South occurred around 1990. Since then, the urbanized area has been expanding slowly towards the Dagon Myothit East township, each time extending the outer border of the city. Land surface that was previously used for agriculture was interchanged for houses and industrial areas. From 2000 onwards, there was also densifica-

tion in the surface occupied by buildings. Since 2010, the densification and expansion grew more rapidly than before, especially in the industrial areas, which might have been a result of the change in political situation (see Appendix A).

The major change in land-use can have multiple effects on the stability of the land surface, other than the increase of groundwater extraction as covered by the previous part of this thesis. First, the amount of recharge (water that is able to reach the groundwater table) reduced since the amount of impervious area increased significantly. The amount of impervious area observed in the subsiding areas varies between 80 % and 90 %<sup>1</sup> thereby reducing the deep infiltration by a factor five with respect to the original situation when comparing with the situations described by Ruby (2005). Second, the placement of structures on previously unloaded soil causes settlements. Although this is not actual subsidence, it still contributes to the measured surface deformation as the usage of PSI usually relies on measuring movement of structures. The placement of a structure first causes initial settlement in the unsaturated or highly conductive part of the soil which typically takes place within days after applying the load. Another kind of settlement is consolidation which typically occurs in highly saturated soil types with low conductivity such as clay. This kind of settlement has a typical time scale of three to ten years (WebTeckTix, 2014). Fig. 6.8 shows an example of a recently built structure for which a vertical velocity of 4 cm/y was found. When inspecting the LOS velocity enlargement displayed in Fig. 6.7, some spatial variability is detected on scales of hundred meter. This may indicate that there is differential motion between buildings caused by settlements.

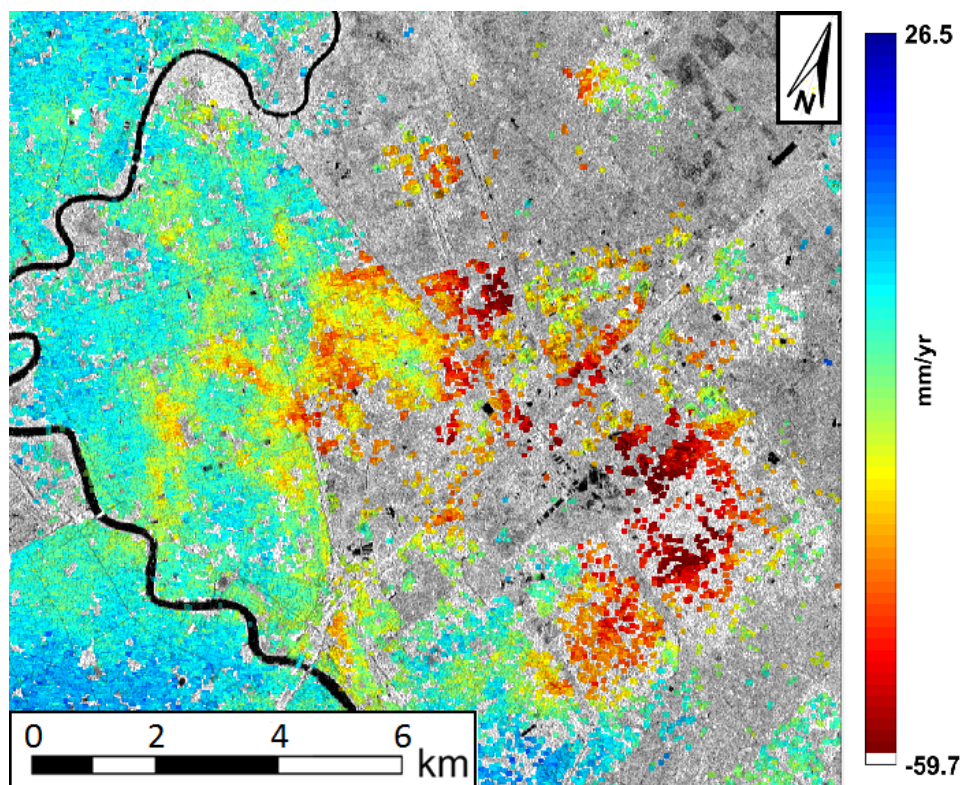


Fig. 6.7: An enlarged view over the subsiding area in Dagon Myothit (Area indicated with '1' in Fig. 5.1) with the ascending LOS velocity in coloured scatter points. The background shows the interferometric amplitude with low and high represented by black and white respectively. The scatter is plotted on radar coordinates which is why longitude and latitude information is not displayed.

The upper layer of the surface might also be susceptible to surface erosion during pluvial floodings which have been reported by JICA (2014b). Flooding events in this area occur twice or three times per year with local water levels between 1.5 m and 2.0 m. Picture 8 in Fig. 6.5 is likely to show an example of surface erosion. The shallow subsurface might also be affected by the practice of ongoing drainage necessary to sustain an

<sup>1</sup>Based on visual inspection of Landsat imagery.



Fig. 6.8: Before and after images for the construction of a compound for which a surface deformation velocity of 4 cm/y downwards was measured. This structure is located at 16°55'27" N and 96°9'31" E.

habitable urban environment. Depending on soil characteristics, this drainage can have a long-term effect on the degradation of the upper layer of the soil if it consists of peat (Cuenca & Hanssen, 2008). To quantify the effect of this possible cause, information regarding soil characteristics is necessary.

Although previous suggestions indicate possible sources for shallow subsurface subsidence and settlements, there are also indications for deeper subsidence activities. When considering the vertical surface deformation velocity in Fig. 5.7, one observes a large area which appears to be circular. The radius of this deformation pattern stretches several kilometers from the center, although it is difficult to determine what happens east from it as little PS points are present in that area. This smooth displacement pattern corresponds to a cone of depression resulting from groundwater pumping activities. An attempt is made to quantify how this cone of subsidence can be explained by the extraction of groundwater. First of all, the volume of subsidence is calculated by integrating over the interpolated vertical velocity in the subsiding cone which is visualized in Fig. 6.9. The volume of subsidence derived from this figure equates to  $5.9 \times 10^6 \text{ m}^3/\text{y}$  equating an average subsiding velocity of 40 mm/y when considering extraction from the area centered at 16.89° N and 96.23° E with a radius of 5 km.

Let's assume that this 40 mm/y of subsidence is indeed caused by water extraction and make an attempt to model the amount of exaction necessary to effectuate this amount of subsidence. This assessment should by no means be taken as interpretation of the reality since many assumptions were made in order to derive extraction amounts from subsidence measurements. First of all, a soil layer configuration is assumed with alternating sand and clay layers. The configuration of this assumed soil model is presented in Table 6.1. Next, The subsidence is a continuous process that can be explained by a consolidation present in compressible layers in the subsoil. For the subsidence calculations, the formula of Koppejan for secondary settlement<sup>2</sup> (Verruijt, 2012) is used:

$$\Delta h_i = h_i \cdot \frac{1}{C_s} \cdot \log\left(\frac{\Delta t}{1 \text{ day}}\right) \cdot \ln\left(\frac{\sigma_i + \Delta\sigma_i}{\sigma_i}\right) \quad (6.1)$$

with  $h_i$  as the soil layer compression in m,  $C_s$  the coefficient of secondary settlement,  $\Delta t$  the time in days after applying the load,  $\sigma_i$  the original effective soil stress in Pa, and  $\Delta\sigma_i$  the increase in effective soil stress in Pa for layer number  $i$ . First the original stress situation is calculated under the assumption of hydrostatic pressure throughout the soil profile. Then water is assumed to be extracted from the middle layer, thereby lowering the water stress to zero in the top of this layer and increasing the effective stress accordingly. The

<sup>2</sup>The primary settlement is not taken into account for this calculation since it is most likely not present in the PSI results

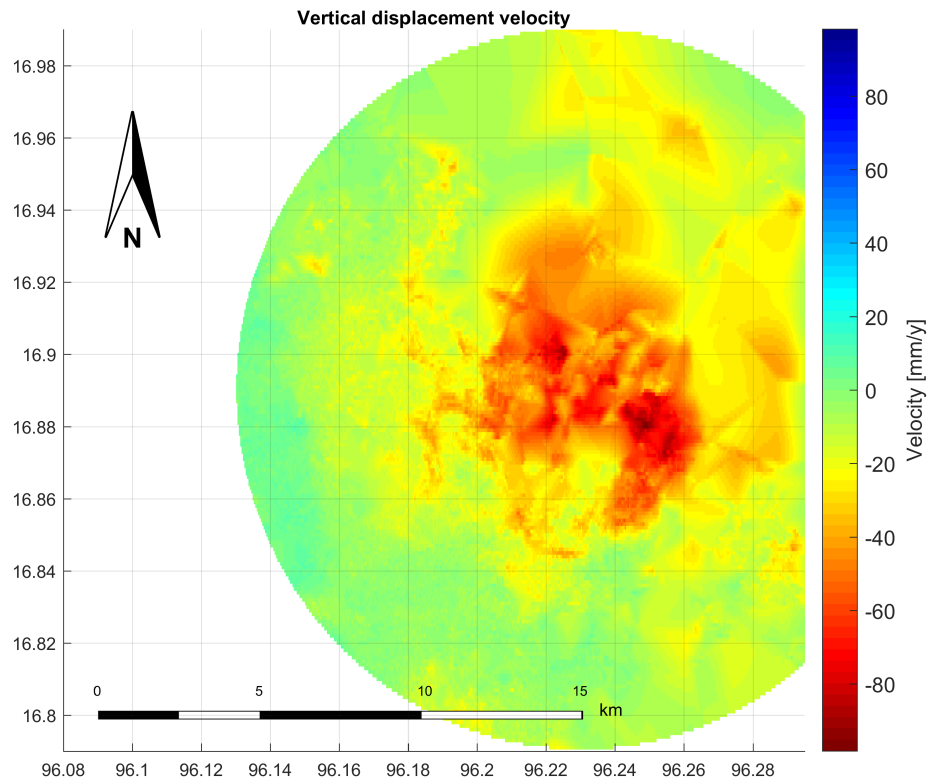


Fig. 6.9: Interpolation of the vertical surface deformation in the Dagon Myothit subsiding area. These values were integrated in space to obtain a total subsidence volume of  $5.9 \times 10^6 \text{ m}^3/\text{y}$ .

stress profiles calculated according to the above stated description are presented in Fig. 6.10. In this figure on the right are the calculated subsidence profiles using equation (6.1) for the first ten years after applying the change in water stress. In the bottom of the figure the cumulative subsidence for each year is presented from the third year onwards. The first two years are not considered since the pre-consolidation value, which is difficult to estimate, largely determines the initial amount of secondary settlement. Therefore only the instantaneous subsidence values in subsequent years are considered to be of interest. When the assumption is made that extraction increased significantly in 2011, then the instantaneous subsidence in year 5–6 shows an instantaneous subsidence value of 0.04 m/y corresponding to the subsiding area in Dagon Myothit.

Now that a hypothetical situation is established explaining the observed subsidence, the corresponding groundwater extraction can be calculated. This is done by only considering the lateral flow in the confined middle layer of the soil profile and neglecting vertical flow through the clay layers. Confined horizontal flow can be approximated using Darcy's law:

$$q_{sx} = -K \cdot H \cdot \frac{\partial h}{\partial x} \quad (6.2)$$

with  $q_{s,x}$  the specific horizontal discharge in  $\text{m}^2/\text{d}$ ,  $K$  as the hydraulic conductivity of the soil in  $\text{m}/\text{d}$ ,  $H$  the aquifer thickness, and the head gradient  $\partial h/\partial x$ . Substitution of soil parameters  $K = 20$ ,  $H = 10$ , the reduction in water stress  $\partial h = -10$  and a radial distance of  $\partial x = 1e4$ , resulting in a gradient of  $\partial h/\partial x = -1e-3$ , results in a specific discharge of  $q_{s,x} = 0.2 \text{ m}^2/\text{d}$ . As this situation concerns radial flow, the gradient is not constant, but increasing exponentially in magnitude towards the centre of extraction. In order to convert the specific discharge to the actual discharge, the radial distance at which the gradient holds is estimated to be half of the distance on which the gradient is based, being 5000 m. Then the discharge can be obtained by multiplication of the specific discharge with the circumference of this radial distance obtaining  $Q = q_{s,x} \cdot x_r^2 \cdot \pi = 1.57 \times 10^7 \text{ m}^3/\text{d}$ . When normalizing by the extraction area having the same area, a normalized extraction of 0.2 m/d is obtained. In comparison to the actual extraction estimation, this differs two orders of magnitude. Although there are high uncertainties in this assessment, it does show that actual extraction amounts could be higher through for instance industrial usage which might also reach into deeper aquifers. Furthermore, it shows that the measured surface deformation could be explained by multiple source contributors.

Table 6.1: Assumed soil parameters for the subsidence model. The layers consist of alternating sand and clay each containing their own properties. The soil layers have an assumed saturated specific density and for the clay layers, the top layer is assumed a little more dense than the lower one as it is likely to be consolidated more than the bottom one. Furthermore, the Clay layers each have a coefficient of secondary settlement,  $C_s$ , which is neglected for the sand layers. Conversely, the sand layers have a conductivity,  $K$ , which is absent in the clay layers.

	Type	top m	bottom m	$\gamma$ $\text{kNm}^{-3}$	$C_s$	$K$ m/d
<b>Layer 1</b>	Sand	0	-5	20	-	20
<b>Layer 2</b>	Clay	-5	-10	15	160	-
<b>Layer 3</b>	Sand	-10	-20	20	-	20
<b>Layer 4</b>	Clay	-20	-22	14	160	-
<b>Layer 5</b>	Sand	-22	-37	20	-	20

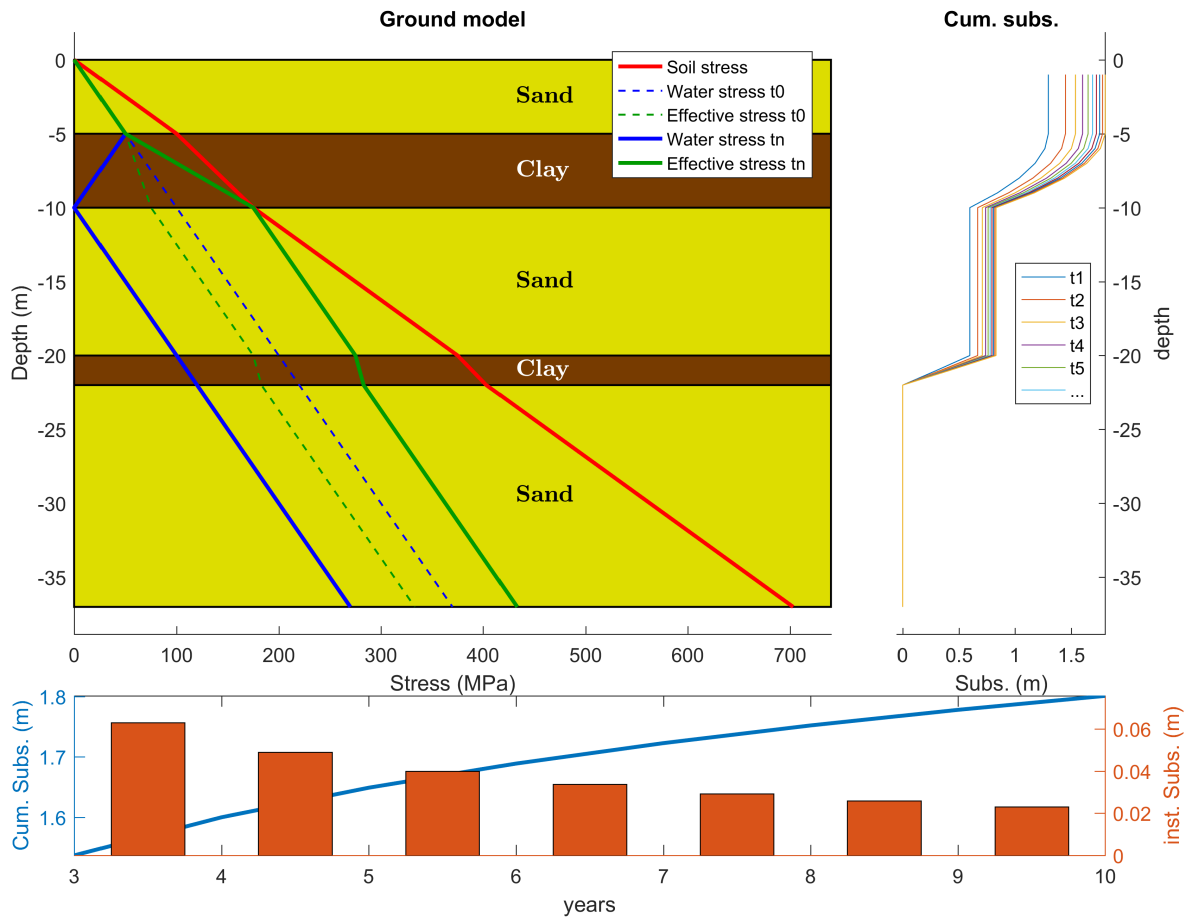


Fig. 6.10: Subsidence model due to groundwater extraction. The top left shows the soil model with the alternating sand and clay layers whose properties are listed in Table 6.1. The assumed soil and water stresses for the original situation and the extraction situation are plotted over the soil depth. The top right graph shows the calculated settlement over depth according to equation (6.1) from  $t_0$  to  $t_n$  with  $n=10$  years. The bottom graph shows the cumulative subsidence on the left axis and the instantaneous subsidence on the right axis.

## Conclusions and recommendations

This chapter will give short answers to all the individual research question and will then formulate an answer to the main research question. Finally some recommendations for direction of future research will be given together with possible strategies of mitigating negative effects of subsidence. In this research, we set out to answer the main research question:

*Can InSAR be used for measuring subsidence in Yangon and is there a correlation between subsidence and groundwater extraction?*

by answering the subquestions:

1. *Can InSAR be applied for the area of Yangon?*
2. *Is it possible to extract surface deformation from the interferometric output?*
3. *Where are significant amounts of water extracted from the ground?*

As an answer to the first sub-question, this thesis demonstrates that SAR interferometry can be applied in the city of Yangon throughout the year. The temporal stability over the urbanized extent in the city ensures that coherent interferograms can be made, even over time-spans longer than 250 days. Agricultural or sparsely urbanized areas prove to be less suitable for coherent results during the monsoon season lasting from mid-May until the end of November, but in the dry season these areas are stable enough to overcome the temporal decorrelation as long as the master image is also chosen in the dry season. To facilitate InSAR processing, the Single Look Complex images derived from data acquired by the Sentinel-1 (S1) satellite were used with the beta version of Doris v5. S1 provides ascending and descending data stacks with short temporal baselines, relatively small perpendicular baselines, and only few acquisition gaps for year-round recording. Over the course of this research, every 24 days an image was released over Yangon which will increase to once every 12 days when S1B will become fully operational. The InSAR processor Doris is capable of processing S1 images in the new release, although improvements in Enhanced Spectral Diversity in less coherent interferograms are required for the fine co-registration up to one millipixel necessary to process S1 datasets.

The answer to the second sub-question can be summarized as follows: The PSI time-series processing facilitates the extraction of surface deformation from the subtracted reference interferograms. The PS processor StaMPS enables the extraction of LOS velocities from a stack of interferograms without a-priori knowledge of the deformation behaviour in time. There are, however, assumptions made regarding the spatial behaviour of the deformation, forcing the algorithm output to be smooth and thereby hindering the detection of unwrapping errors. The fact that both ascending and descending stacks result in similar patterns, shows that the output is consistent. Vertical velocity differences up to 9 cm per year relative to the reference PS have been found in the east part of the city. Unfortunately, no validation of these values was done since no data regarding surface deformation in Yangon exists. The order of magnitude is more credible than the actual values since the number of images that have been used is under 25 and only little more than one year worth of data has been processed. The direction and magnitude of horizontal decomposed values depend heavily on the choice for reference PS and therefore no conclusions will be based on the horizontal velocity values. To summarize, it is indeed possible to extract the surface deformation from the interferometric output and the vertical velocity is considered to be correct concerning the order of magnitude.

To answer the third and final sub-question, significant amounts of water are extracted from the subsoil in several townships. The assessment on groundwater usage shows area-normalized extraction rates ranging from 0 to 8 mm/d on a township scale accounting for YCDC managed wells and private wells. The assessment on industrial water extraction could not be done because of a lack in data, and its significance also remains unknown. Nearly all available data is publicly not available on a finer scale than used in this research. There is also no available information on groundwater levels or soil layers to support the analysis on extraction. The results from the 'Water demand survey' provide a reasonable estimate for the daily usage of water by citizens of Yangon. The water demand survey also shows how the daily water demand is mainly dependent on how water is delivered to (or obtained by) the users rather than depending on income. Concerning the groundwater extraction, the most significant extractions were found in the old central part of town where the extraction estimate is dominated by YCDC wells. Towards the outskirts of the city, the normalized extraction amounts are slightly lower, although they consist mainly of private well extraction.

To answer the main question using the answers on the previous question, the results in this thesis show that it is indeed possible to extract surface deformation in Yangon using InSAR by subsequent processing with a PSI time-series analysis. Subsidence velocity differences up to 9 cm/y were found between the reference point and the severest subsiding area found in the Dagon Myothit townships. However, the subsidence signal does not correlate with the groundwater extraction on a township scale. This does mean that a first order indicator for a causal relation between the two parameters cannot be found, but it does not confirm or deny that there is a possible more complex relation between the two. Determining the actual sources of surface deformation requires a more extensive approach also incorporating industrial water usage.

Future research should mainly be directed towards the sources of surface deformation. In order to form the correct strategy for further research, the principle mechanisms of the surface deformation should be identified first. Discussed in sections 6.3 and 6.6 are some suggestions such as reduction in recharge, settlement of buildings and erosion of soil that are worth considering. The assessment on the subsidence mechanisms would be much more conceivable by the support of information on water level time-series and soil layer characteristics in the subsiding areas. Regarding the groundwater assessment, improvements can be made regarding the estimate on extraction of wells managed by the city council, especially when more detailed information on extraction amounts is available rather than capacities. This assessment would also greatly benefit from information regarding industrial extraction wells. Improvements on the InSAR and PSI can be made by using 25 or, preferably, more images ideally with a range covering two years or more. Additionally, the option of using the multi-temporal approach can be considered for an even more extensive analysis, but development of these algorithms for S1 is still required.

Considering the approach for managing water resources, it would be wise to act on the possibility of the surface deformation being caused by groundwater extraction. Though many attempts are made to significantly reduce the amount of water extracted from the subsoil, it will still take several years and maybe even decades to get every citizen connected to other means of water supply. To whom it may concern, take into account that many of the subsidence effects are, in fact, non-reversible and although they are not always immediately apparent, the damages resulting from them can be enormous. Also take into account other negative effects as depletion of groundwater resources, deterioration of aquifer conductivity and aquifer salinization to stress the importance of immediate action, and when considering if measures need to be applied. Possible means of mitigation of subsidence effects other than reducing of water use include: artificial recharge (or infiltration) and an optimization of pumping locations and discharge according to ground-water flow models.

# References

- Aobpaet, A., Trisirisatayawong, I., Aung, H. H., Maksin, P., Technology, S., Agency, D., Committee, M. E. & Insar, P. S. (2014), Yangon surface displacement as detected by InSAR time series, *in* 'Asian Association on Remote Sensing', pp. 1–6.
- Bally, P. (2012), Scientific and Technical Memorandum of The International Forum on Satellite EO and Geo-hazards, 21-23 May 2012, Santorini Greece, *in* 'THE INTERNATIONAL FORUM ON SATELLITE EO AND GEOHAZARDS (draft)'.  
**URL:** <http://esamultimedia.esa.int/docs/EarthObservation/Geohazards/esa-geo-hz-rd-2012.pdf> Publication
- Chen, C. W. & Zebker, H. a. (2000), 'Network approaches to two-dimensional phase unwrapping: intractability and two new algorithms.', *Journal of the Optical Society of America. A, Optics, image science, and vision* **17**(3), 401–414.
- Chen, F., Lin, H., Zhang, Y. & Lu, Z. (2012), 'Ground subsidence geo-hazards induced by rapid urbanization: Implications from InSAR observation and geological analysis', *Natural Hazards and Earth System Science* **12**(4), 935–942.
- Cuenca, M. C. & Hanssen, R. (2008), 'Subsidence due to peat decomposition in the Netherlands, kinematic observations from radar interferometry', *European Space Agency, (Special Publication) ESA SP* (649 SP).
- de Moel, P., Verberk, J. & van Dijk, J. (2004), *Drinkwater - Principes En Praktijk*, Sdu Uitgevers, Den Haag.
- De Zan, F. & Guarnieri, A. M. (2006), 'TOPSAR: Terrain observation by progressive scans', *IEEE Transactions on Geoscience and Remote Sensing* **44**(9), 2352–2360.
- ESA (2016), 'Sentinel-1 - ESA EO Missions - Earth Online - ESA'.  
**URL:** <https://earth.esa.int/web/guest/missions/esa-operational-eo-missions/sentinel-1>
- Fernandez, J., Escobar, D., Bock, H. & Femenias, P. (2016), Copernicus POD service operations - orbital accuracy of Sentinel-1A and Sentinel-2A, *in* 'EGU General Assembly 2016', Vienna, p. 3855.
- Ferretti, A., Monti-guarnieri, A., Prati, C. & Rocca, F. (2007), InSAR Principles (part A): Guidelines for SAR Interferometry Processing and Interpretation (TM-19, February 2007), *in* 'InSAR Principles', ESA, p. 71.
- Ferretti, A., Prati, C. & Rocca, F. (2001), 'Permanent Scatters in SAR Interferometry', *IEEE Transactions on Geoscience and Remote Sensing* **39**(1), 8–20.
- Grandin, R. (2015), Interferometric processing of SLC Sentinel-1 TOPS data, *in* 'ESA Fringe 2015 Workshop', Vol. SP-731, ESA, pp. 1–14.
- Hanssen, R. F. (2001), *Radar Interferometry*, Vol. 2 of *Remote Sensing and Digital Image Processing*, Springer Netherlands, Dordrecht.  
**URL:** <http://link.springer.com/10.1007/0-306-47633-9>
- Higgins, S. A. (2015), 'Review: Advances in delta-subsidence research using satellite methods', *Hydrogeology Journal*.  
**URL:** <http://link.springer.com/10.1007/s10040-015-1330-6>
- Hlaing, K. Y. (2012), 'Understanding Recent Political Changes in Myanmar', *Contemporary Southeast Asia* **34**(2), 197–216.  
**URL:** <https://bookshop.iseas.edu.sg/publication/630>
- Hooper, A., Bekaert, D., Spaans, K. & Arikan, M. (2012), 'Recent advances in SAR interferometry time series analysis for measuring crustal deformation', *Tectonophysics* **514-517**, 1–13.

Hooper, A., Segall, P. & Zebker, H. (2007), 'Persistent scatterer interferometric synthetic aperture radar for crustal deformation analysis, with application to Volc??n Alcedo, Gal??pagos', *Journal of Geophysical Research: Solid Earth* **112**(7), 1–21.

Hooper, A. & Zebker, H. A. (2007), 'Phase unwrapping in three dimensions with application to InSAR time series.', *Journal of the Optical Society of America* **24**(9), 2737–2747.

IBNet (2016), 'Tariff Benchmarking Map - IBNet Tariffs Database'.

**URL:** <https://tariffs.ib-net.org/VisualSearch/TariffHeatMap>

ILHCA (2006), 'Integrated Household Living Conditions Survey in Myanmar', p. 107.

JICA (2014a), The project for the improvement of water supply, sewerage and drainage - Vol III: Water supply system master plan, Technical report, JICA.

JICA (2014b), The project for the improvement of water supply, sewerage and drainage - Vol VI: Sewerage and drainage system master plan, Technical report.

Kampes, B. M., Hanssen, R. F. & Zbigniew, P. (2003), 'Radar interferometry with public domain tools', *Third International Workshop on ERS SAR Interferometry, 'FRINGE03', Frascati, Italy, 1-5 Dec 2003* p. 6.

**URL:** <http://doris.tudelft.nl/>

Maljaars, J. (2015), Optimized Coregistration methods for Sentinel-1 TOPS data, PhD thesis, Delft University of Technology.

MIMU, UN & Embassy of Switzerland in Myanmar (2014), 'Population of Myanmar using the World Population Grid'.

**URL:** <http://www.worldpop.org.uk/>

Ministry of Agriculture and Irrigation (2013), 'Agricultural Atlas'.

Minn, H. H. (2014), 'No Water Supplies above 12th Floor: YCDC | Myanmar Business Today'.

**URL:** <http://www.mmbiztoday.com/articles/no-water-supplies-above-12th-floor-ycdc>

Mon, E. K., Htay, Y. Y., Tun, S. L. & Aung, Z. W. (2013), 'Yangon ' s Water Supply Treatment Issues'.

Morley, I. (2013), 'Rangoon', *Cities* **31**, 601–614.

Munian, A. (2010), *Dynamics of Residential Water Demand and Supply in India: A Case Study of Chennai City*, Gyan Publishing House, New Delhi.

NASA (2000), 'Sinking River Deltas - Irrawaddy River : Image of the Day'.

**URL:** <http://earthobservatory.nasa.gov/IOTD/view.php?id=40257>

Richmond, S. & Brody, C. (n.d.), 'History of Myanmar/Burma - Lonely Planet Travel Information'.

**URL:** <http://www.lonelyplanet.com/myanmar-burma/history>

Ruby, E. (2005), 'How Urbanization Affects the Water Cycle', *CA WALUP Partnership website* pp. 1–4.

**URL:** [https://www.google.co.uk/?gws\\_rd=cr&ei=qIUdU4iVDoKqhAfK14CgCQ#q=pouplation+and+increasing+urbanization+eff](https://www.google.co.uk/?gws_rd=cr&ei=qIUdU4iVDoKqhAfK14CgCQ#q=pouplation+and+increasing+urbanization+eff)

RVO Netherlands (2014), 'Myanmar Integrated Water Resources Management, Strategic Study'.

Sakar, N. (2014), Development of Advanced Co-registration Methods for Sentinel-1 TOPS Mode Master ' s Thesis, PhD thesis, Technische Universität München.

Schubert, A., Small, D., Meier, E., Miranda, N. & Geudtner, D. (2014), 'Spaceborne SAR product geolocation accuracy: A Sentinel-1 update', *International Geoscience and Remote Sensing Symposium (IGARSS)* **3**(1), 2675–2678.

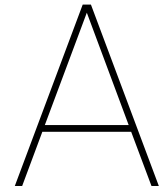
Syvitski, J. P. M. (2008), 'Deltas at risk', *Sustainability Science* **3**(1), 23–32.

Syvitski, J. P. M., Kettner, A. J., Overeem, I., Hutton, E. W. H., Hannon, M. T., Brakenridge, G. R., Day, J., Vörösmarty, C., Saito, Y., Giosan, L. & Nicholls, R. J. (2009), 'Sinking deltas due to human activities', *Nature Geoscience* **2**(10), 681–686.

**URL:** <http://www.nature.com/doi/finder/10.1038/ngeo629>

- TU Delft (2008), 'Delft object-oriented radar interferometric software: Users manual and technical documentation', *Delft University of Technology, Delft*.  
**URL:** <http://scholar.google.com/scholar?hl=en&btnG=Search&q=intitle:Delft+Object-oriented+Radar+Interferometric+Software+User+?+s+manual+and+technical+documentation#1>
- USGS (2016), 'How much is your daily indoor water use?'.  
**URL:** <http://water.usgs.gov/edu/activity-percapita.html>
- van der Horst, T. (2016), 'Subsidence in Yangon , Myanmar A study of terrain deformation using InSAR'.
- Van Leijen, F. J. (2014), Persistent Scatterer Interferometry based on geodetic estimation theory, PhD thesis, Delft University of Technology.
- Verruijt, a. (2012), *Soil Mechanics*, Delft University of Technology.  
**URL:** <http://geo.verruijt.net/>
- Wang, F, Miao, L. & Lu, W. (2013), 'Sand creep as a factor in land subsidence during groundwater level recovery in the southern Yangtze River delta, China', *Bulletin of Engineering Geology and the Environment* **72**(3-4), 273–283.
- WebTeckTix (2014), 'Soil Settlement Types, Calculations & Analysis - Settlement Limits'.  
**URL:** <http://www.aboutcivil.org/types-of-soil-settlement.html>
- WMO (2016), 'WMO OSCAR | Observing Systems Capability Analysis and Review Tool Analysis and Review Tool - Home'.  
**URL:** <http://www.wmo-sat.info/oscar/>
- Wyne Khin, P. P. (2016), 'Yangon water supplies to outlast hot season, says YCDC'.  
**URL:** <http://www.mmmtimes.com/index.php/national-news/yangon/19376-yangon-water-supplies-to-outlast-hot-season-says-ycdc.html>
- YCDC (2014), 'Water Supply , Sewerage System and The Improvement Projects for Yangon City'.
- YCDC (2015), Situation of Water Supply System of Yangon City and it ' s Future Demand, Technical report, YCDC.
- YCDC & JICA (2013), The Strategic Urban Development Plan of the Greater Yangon Yangon 2040, Technical Report March, YCDC.





## Short recent history of Myanmar

The following story is based on (Richmond & Brody, n.d.; Hlaing, 2012) and useful for those who would like to know more about how present Myanmar came to be.

From the early 19<sup>th</sup> century to WWII the British Empire ruled Burma (previous name of Myanmar) until the Japanese drove them away together with the Burmese Independence Army declaring 'Myanmar' an independent country. Towards the end of the war the Burmese switched sides and fought to drive out the Japanese.

After the war Bogyoke Aung San, an early activist for nationalism and later minister of defence, held the country together after the Japanese were driven out. After winning the democratic elections in 1947, Aung San was assassinated by a rival after which the country struggled as political candidates were assassinated and ethnic conflicts raged.

In 1962 General Ne Win led a left-wing army takeover and set the country heading towards Socialism, crippling the country economically. In 1988 the Burmese people started a massive confrontation and set the army aside demanding for democratic elections. The quickly formed State Law and Order Restoration Council (SLORC) declared martial law and arranged for democratic elections in which they were opposed by National League for Democracy (NLD) led by the daughter of Bogyoke Aung San, Aung San Suu Kyi. During this time the official name of the country was changed from the 'Union of Burma' to the 'Union of Myanmar' since 'Burma' was still associated with European colonialism.

Again an attempt for a democratic election was destroyed as SLORC refused the NLD to assume their righteous acquired positions in parliament. It would take another 20 years before a new constitution would pass and fair elections would take place in which the chosen candidate could actually assume it's governing position.

Although after 2011 many internal power shifts in the government have taken place in order to provide a positive political change and fight corruption, it should not be expected that Myanmar will become fully democratic any time soon. The expansion of the political openness should proceed carefully in order for the liberals and pro-democracy movement to work together without prompting the armed forces again to preform a coup.



# B

## Maps of Yangon and Myanmar

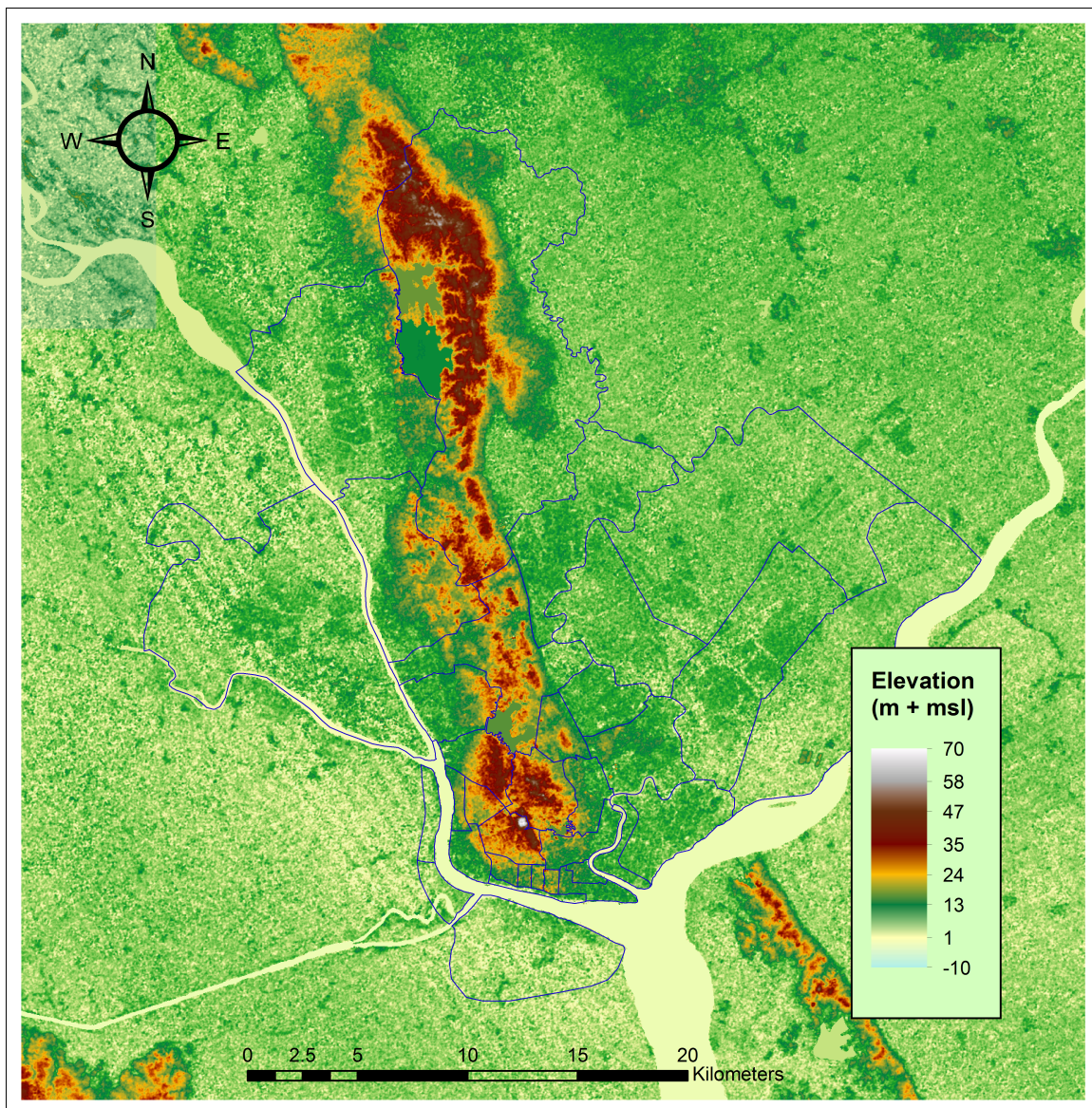


Fig. B.1: The DEM of Yangon provided by United States Geological Survey (USGS).

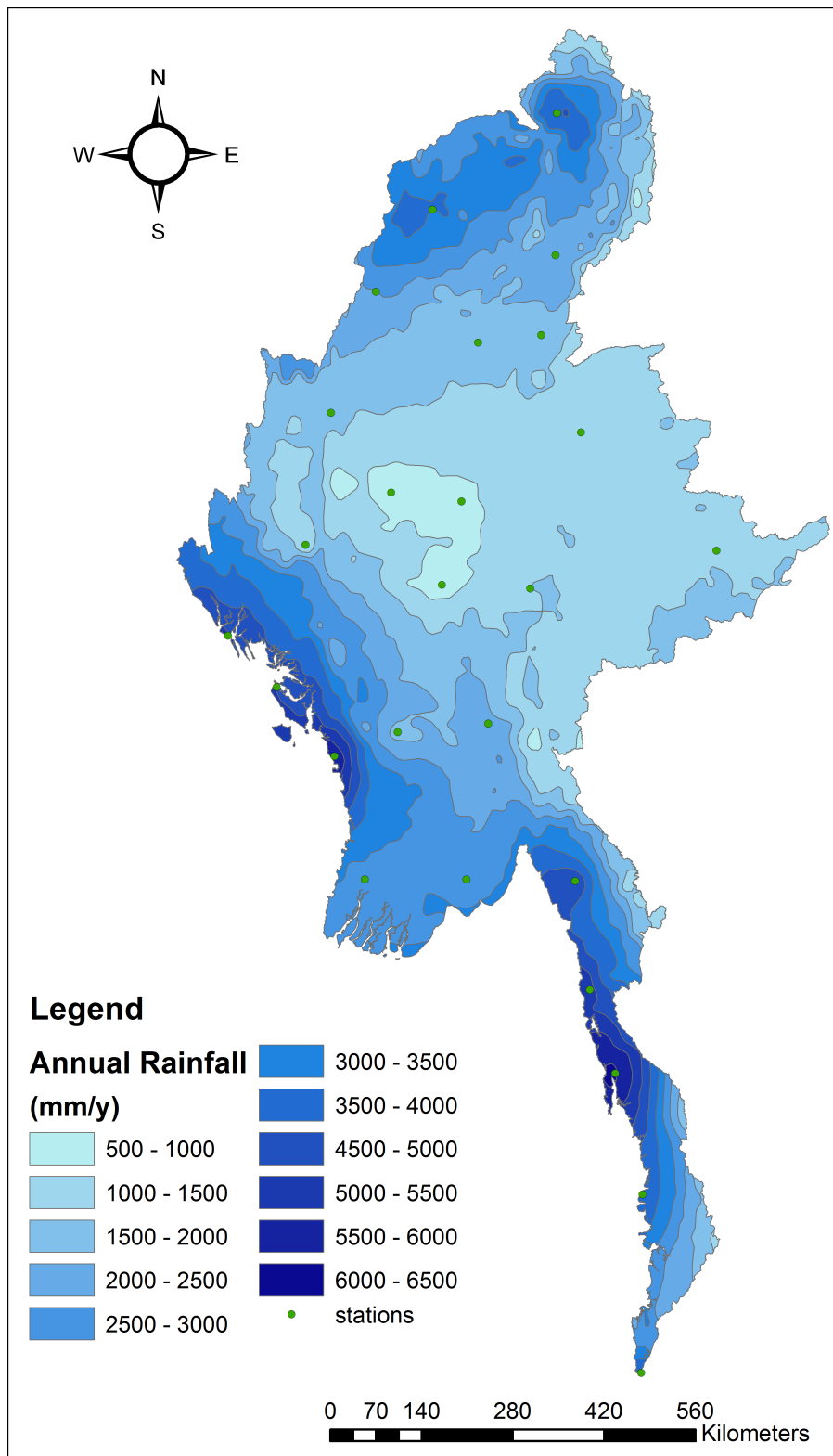


Fig. B.2: Contour plot of long-term averaged annual rainfall for Myanmar. The green dots represent rainfall gauges.

# C

## Pre study on subsidence in Yangon

This appendix consists of an unpublished pre-study done for this thesis in which a part of the same ascending data stack was processed. This data was cascaded to assess the quality of S1 interferograms throughout the year. It states a few requirements which have been used as guidelines for the processing of the single-master stack. The reference corresponding to this appendix is (van der Horst, 2016).

# Subsidence in Yangon, Myanmar

## A study of terrain deformation using InSAR

Teije van der Horst, *Student, Delft University of Technology,*

**Abstract**—Yangon, Myanmar is one of the cities in South-East Asia where subsidence due to groundwater extraction is one among potential natural hazard. Like in many neighbouring countries, the majority of inhabitants in this urbanized delta region rely on groundwater supply with very few alternatives for receiving water from other sources. Little is known on the true extent to which subsidence is currently occurring in Yangon, therefore this research uses state-of-the-art techniques to evaluate the current situation regarding surface deformation. Data from ESA's Sentinel-1 is processed using the newest version of doris for differential-InSAR. Fourteen cascaded interferograms have been formed, clearly showing the effects of seasonality and temporal decorrelation. Although subsidence is hard to detect using only a d-InSAR approach, future research steered towards advanced post-processing techniques may present the desired outcome.

**Index Terms**—InSAR, Yangon, Sentinel-1, TOPSAR, Subsidence.

### 1 INTRODUCTION

THIS is the final assignment for the course CIE4609 - Geodesy and Natural Hazards. This report will elaborate on most topics learned in the course which are applied to a case study: Yangon, the former capital of Myanmar also known as Rangoon and Burma respectively.

#### 1.1 Sinking deltas

All around the world major river deltas are sinking relative to local mean sea level. On the one hand this is caused by (local) mean sea level rise in the order of few millimeters per year. On the other hand the ground surface in delta regions is susceptible for subsidence as a result of both natural and human induced causes [1]. Natural causes for land subsidence include sediment compaction, peat oxidation, crustal motion [2] which are often found to be in the same order of magnitude as sea level rise [1].

Human induced land subsidence is mainly caused by excessive groundwater extraction as a result of rapid urbanization and/or hydrocarbon extraction. Among the problems that can arise as a result of land subsidence are an increased vulnerability to flooding and storm surges, (infra)structural failures, aquifer salinization, and permanent geological deformation [3] [4].

The Irrawaddy Delta is an example of such a delta system in peril where sea level rise and (accelerated) soil compaction may form a large threat for the people living in it. The storm surge area covers as much as 15 000 km<sup>2</sup> exposing over 5 million people in the city of Yangon alone.

#### 1.2 Yangon area and its water usage

Yangon Region is the highest populated region of the country housing around 720 inh/km<sup>2</sup>. Currently 50% of the region is for agricultural use and 30% is urbanized area, but these numbers are expected to shift more towards urbanisation as the city is still expanding in northern direction [5].

Little is known about the true usage of drinking water throughout the city. Somewhere between 40% [5] - 60% [6] of the city's inhabitants are connected to reservoirs through a pipe system managed by the Yangon City Development Committee (YCDC). Other means of getting water are ponds in the town, rainwater harvesting and tube wells. Of the water supplied by the city council 10% is groundwater use and of the personal supply as much as 80% [6]. In total between 35 to 50% of Yangon's inhabitants receive water from the subsoil.

Drawdown of the groundwater table is related to subsidence; the increased stress on the soil skeleton results in elastic and inelastic strain [7]; compressible soil layers will consolidate [8] and; peat layers may oxidize [9]. The majority of these processes is non-reversible.

#### 1.3 Previous study

One preceding study is known to have assessed subsidence in Yangon by means of Interferometric Synthetic Aperture Radar (InSAR) [10]. A Persistent Scatter Interferometry (PSI) analysis is done using 15 descending orbit Radar satellite 2 (Rsat-2) images. The research suggests non-seismic surface deformation with vertical displacement rate differences up to 12 cm/y, most likely caused by groundwater extraction. The used images have been acquired between April 2012 and April 2014, nearly all of them during the dry season. Validation of these results proved to be impossible due to the unavailability of data. The research states that the numbers should be interpreted carefully and emphasizes that primarily the potential of InSAR for this kind of analysis is shown. Furthermore it should be noted that there was no description of the vertical displacement reference assumption.

#### 1.4 Research objective

The aim of this research is to answer the following questions: **Can subsidence in Yangon be detected using InSAR?** and **Are parts of Yangon currently subsiding?**

## 2 DATA

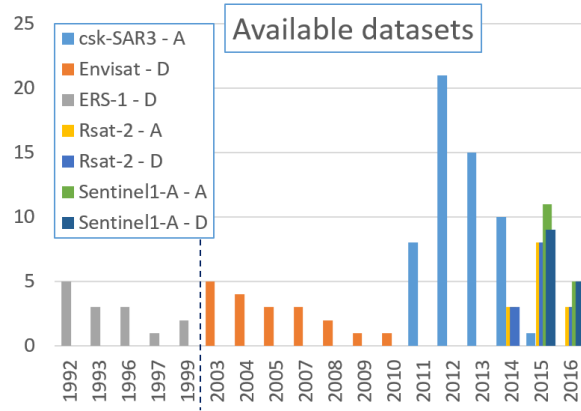


Fig. 1. Available data stacks for csk, Envisat, ERS-1, Rsat-2 S1a; Amount of images per satellite per year split into ascending and descending orbits. Between 1999 and 2003 no data is available. Source: SkyGeo

AVAILABILITY of data is assessed using the SkyGeo image catalog to see which InSAR data stacks are available for COSMO-SkyMed (csk), Environmental Satellite (Envisat), European remote sensing satellite 1 (ERS-1), Radar satellite 2 (Rsat-2) and S1a. A distinction is made between ascending and descending orbits as they have to be processed separately. The available datasets are shown in Fig. 1 demonstrating poor coverage for satellites before 2011 with five or less acquisitions on a yearly basis.

### 2.1 Selection of data

Considering the available data from all satellites, both ERS-1 and Envisat can be discarded because they lie outside the temporal domain of interest; The socio-economic changes in Myanmar's recent history [11], makes for possible variations in water demand to be significant from 2011 onwards. When considering all remaining satellites, it is clear that only csk does not have ascending and descending orbits. Furthermore this data is not freely accessible and the author does not have the means to obtain this dataset easily. Both Rsat-2 and S1a have the advantage of collecting ascending and descending orbits<sup>1</sup> while still gathering their datasets at the moment of writing. The factors that contribute to the choice of Sentinel-1 data over Rsat-2 can be summarized as follows:

- Rsat-2 data is only available in the dry season – from December to April – and it should be interesting to see the full potential of InSAR throughout the year
- The development of Delft object-oriented radar interferometric software (doris) software can now run simultaneously with testing on an actual case.
- Sentinel recently launched the second satellite increasing its revisit time by a factor two when it starts collecting data.

1. For this assignment only ascending orbits are considered, but descending orbits will be used in the author's master thesis

### 2.2 About the collected data

The S1a images are collected from the European Space Agency (ESA) scientific data hub using a predefined polygon from the launch date until May 2016. The resulting stack of data over the area of interest is visible in Fig. 2. The ascending orbit stack is chosen because the area of interest fits into the bounds of a single image per orbit.

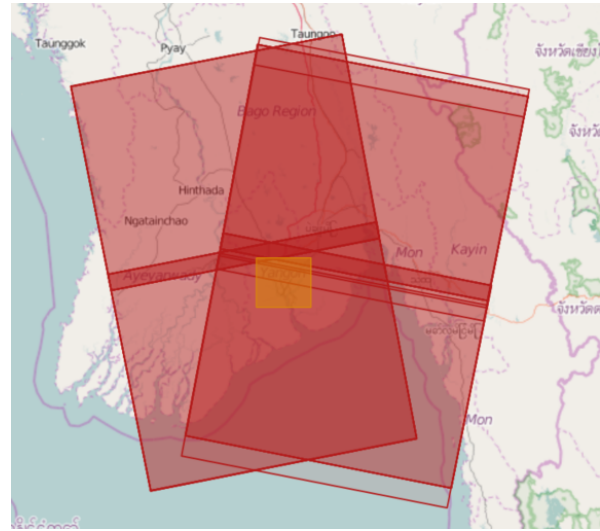


Fig. 2. Sentinel-1 data stacks over area of interest. Source: ESA SciHub

The data was collected as level-1 Single Look Complex (SLC)<sup>2</sup> data with a  $5 \times 20$  m ground geometry as provided by ESA's scientific data hub. All data was collected in the Interferometric Wide Swath (IW) with a single 'VV' polarization. The dates range from May 31, 2015 until May 25, 2016 in which a total of 14 images were used.

### 2.3 Perpendicular Base-line

Fig. 3 shows the perpendicular baselines for different orbits with Dec 29, 2015 as a reference. Sentinel-1 baselines are very small as the satellite is steered quite accurately into the same track. Each image pair that can be made has a baseline far below the critical baseline.

Considering the height ambiguity, the sensitivity for errors made by Digital Elevation Model (DEM) phase subtraction of the final interferogram is less for small values of  $B_{\perp}$  since the interferometric-phase is related to the perpendicular baseline according to:

$$\partial\phi = -\frac{4\pi}{\lambda} \left( \frac{B_{\perp}}{R \sin\theta} H_p \right) \quad (1)$$

where  $\phi$  is the interferometric phase,  $\lambda$  is the wavelength,  $B_{\perp}$  is the perpendicular baseline,  $R$  is the slant-range,  $\theta$  is the look angle and  $H_p$  is the topographic height.

2. Compressed data in complex format with the largest possible resolution

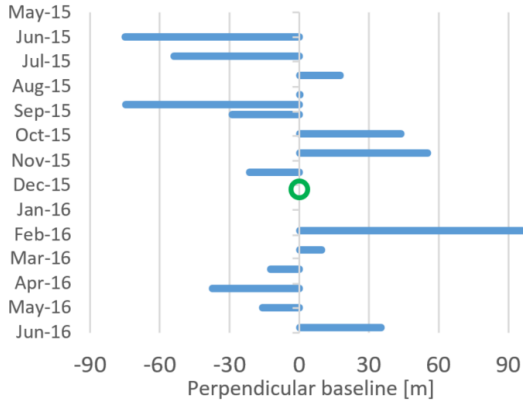


Fig. 3. Perpendicular baselines of all usable ascending orbit images. The zero baseline is defined at the reference image on December 9, 2015. (data generated using SNAP)

### 3 METHODOLOGY

THE selected images are processed on a Linux cluster at Delft University of Technology (TU Delft) using doris. Fourteen images are used to make thirteen interferograms by cascading<sup>3</sup> through the images each with the master and slave being 24 days apart. These interferograms are used for a differential InSAR (d-InSAR) analysis.

#### 3.1 Elevation model

A DEM is necessary for co-registration and phase subtraction when performing a deformation analysis such as d-InSAR. The creation of a DEM is difficult using Sentinel-1 data as no tandem missions exist making the temporal baseline too high to avoid decorrelation while the perpendicular baseline is often too small. Therefore a DEM is extracted from Shuttle Radar Topography Mission 3'' (SRTM3).

#### 3.2 Differential interferometry

$$\phi_{int} = \phi_{flat} + \phi_{topo} + \phi_{defo} + \phi_{atmo} + \phi_{noise} \quad (2)$$

Each interferogram consists of multiple phase contributors that determine the interferometric phase  $\phi_{int}$  according to (2) with the earth's near flat approximated ellipsoid shape phase  $\phi_{flat}$ , the topographic phase contribution  $\phi_{topo}$ , the phase by surface deformation between acquisitions  $\phi_{defo}$ , the atmospheric phase contribution  $\phi_{atmo}$  also known as Atmospheric Phase Screen (APS) and the noise contributions  $\phi_{noise}$  [12]. After subtraction of the calculated phase values for both  $\phi_{flat}$  and  $\phi_{topo}$  the remaining interferometric phase consists of surface deformation, APS and noise and error sources.

#### 3.3 Pair-wise logic

Assuming that the error sources can be disregarded, the objective is now to distinguish between deformation and atmospheric contribution. This can be done using pair-wise logic between all consecutive images as follows;

3. The first in time of each pair is used as master image and the second in time is used as a slave image.

Atmosphere in one image is seen in two consecutive interferograms in which the image functions as a master in the first and a slave in the second. This ensures that the APS is positive in one interferogram where it is negative in the second, whereas linear deformation phenomena retain the same direction.

## 4 SENTINEL-1 PROCESSING STRUCTURE

SENTINEL-1 IW data is processed different than stripmap acquisitions; a few extra steps are introduced. The images are processed using the beta version of doris 5.0 [13] developed by the TU Delft. This version supports the processing of Sentinel-1 IW mode also known as TOPS covering 250 km in range direction.

### 4.1 TOPS

Sentinel-1 has a few modes of collecting data that affect the resolution and swath width that is collected each track. The one used in this research is the Interferometric Wide Swath mode which uses Terrain Observation by Progressive Scans (TOPS) in three range sub-swaths by steering the antenna in range and azimuth direction as illustrated in Fig. 4. Hereby the coverage in range direction is increased at the cost of azimuth resolution as the steering in azimuth direction, necessary to avoid scalloping, shrinks the footprint [14] [15]. The sub-swaths are split into multiple bursts with marginal overlap where each burst has been processed as a separate SLC image.

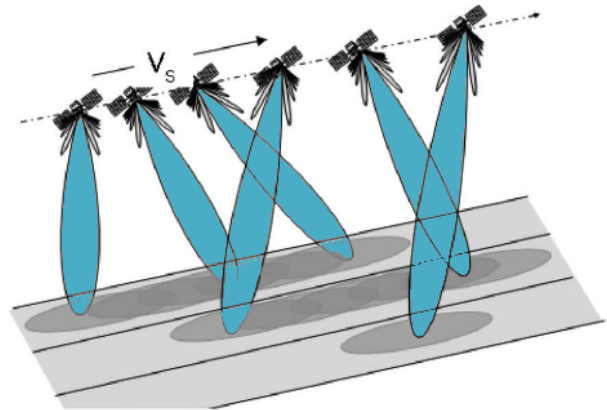


Fig. 4. TOPS acquisition mode, the three sub-swath scanning scheme by steering in both azimuth and range direction in a repeated cycle. The steering of the antenna introduces a variation of the Doppler centroid frequency [14].

### 4.2 Processing setup

The steps required for the processing of InSAR datasets using doris are shown in Fig. 5 where additional steps required for TOPS are highlighted green. Some additional information on Sentinel processing is given below as it differs from the regular stripmap processing steps.

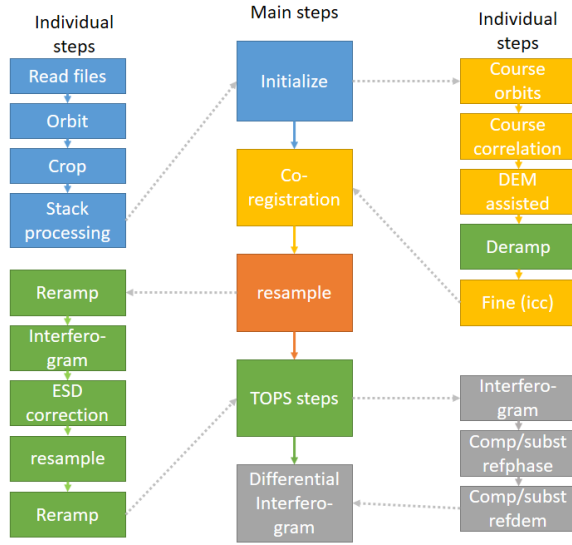


Fig. 5. Processing scheme for Sentinel-1 TOPS mode. The additional steps for Sentinel-1 are highlighted in green

#### 4.2.1 Initialize

The SLC images are read and split into bursts; Complete bursts covering the area of interest are extracted without cropping while the ones outside the domain of interest are rejected completely.

#### 4.2.2 Co-registration

At the coarse correlation step, the master and slave image offsets are calculated on magnitude images in the space domain rather than the spectral domain since it performs much better in low-coherent areas.

An extra step is introduced in the processing of TOPS data; a quadratic phase ramp is introduced because of the steering in azimuth direction of the radar beam during acquisition. Grandin has provided a method to remove this quadratic phase called 'deramping' [16].

#### 4.2.3 Resampling

One additional resampling step is introduced for the creation of the first interferogram necessary for the TOPS processing steps. The first resampling after the fine cross correlation step ensures a co-registration accuracy up to sub-pixel level as prerequisite for a successful Enhanced Spectral Diversity (ESD) correction [17].

#### 4.2.4 TOPS steps

The precise alignment of the master and slave images has to be accurate to within  $1/1000^{th}$  of a pixel. This precise co-registration is necessary because the difference in squint angle to the ground targets during acquisition introduce a large Doppler centroid variation. A mis-registration leads to a phase jump at the burst boundaries. The accuracy is obtained by exploiting the spectral difference at the overlapping edges of the bursts. The interferometric phase difference between these overlaps can be related to the mis-

registration in azimuth direction [15]. Once the exact co-registration parameters are determined, the original deramped product is resampled and reramped again to the desired accuracy. This final co-registration step is called ESD

#### 4.2.5 Differential Interferogram

These steps does not differ much from regular differential interferogram formation.

$$I = M \cdot S^* \cdot R^* \quad (3)$$

For each burst the interferometric phase is calculated according to the complex interferogram minus the reference phase formula eq. (3) [18] in which  $I$  denotes the complex interferogram,  $M$  and  $S$  are the, deramped complex, master and slave images, and  $R$  represents the calculated reference phase with an amplitude of 1. The '\*' designates the conjugate of the complex dataset. A continuous interferogram is created by mosaicking the bursts together. The reference and topographic phases are calculated and subtracted, leaving the differential interferogram.

## 5 RESULTS

THE unwrapped interferograms from the cascaded dataset are shown in Fig. 6. The images are arranged by date ranging from 2015-05-31 to 2016-05-25. Also seen in this figure in the lower right corner is an interferogram with a 71 day temporal baseline during the dry season. The images display colour fringes ranging from blue through cyan, green and yellow to red each representing an interferometric phase value in the interval  $[-\pi, \pi)$ . For the approximate values of each colour, consult the legend in the bottom of Fig. 6.

All master images are first in time, thus an increase in slant-range distance between  $t_{master}$  and  $t_{slave}$  causes a decrease in phase in the slave image with respect to the master image as range and phase are related according to:

$$D = -\frac{\lambda}{4\pi} \phi \quad (4)$$

with line-of-sight deformation  $D$ . This ensures that the interferometric phase increases with increasing slant-range distance as the interferometric phase is the subtraction of the slave image from the master image.

The colours are also mixed with grayscale values which indicate the amplitude of the interferogram, dark meaning lower amplitude than light. The interferometric amplitude is the product of the master and slave amplitudes.

## 6 INTERPRETATION AND DISCUSSION

GENERALLY, the interferograms show the complete outline of the city to be coherent throughout the whole year, apart from several golf courses and surface waters such as reservoirs and rivers. However, the areas outside the city are much less coherent throughout the year because there is an absence of stable scatterers in the agricultural fields outside the city. These areas become visible in the dry months of the year from December until May. From December through January it seems that rural areas are still affected by temporal decorrelation while there is an almost absence of precipitation [19].

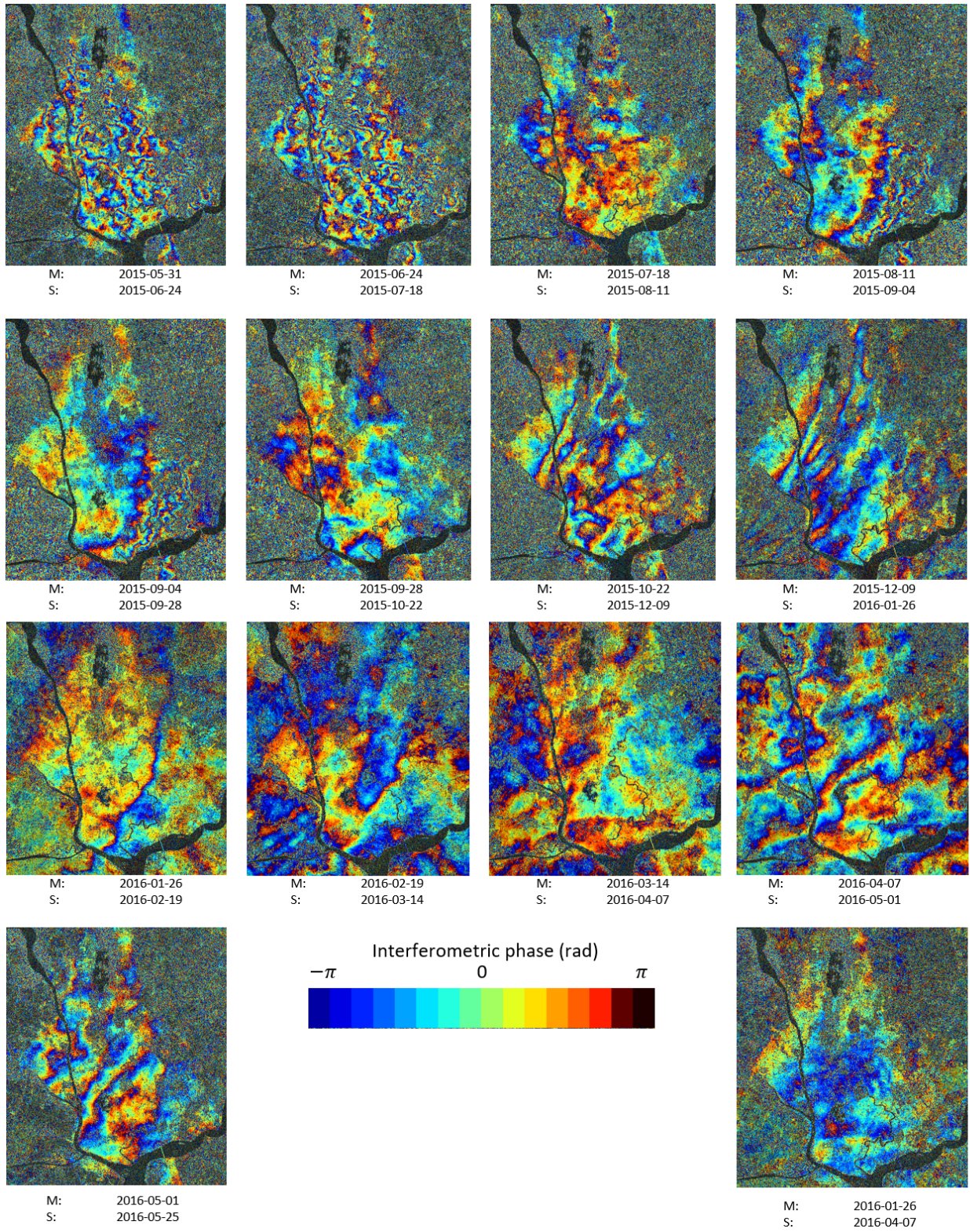


Fig. 6. 13 cascaded wrapped interferograms and an additional 3 month temporal baseline interferogram, displayed as interferometric phase mixed with magnitude.

### 6.1 Perpendicular and temporal baselines

The perpendicular baselines are all rather small with values ranging from 10 to 100 m. This ensures that the geometric decorrelation is kept to an absolute minimum. Another benefit of these small baselines is the reduced sensitivity to elevation and errors in the DEM. Although the elevation differences in and around Yangon amount to only 25 m, the DEM tends to be quite inaccurate at rural locations with maximum elevation errors up to 5 m based on visual inspection of the data. With eq (1) the error in phase as a result of this DEM error becomes 0.23 rad.

As one observes the results from the cascaded dataset, there are two dates missing in the 24 day baseline configuration. *Nov 15, 2015* and *Jan 02, 2016* have not been processed since the former resulted in processing errors and the latter was not recorded due to satellite unavailability. The effect of temporal decorrelation in the interferograms over the missing dates is not much greater than elsewhere, although the 48 days between Dec 09, 2015 and Jan 26, 2016 could also explain why the rural parts are still not coherent.

When comparing the 72 day interval from the bottom right in Fig. 6 to the other interferograms, the coherent area is reduced to only the extent of the city while both master and slave images had been acquired in the dry season. Note that while the perpendicular baseline for this case (131.8 m) is also larger than with any of the other interferograms, it is still relatively small. It seems that temporal decorrelation is dominant over spatial decorrelation.

### 6.2 Deformation and atmosphere

The interferometric phases are the combination of surface deformation, atmospheric contribution, orbital ramps and noise. Atmosphere appears to be dominant in all interferograms although its influence and scale vary over the year. Based on these results, a few fringes within several kilometres are found in the monsoon season and roughly one fringe over the whole city outside the monsoon season. Since this cascade only consists of one dry season, there is not enough data to confirm a trend.

It is nearly impossible to find locations where the effect of surface deformation is present using only a visual interpretation. Even the 72 day baseline interferogram does not allow for a clear interpretation of the interferometric phase. Unwrapping might make phase interpretation easier, but in general a more sophisticated approach is desired for estimating surface deformation where the interferograms are sampled on the same grid.

While estimation of surface deformation remains difficult, it is possible to estimate an upper bound of deformation based on these images. When observing the dry season interferograms which are expected to have the most deformation present, there is roughly one fringe of phase difference observed in a 24 day interval. When assuming that a stronger deformation signal than one fringe would have been detected, the upper bound for deformation can be set at 42 cm/y. When considering the 72 day interval interferogram in the dry season, one fringe is observed which translates into an upper bound of only 14 cm/y.

## 7 CONCLUSIONS AND RECOMMENDATIONS

SENTINEL-1 is a relatively new satellite with notable benefits for studies on surface deformation. It records the entire year though on nearly every location in the world with a swath of 250 km. In the case of Yangon, SLC images can be found both ascending and descending from *May 2015* onwards. Further benefits include small perpendicular baselines and short temporal baselines.

Doris is an excellent tool for processing of Sentinel data and works particularly well with small temporal baselines. The most critical processing step was the high-precision co-registration for which small errors result in high inaccuracies.

A cascade of interferograms demonstrates how Yangon remains coherent throughout the whole year while coherence in the remaining parts of the delta appear only in the dry season lasting from mid December through April. The monsoon has a notable effect on the scale and intensity of signal delay in the lower atmosphere. Even though this effect has significantly diminished in the dry season, it is still greater than surface displacements.

This article exhibits that surface deformation in Yangon cannot be observed directly using a cascaded Sentinel-1 datastack. Therefore the second question cannot yet be answered. However, an upper limit of 14 cm/y of relative displacement is found through the 72 day interval interferogram. Further research on this topic should focus on time series analysis with either a PS-InSAR, a Small-Baseline or a hybrid approach. If a single master is chosen, it would be well to choose the master date in the dry season and such that it minimizes temporal decorrelation over geometric decorrelation as the latter is generally much smaller for Sentinel-1.

### ACKNOWLEDGMENT

The interferometric processing was performed using the freely available Doris software package developed by the Delft University of Technology. Many thanks to Gert Mulder who helped me during the processing of Sentinel data using the unpublished version of doris which I've seen improving on a daily basis. I am also grateful to Ramon Hansen for the help in interpreting results and to Freek van Leijen who was kind enough to supply the DEM in a doris friendly format.

The results in this article relied heavily on the data provided by ESA which have been provided free of charge which is frankly amazing. Furthermore the image catalog tool from SkyGeo is used to assess available datasets for the area of interest and the author would like to thank SkyGeo for providing access to this tool.

## REFERENCES

- [1] J. P. M. Syvitski, "Deltas at risk," *Sustainability Science*, vol. 3, no. 1, pp. 23–32, 2008.
- [2] S. A. Higgins, "Review: Advances in delta-subidence research using satellite methods," *Hydrogeology Journal*, 2015. [Online]. Available: <http://link.springer.com/10.1007/s10040-015-1330-6>
- [3] J. P. M. Syvitski, A. J. Kettner, I. Overeem, E. W. H. Hutton, M. T. Hannon, G. R. Brakenridge, J. Day, C. Vörösmarty, Y. Saito, L. Giosan, and R. J. Nicholls, "Sinking deltas due to human activities," *Nature Geoscience*, vol. 2, no. 10, pp. 681–686, 2009. [Online]. Available: <http://www.nature.com/doi/10.1038/ngeo629>
- [4] F. Wang, L. Miao, and W. Lu, "Sand creep as a factor in land subsidence during groundwater level recovery in the southern Yangtze River delta, China," *Bulletin of Engineering Geology and the Environment*, vol. 72, no. 3-4, pp. 273–283, 2013.
- [5] YCDC and JICA, "The Strategic Urban Development Plan of the Greater Yangon Yangon 2040," YCDC, Tech. Rep. March, 2013.
- [6] YCDC, "Water Supply, Sewerage System and The Improvement Projects for Yangon City," 2014.
- [7] USGS, "Land Subsidence Measurement Techniques — USGS California Water Science Center," 2016. [Online]. Available: <http://ca.water.usgs.gov/land/subsidence/california-subsidence-measuring.html>
- [8] a. Verruijt, *Soil Mechanics*. Delft University of Technology, 2012. [Online]. Available: <http://geo.verruijt.net/>
- [9] M. Cuenca, R. Hanssen, and F. van Leijen, "Subsidence due to peat decomposition in the Netherlands," *Environmental Modelling & Software*, vol. 20, no. 2, pp. 215–229, 2005. [Online]. Available: <http://www.sciencedirect.com/science/article/pii/S1364815204000398>
- [10] A. Aobpaet, I. Trisirisatayawong, H. H. Aung, P. Maksin, S. Technology, D. Agency, M. E. Committee, and P. S. Insar, "Yangon surface displacement as detected by InSAR time series," in *Asian Association on Remote Sensing*, 2014, pp. 1–6.
- [11] I. Morley, "Rangoon," *Cities*, vol. 31, pp. 601–614, 2013.
- [12] J. Maljaars, "Optimized Coregistration methods for Sentinel-1 TOPS data," Ph.D. dissertation, Delft University of Technology, 2015.
- [13] B. M. Kampes, R. F. Hanssen, and P. Zbigniew, "Radar interferometry with public domain tools," *Third International Workshop on ERS SAR Interferometry, 'FRINGE03', Frascati, Italy, 1-5 Dec 2003*, p. 6, 2003. [Online]. Available: <http://doris.tudelft.nl/>
- [14] F. De Zan and A. M. Guarnieri, "TOPSAR: Terrain observation by progressive scans," *IEEE Transactions on Geoscience and Remote Sensing*, vol. 44, no. 9, pp. 2352–2360, 2006.
- [15] N. Sakar, "Development of Advanced Co-registration Methods for Sentinel-1 TOPS Mode Master 's Thesis," Ph.D. dissertation, Technische Universität München, 2014.
- [16] R. Grandin, "Interferometric processing of SLC Sentinel-1 TOPS data," in *ESA Fringe 2015 Workshop*, vol. SP-731. ESA, 2015, pp. 1–14.
- [17] N. Yague-martinez, F. R. Gonzalez, R. Brcic, R. Chau, F. D. Zan, and G. Gomba, "Interferometric Processing of Sentinel-1A TOPS data," *IEEE Transactions on Geoscience and Remote Sensing*, vol. 54, no. 4, pp. 2–5, 2015.
- [18] B. Kampes, "Delft object-oriented radar interferometric software: Users manual and technical documentation," *Delft University of Technology, Delft*, 1999. [Online]. Available: [#1](http://scholar.google.com/scholar?hl=en&btnG=Search&q=intitle:Delft+Object-oriented+Radar+Interferometric+Software+User+s+manual+and+technical+documentation)
- [19] ClimaTemps, "Yangon Climate," 2015. [Online]. Available: <http://www.yangon.climatemps.com/>

# D

## Additional PSI results

The wrapped, unwrapped phases are presented as they are important for interpretation of the quality of the results rather than being suitable for direct interpretation. The DEM error (Fig. 5.6) and the master Atmosphere and Orbit Error (AOE) are subtracted from both the wrapped and unwrapped phase for better visualization. For the unwrapped phase, the reference has been set to the first interferogram so that each value is zero and all increasing interferometric phases relate to phase-delay. The wrapped and unwrapped results for the ascending track can be found in Fig. D.2 and Fig. D.2. For the descending track both can be found at Fig. D.4 and Fig. D.5.

The spatially correlated master AOE which is present in all interferograms is also estimated in the PSI. Although the effect from it does not influence the LOS velocity results since it causes a constant offset in all phase values throughout all time-series, it is useful to subtract it from the wrapped and unwrapped phases so only the slave errors influence the results. The master AOE for both track is shown in Fig. D.1 where it can be seen that the ascending track is heavily affected and the descending track much less.

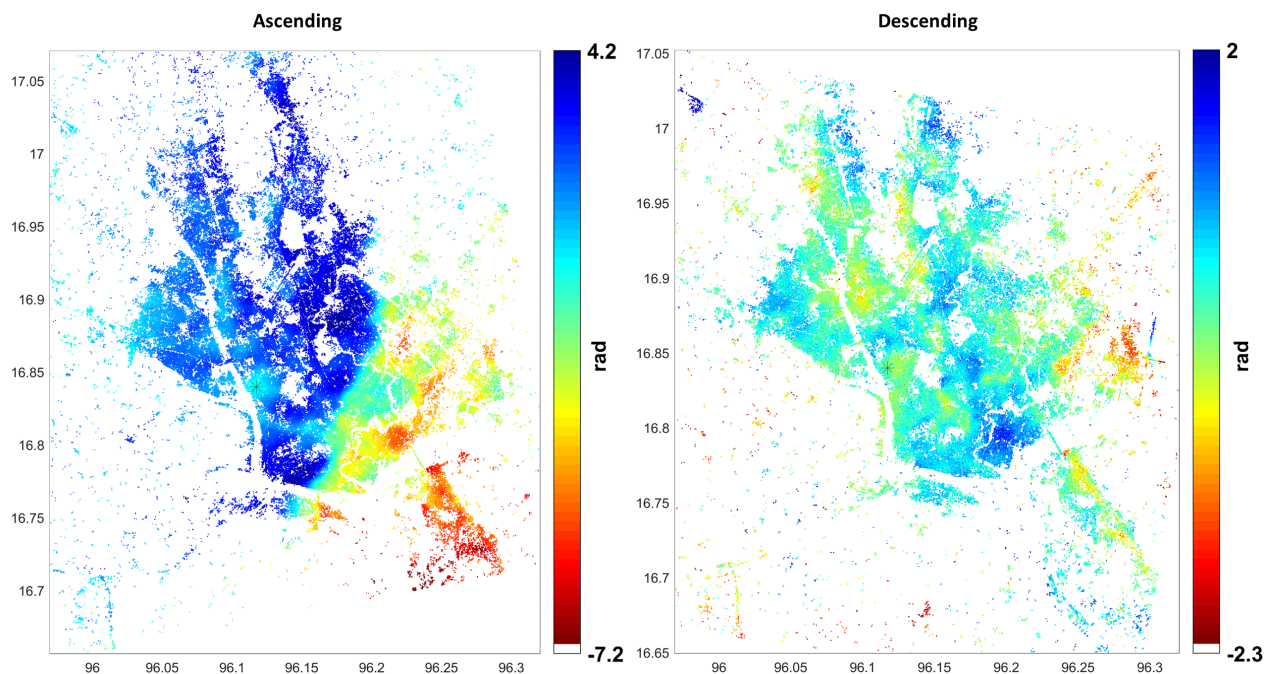


Fig. D.1: Estimate of the master Atmosphere and Orbit Error which is present in all interferograms. The estimate is made based on a spatially correlated constant offset found in each of the interferograms which is expected to be largely contributed by atmosphere. Orbital errors are expected to be much less significant (especially for S1) and are not clearly represented in these figures. Although not presented in this thesis, both tracks have a good correspondence with the small temporal baseline interferograms which include the master image.

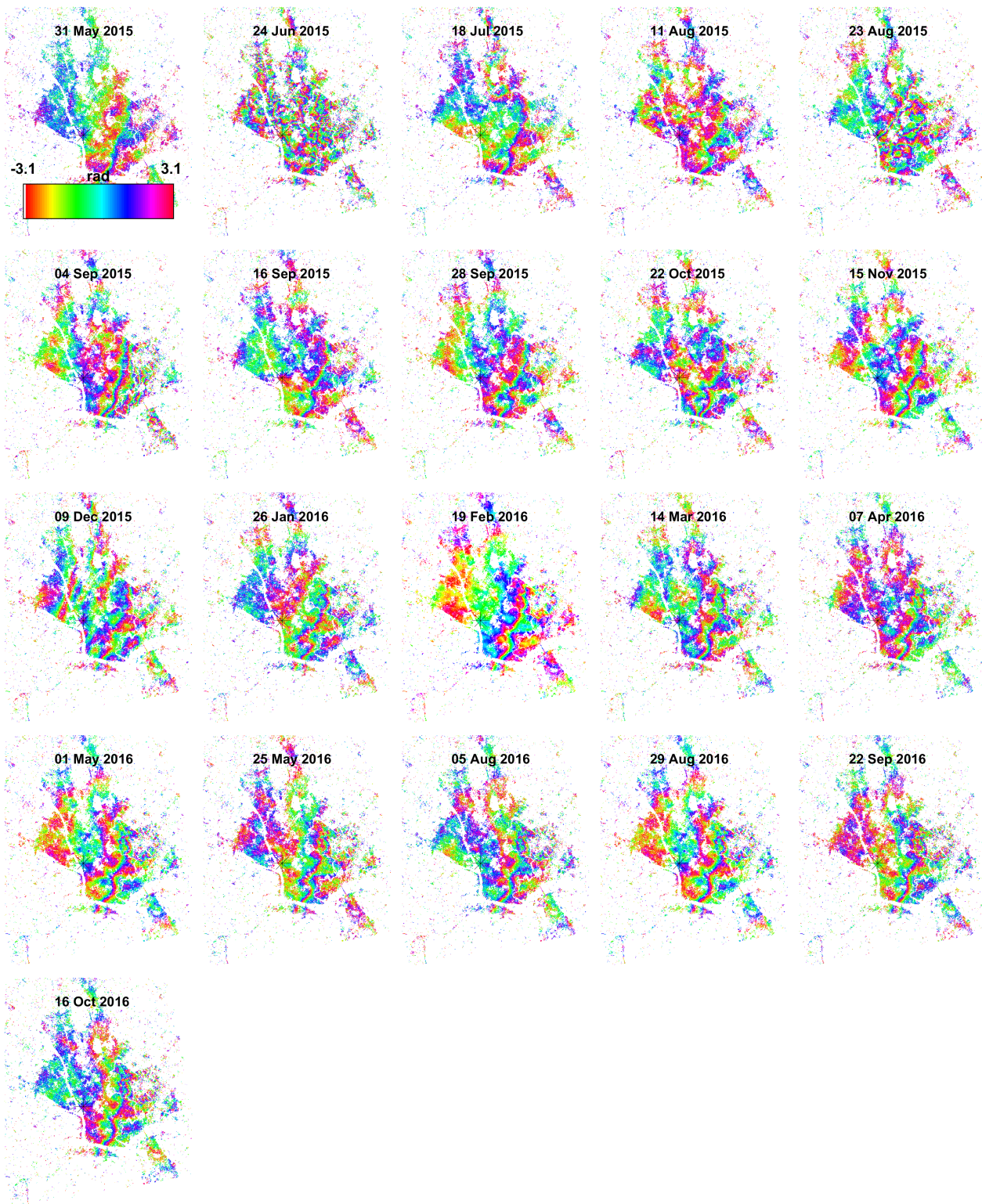


Fig. D.2: Phase values of the ascending track PS points in the wrapped domain  $[-\pi, +\pi)$ . No spatial filtering is applied and the values thus solely depend on the raw data from the differential interferograms minus the master AOE and DEM error. From these visuals, only clear atmospheric signals are visible and no clear subsiding areas can be identified.

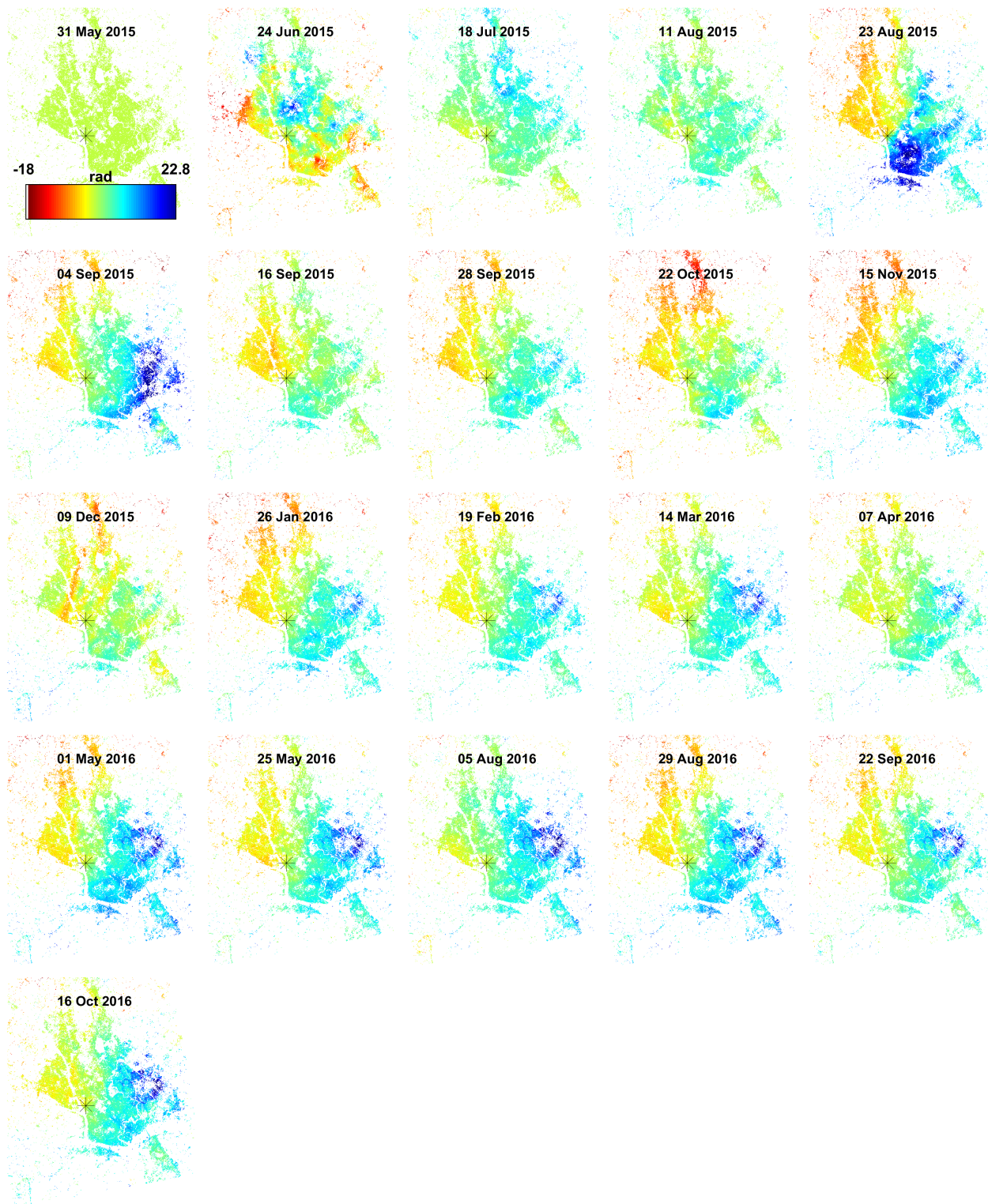


Fig. D.3: Unwrapped phase values for PS points of the ascending track. The spatially-filtered wrapped phase with subtracted master AOE and SCLA was the input for the unwrapping process in which assumptions regarding the surface deformation were used to obtain the unwrapped results. The first image was set as a reference for easier interpretation rather than the master. The results close to the reference consist of mainly atmosphere while the last image consists of mainly deformation both as implied from the temporal separation. Although large atmospheric influence is present in interferogram 2, 5 and 6, only 2 has been rejected because it interfered with the reference PS and the dropping of 5 and 6 did not lead to significant changes in surface deformation velocities.

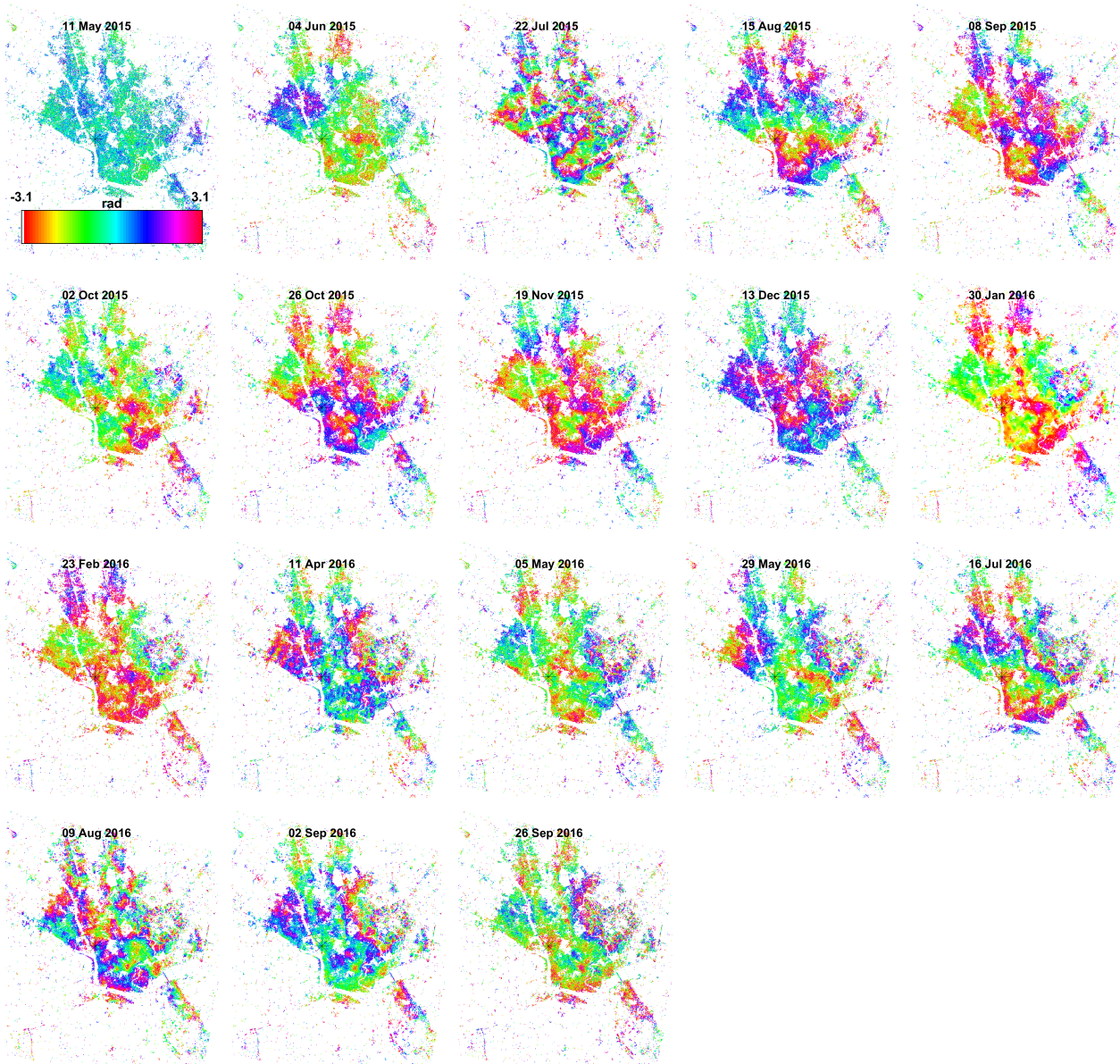


Fig. D.4: Phase values of the descending track PS points in the wrapped domain  $[-\pi, +\pi]$ . No spatial filtering is applied and the values thus solely depend on the raw data from the differential interferograms minus the master AOE and DEM error. From these visuals, only clear atmospheric signals are visible and no clear subsiding areas can be identified.

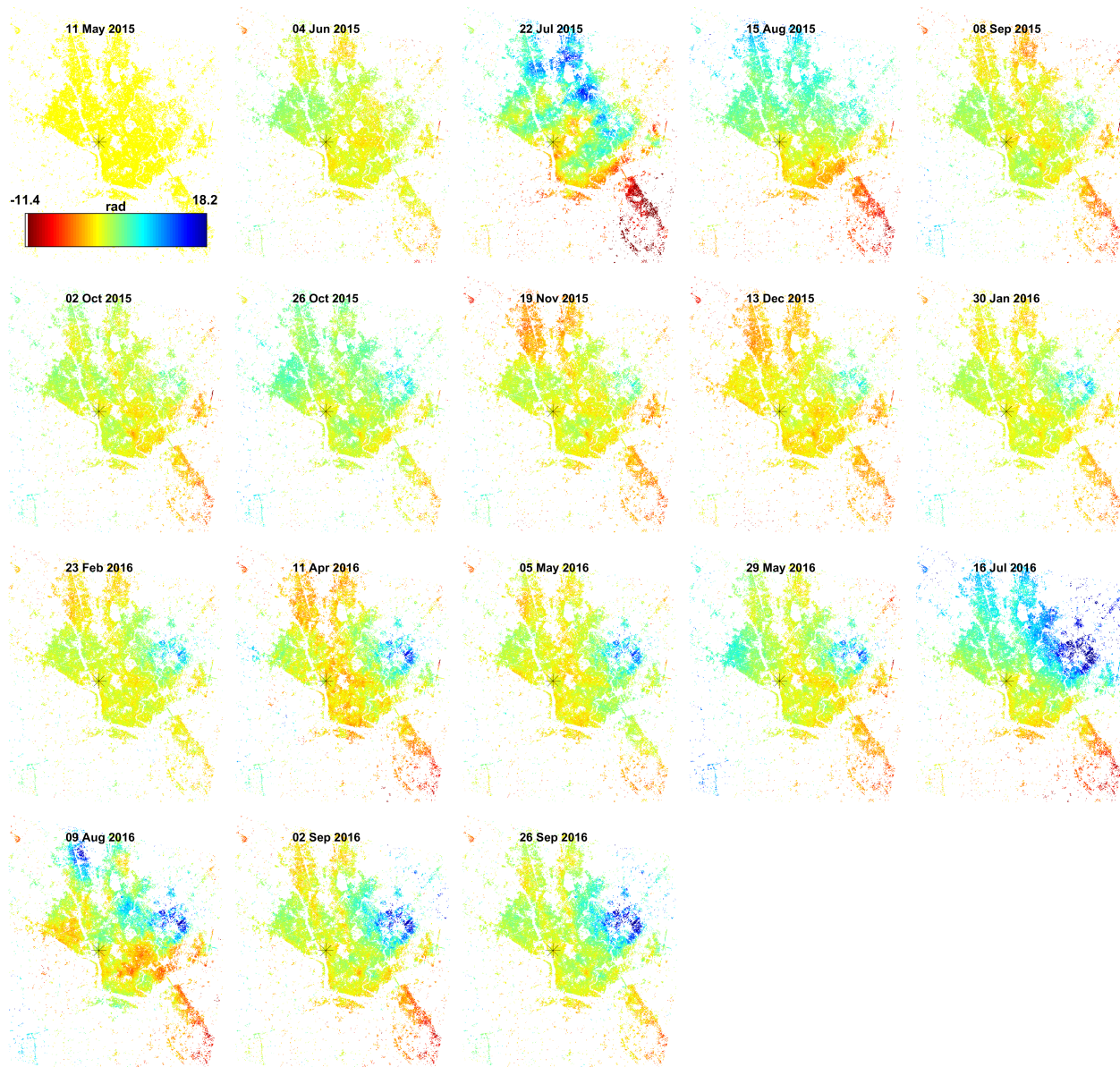


Fig. D.5: Unwrapped phase values for PS points of the descending track. The spatially-filtered wrapped phase with subtracted master AOE and SCLA was the input for the unwrapping process in which assumptions regarding the surface deformation were used to obtain the unwrapped results. The first image was set as a reference for easier interpretation rather than the master. The results close to the reference consist of mainly atmosphere while the last image consists of mainly deformation both as implied from the temporal separation. None of the interferograms were rejected during the PSI analysis.



# E

## Additional decomposition results

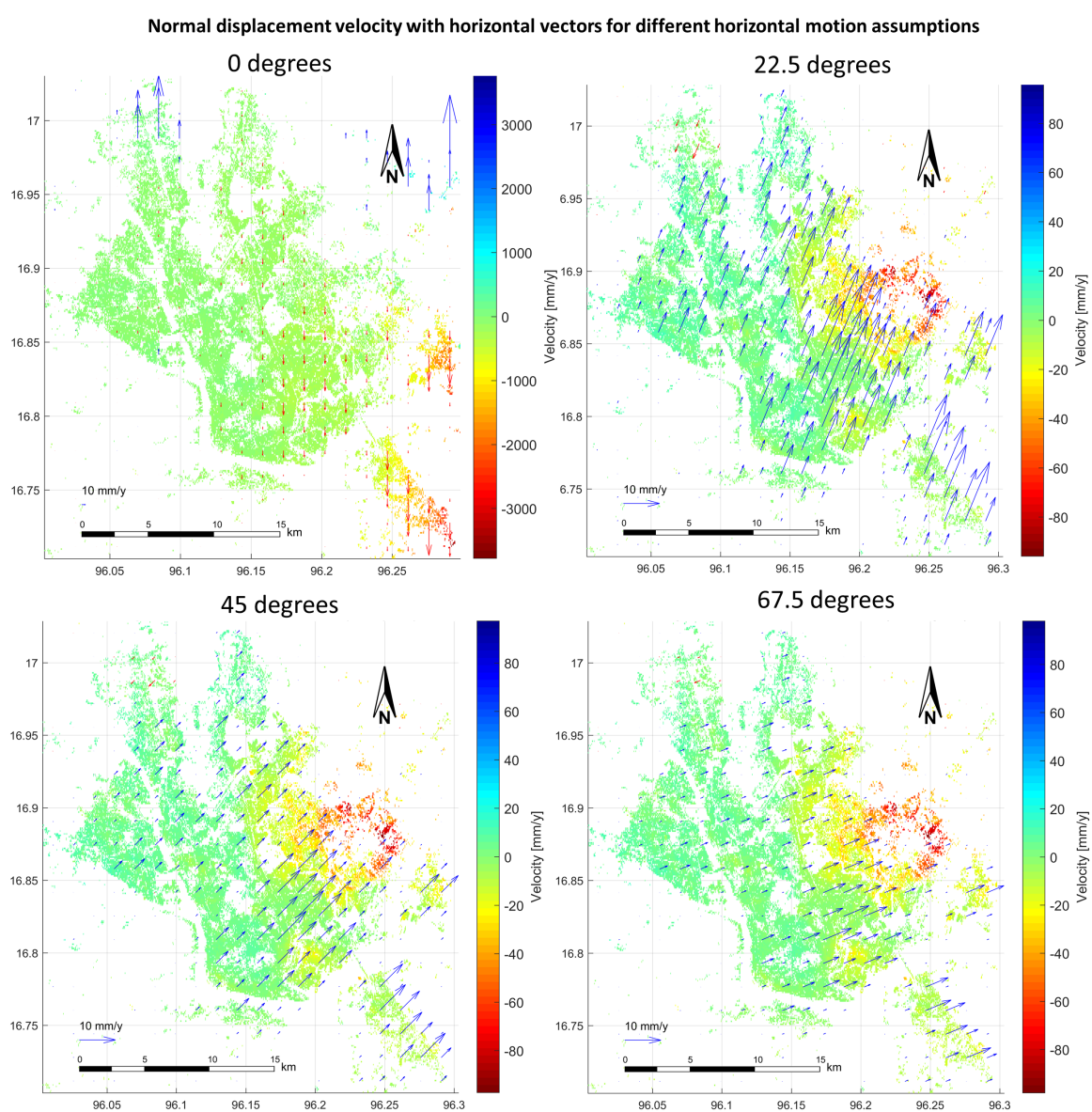


Fig. E.1: Decomposition results for different assumed horizontal deformation directions.

Additional decomposed results are shown in Fig. E.2 and Fig. E.1 where different assumptions regarding horizontal velocity direction are made. Only values between  $0^\circ$  and  $179^\circ$  are considered, as the  $+180^\circ$  directions would lead to the same results. The normal velocity is not affected by the assumed directions between  $45^\circ$  and  $135^\circ$  with respect to the North direction. The assumed directions close to North result in unrealistic behaviour which is the effect of the ALD not being sensitive for the North direction.

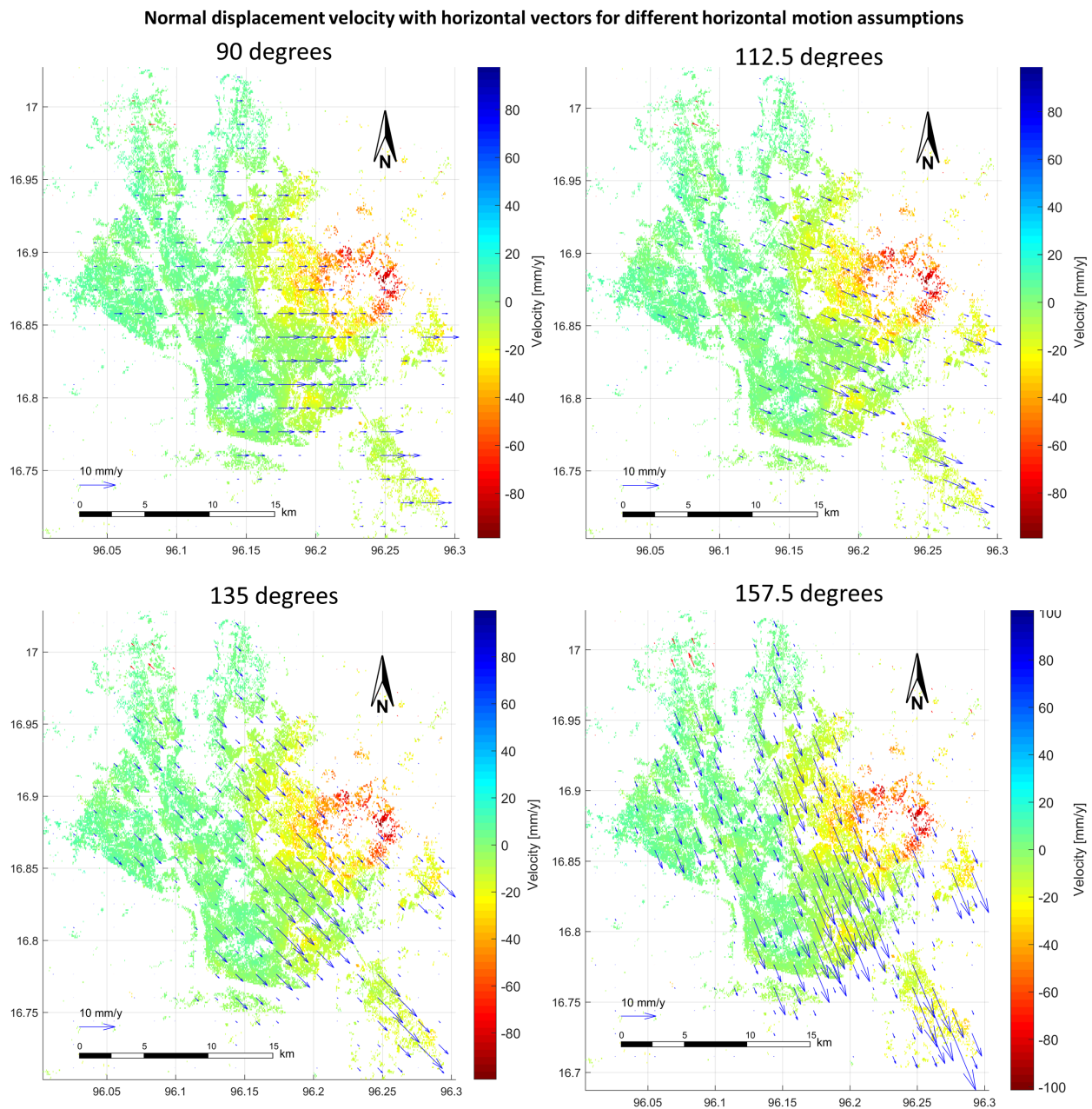
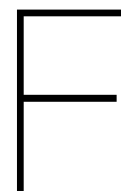


Fig. E.2: Decomposition results for different assumed horizontal deformation directions.



# Water Demand Survey

This is the report on the results of the water demand survey held in June and July 2016. The survey was held to assess the water demand for people living in Yangon, Myanmar. Aside from the assessment on the daily water demand, some additional questions were asked about its quality and how it is received. First the questionnaire set-up and the questions are discussed, then results are shown individually after which a short discussion is done in which other sources than this survey are included as well. The people who completed the survey will be called users from now on.

Throughout this appendix, the usage of Liters and Gallons is sometimes interchanged. Note that Imperial gallons are used which are converted as follows:

Table F.1: Liter/Gallon conversion

1 Gallon	=	4.546 Liter
1 Liter	=	0.220 Gallon

The questionnaire was partially preformed using the freely available Google forms and a discounted usage of AppSheet. The author would like to thank everyone who participated in this survey.

## Questionnaire set-up

The survey was non-supervised as questions were filled in digitally without the support of an interviewer. The questionnaire was set up in a way that most of the questions were asked in closed form aside from a few reflection questions. This was done to prevent interpretation bias but also to allow for quick completion of the questionnaire. Moreover, most of the questions needed facts or numbers rather than opinions or reflections. At the end of each section there was a reflection about the previous questions which was posed as open question. Some questions also allowed for the user to provide an additional answer if it was not listed in the answers that were pre-compiled.

The questionnaire could be completed on nearly all digital devices since it was available on both Google forms and an application created on AppSheet. The AppSheet application had the advantage of enabling the user to fill in the questions without the usage of internet. The questions could later be synchronized when internet was available again.

## Questions

The survey is divided into three parts; general information (1); Type of delivery based on (ILHCA, 2006) (2); and water demand based on (USGS, 2016; de Moel, Verberk & van Dijk, 2004) (3). All of the data was stripped from any personal information. Each section will be discussed separately. In each section, all questions are stated and then some elaboration will be given.

### General information

#### Listed questions:

- Gender:
- Age:
- Occupation:
- Township:
- Where in this township?
- GPS location (optional)

In the general information section, questions were asked about the gender, age, occupation and location. The gender (male /female) and age (open, number) are meant to assess if large differences between men, women or certain categories of age can be found. Furthermore some information is dependent on a geological reference. The location is only known approximately as the location was entered as Township from a drop-down menu with additionally a cardinal direction within this township. GPS coordinates could also be entered which would be precise up to 3 degree-decimals. This means that the location is known to a maximum accuracy of 100 m.

### Type of delivery

#### Listed questions:

- What is the main source of water supply to your house?
- How is the YCDC water supplied to your house?
- Do you have any other source(s) of water delivery?
- What kinds of private water supply do you have?
- If you extract water from the ground, is this registered at the YCDC?
- Where is the access point of this water source?
- How does the water availability vary over the day in the 'wet season'? A glass can be filled in:
- Does the answer to the previous question vary in the dry season?
- How does the water availability vary over the day in the 'dry season'? A glass can be filled in:
- Which color corresponds best to your water?
- Does the water taste saline (salty)?
- Do you boil the water before drinking?
- Do you have any remarks about this part of the survey?

This part of the survey was meant to see how water is delivered to users and what the quality of this water is. It was expected that users often have multiple sources to rely on in case their main source cannot supply enough water. A large survey was performed in Yangon before by ILHCA (2006), and most of the questions regarding the source of the water were based on information gathered in this document.

First of all there was a question where users receive their water from; The YCDC, private supply, unknown or an additional option. If the answer to the previous question was YCDC a question was asked if the user relied on another source of water. Furthermore the type of delivered water needed to be specified for YCDC and private sources. For YCDC the options were: Piped water with a private tap, piped water from a public tap, a source outside of the house such as a pond or a spring or an additional option. For private sources the options were: tube well, bore hole, dug hole, rainwater, river, lake or other as specified by user and multiple answers were possible. Moreover the location of the access point to the main source of water was asked where the access point could be: inside the house, inside the building, outside the building within 5 minutes walking and outside the building at more than 5 minutes walking.

For users possessing a tap, questions on this topic were covered. In order to do so, Fig. E.1 was shown with the question; How does the water availability vary over the day in the 'wet season'? The statement in the Figure states; "A glass can be filled in:" and the answer consisted of picking the numbers 1 to 4 corresponding to the

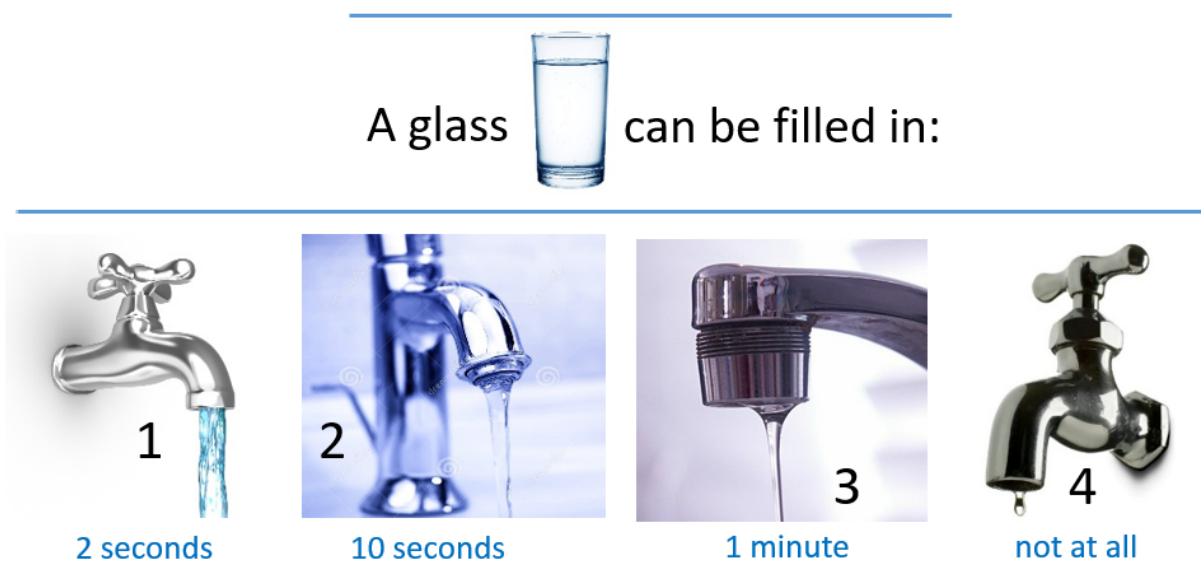


Fig. F.1: Selection of answer options for the water availability question; A glass can be filled in:

taps the figure. This was asked for each two hours of a regular day in the monsoon season and dry season.

To assess the water quality, three questions were asked making use of another visual interpretation. Which color corresponds best to your water? Where the options were to pick a number ranging from 1 - 5 as seen in Fig. F.2. The next question is slightly more open to personal interpretation; Does the water taste saline (salty)? Where the answer could be ranged from 1, not at all to 5 very much. Finally if users boil the water before drinking with answers ranging from 1, never to 4, always.



Fig. E.2: Answer options for the water turbidity; Turbidity value numbers 1 – 5

This section of the survey was concluded by a long-answer text where the used could fill in any remarks or additional information that was not covered by the type of delivery part of the survey.

## Water demand

### Listed questions:

- How many glasses of water do you drink per day?
- How many times per day do you brush your teeth?
- How many water do you use while brushing?
- How many times per day do you wash your hands or face?
- Do you have a bath at home?
- How many times per week do you shower?
- Which picture matches your shower best in terms of flow?
- How long does an average shower take?
- What kind of toilet do you have?
- How many flushes per day?
- How much water per flush?
- How much water do you use in food preparation?
- How many times per day are the dishes done? (whole house / day)
- How many times is washing done in your house? (whole house / week)
- How are your clothes washed?
- Please indicate other water demanding activities here (max 3):
- How many people live in your house?
- Do you think you use a lot of water in comparison to others in your house?
- Indicate why you think this:
- Do you have any further remarks about this part of the survey?

The final and most important part of the survey was meant to assess how much water a day is used on average. Although many of the questions are closed and aided with textual support, an additional visualization seen in Fig. E3 is added which should help to estimate quantities better for those who have a less understanding of water in a volumetric sense. For this part users were asked to think of a typical day when it is raining and they did not have to work or study and thus stay at home.

The first question was how water is used for drinking including any drinks made from the tap such as tea with answers 0 – 10 glasses or more. Hereafter the amount of water for brushing teeth was asked with two questions: How many times per day do you brush your teeth? With answers 0-3+ and how many water do you use while brushing with a selection of answers: None minimal (0.03 gal), about a glass (0.05 gal), about two glasses (0.1 gal), I leave the tap running for a short while (0.2 gal) and I leave the tap running (0.5 gal). Subsequently how many times per day do you wash your hands or face? Answers were ranging from 0 - 6+ with an assumption of 0.5 L each time.

For bathing the question was whether users owned a bath and how often it was used. Users could choose from every day, once a week, once per month or less or never. There are some large steps in between the answers as the assumption was that bathtubs would not be abundantly used. Hence also the quantity per bath is not examined. For the shower a more detailed analysis was done because of its large influence on the accuracy of the water demand. The questions consist of how many times do you shower, how long and what is the flow rate. To assess the flow rate, the users were asked to compare the showers in Fig. E4 and choose one or two that matched their flow best.

The next question regarded the toilet usage where the first question was to identify what kind of toilet was used. There were three options: squat toilet with reservoir, squat toilet without reservoir and flush toilet. There was also an option for the user to specify an answer to this question. To aid in identifying the correct toilet, the toilet types are visualized as seen in Fig. E5 The final question about toilet use is to estimate how much water is used each flush with the aid of textual support and the quantities as seen in Fig. E3.

The next section asked about dish washing for the whole house over a day which would be normalized with the amount of people living in one home. The same is done for a washing machine where the amount of washings for a whole household per week was asked. For both activities amounts have been assumed based on multiple sources and common sense. A distinction was made between hand washing and machine washing in terms of used water amount. Although a small amount, users were also asked to estimate how much water they use in food preparation.

Conversion table		
		
0.25 Liter 0.05 gallon	1 Liter 0.2 gallon	2 Liter 0.45 gallon
		
4.5 Liter 1 gallon	10.0 Liter 2.2 gallon	22.5 Liter 5 gallon

Fig. F3: Conversion table to support quantity estimations



Fig. F4: Showers with different flow rates for discharge estimation

Nearly all of the common water demanding activities have been covered at this point in the questionnaire. Therefore there was some space where additional activities could be placed such as watering the garden, cleaning the house or other activities. The user had to specify the activity, volume, unit and timespan with a maximum of three, and was again aided with Fig. F.3.

There were some remaining questions in the questionnaire that provide insight into the situation of the household of the user. The amount of people that live in the users house was asked and also if the user thinks that he or she uses more or less water than the rest in the house while indicating the reason for this thought.



Fig. F5: Different toilet types where the user could choose from

This section of the survey was concluded by a long-answer text where the user could fill in any remarks or additional information that was not covered by the type of delivery part of the survey.

## Results

The results of the questionnaire have been processed using the export function of google forms in which all results (both AppSheet and Google forms) are combined. The results in numbers and figures are shown in the same order as they were asked in the questionnaire.

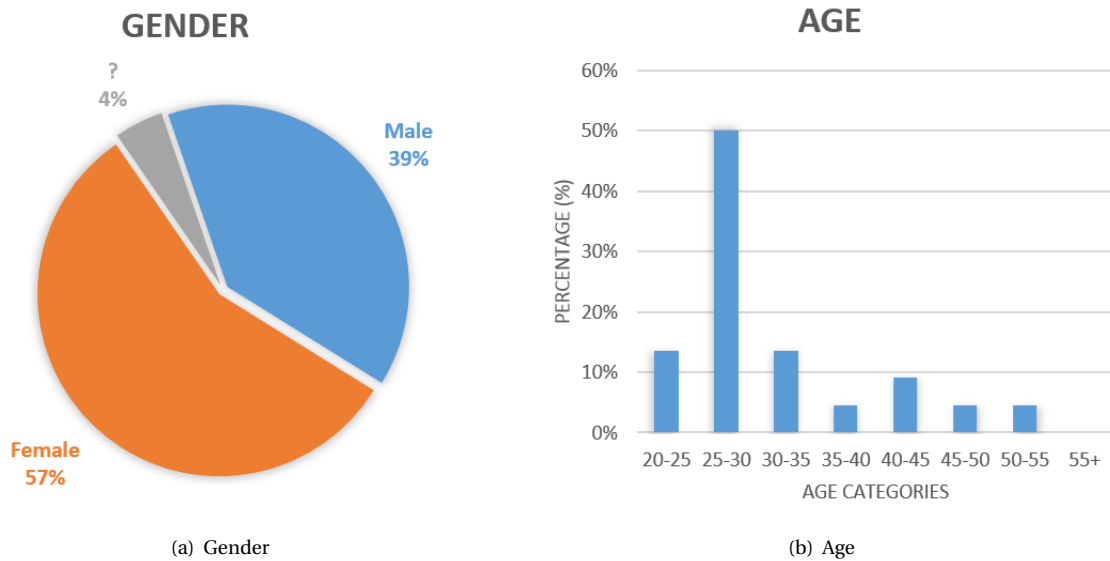


Fig. F6: Gender and age distributions of all users that completed the questionnaire

## General information

The questionnaire was completed by 24 people in the city of Yangon. The gender and age distributions can be found in Fig. F6(a) and Fig. F6(b) respectively. Slightly more female than male are found in the user distribution. In the age graph shows a peak at 25-30 years old which is explained by the fact that most of the users were students. When looking at the spatial distribution of the responses, most of them are located in the most densely populated areas of the city. Unfortunately not the whole city is covered in this survey. Concerning the occupations of the users, it is clear that aside from students there are many business owners, expats and managers.

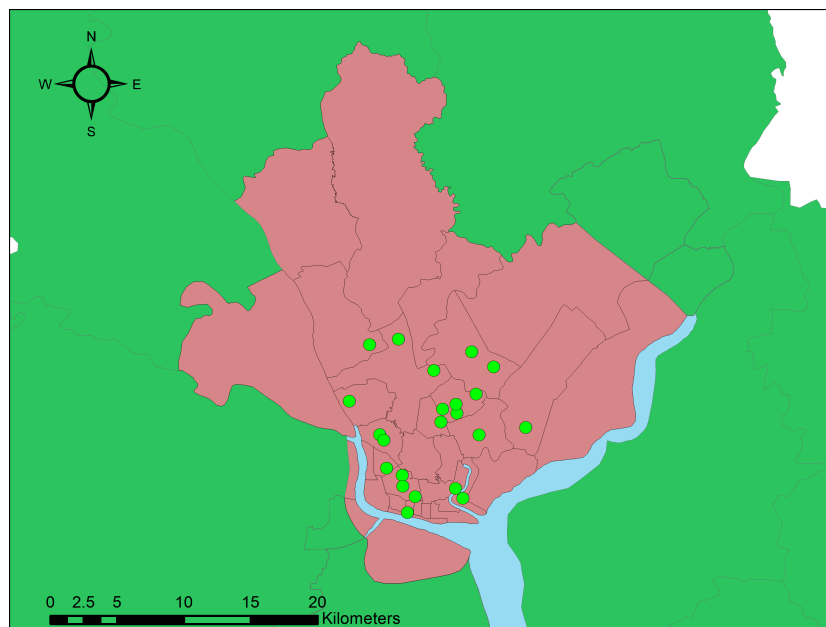


Fig. F7: The outline of the city has been colored in dark pink. The green dots represent the approximate locations of the respondents

## Type of delivery

Some simple graphs show where users receive their water from. Firstly the distribution between YCDC and private supply is shown in Fig. E8(a). More than one in four users receives water from more than one source. For the private use the vast majority relies on groundwater while very little rainwater is harvested and even less rely on surface water by treated or untreated means.

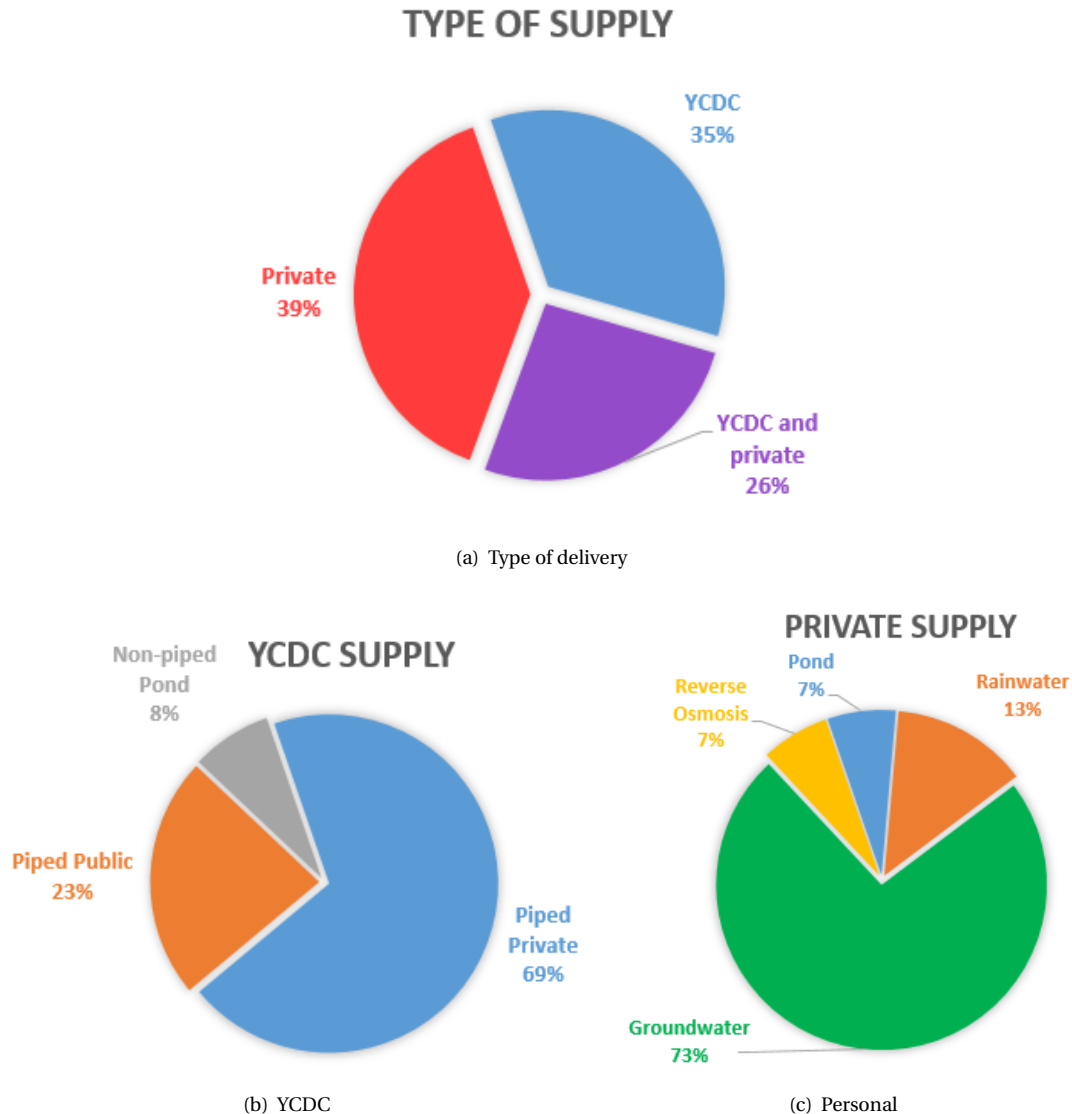


Fig. E8: Distribution of the source of water for all respondents. The Type of delivery (a) is further examined for both YCDC and private supply. The source of the water within the users that receive water from the YCDC is shown in (b). Finally the sources of water within the users that have a private source of water is shown in (c).

Concerning the water availability, most of the users have a very constant supply of water throughout the year. For approximately 15% of the users there is a slight drop in availability in the dry season.

The final indicator for the delivery type was water quality which is shown in Fig. E9. Most of the users receive clear water, but a small amount has slightly murky to quite murky water. Most of the water does not taste salty while in some areas there is quite some more salinity in the water. If water is used for drinking, it is most of the times boiled because it often regards untreated water which can be dangerous for human health.

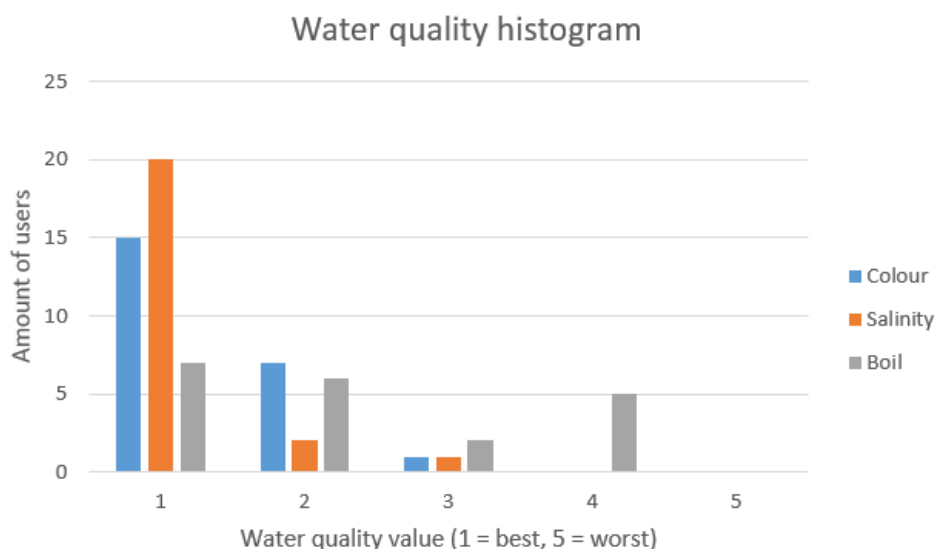


Fig. E9: The water quality expressed as judgement value 1–5 (best quality to worst quality) by all users. The chart shows color, salinity and whether the water is boiled before drinking

## Water demand

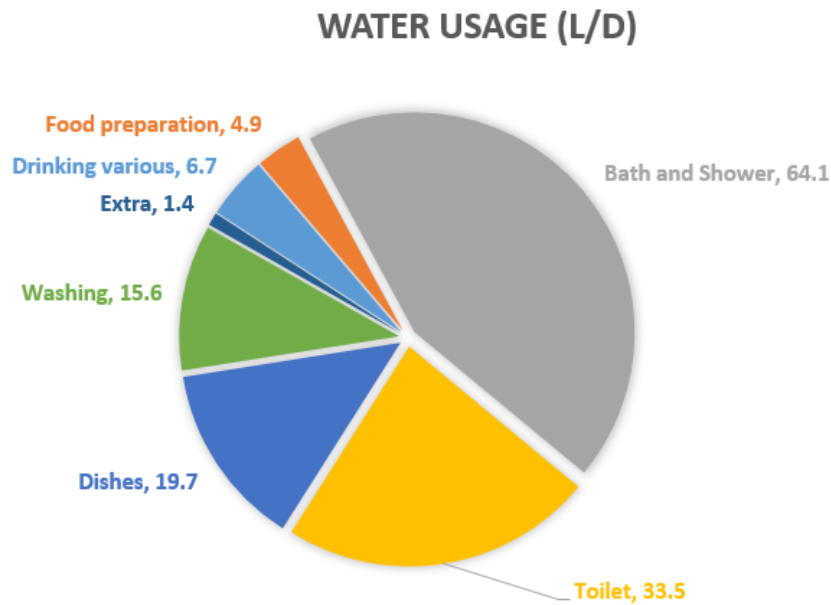
The water demand is calculated per category. The individual results are shown as average value and standard deviation and can be found in Table E2. Bath and shower is by far the dominant category like many other parts in the world. Most notably about the bath and shower category is that most users shower twice a day and because of the tropical climate in Yangon. The standard deviations are calculated for a sample group and since the group is relatively small this means that the standard deviations are quite high. The category extra is composed of the final question of this section where the user could specify additional water usage. For cleaning an average is calculated for all users. For watering the garden and other activities there were only some individuals who answered which is why the deviation is so high.

Table E2: Water demand statistics per category. Average values and standard deviations are shown

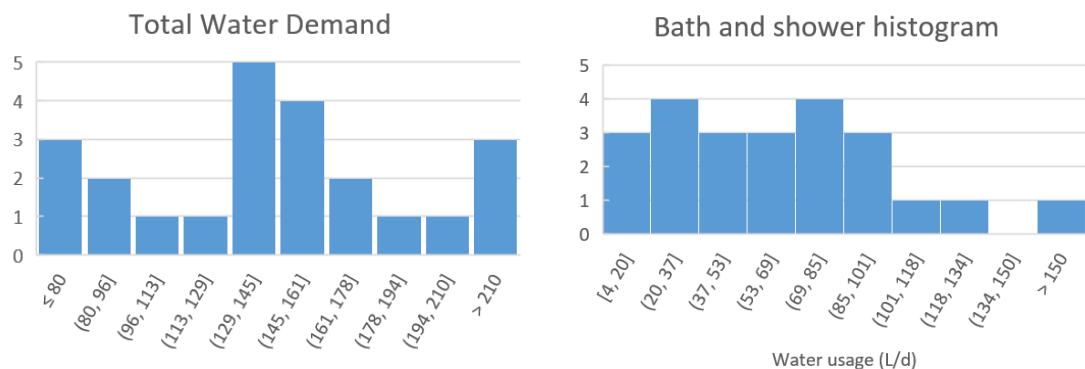
Cat.	Average (L/d)	SD (L/d)
Food preparation	4.9	2.58
Bath and Shower	64.1	43.38
Toilet	33.5	23.50
Dishes	19.7	10.90
Washing	15.6	13.37
Extra	1.4	3.39
Drinking	1.2	0.83
Brushing teeth	1.1	1.37
Sanitary rinsing	4.5	2.39

The results have also been put into a pie chart for convenient visualization. This chart with values in Liter per day is visible in Fig. E10(a). Note that drinking water is combined with teeth brushing and sanitary rinsing. The amount of drinking water is small because most people use bottled water.

A histogram is made for both total water demand and the largest category, 'Bath and Shower'. These histograms can be found in Fig. E10(b) and Fig. E10(c) respectively. There is not yet a clear distribution visible for any of these figures and also a lot of variation is observed.



(a) The average water demand distributed over all assessed categories in Liter per day. Drinking water, teeth brushing and sanitary rinsing has been combined in 'drinking various'.



(b) Histogram for total water demand values. x-axis values are in Liter per day and y-axis shows the number of users

(c) Histogram for water demand in the category 'Bath and Shower'. x-axis values are in Liter per day and the y-axis shows the number of users

Fig. E10: Pie chart of water demand per category and histograms showing the distributions in water demand for total amounts and the bath and shower separately.

## Discussion

Both Fig. E8(b) and Fig. E8(c) show similar results as found in (YCDC & JICA, 2013) and (YCDC, 2014). For the type of supply the previously mentioned documents do not show any overlap for users have multiple sources of delivery while Fig. E8(a) shows that more than one in four users has multiple types of water delivery.

The remark that was most often placed at the 'Type of delivery' section was the fact that users do not drink their water from the tap. Most of the users drink from bottled water gathered by other means than one of their own water sources. For the salinity parameter all users that answered slightly to moderate saline water live in a township adjacent to the brackish river; Kamaryut, Hlaing and Dawbon. Remarkably however, none of them indicated having a private water source.

Another remark was often stated as well: 'Most of the buildings have a water tank up high so water can be pumped up when water and electricity are both available'. Only whenever there is a long time period of

shortage of either water or electricity, there can be a period of water shortage. For these people the variation over the season is not possible to express in flow rate but should rather be expressed in down time of water, electricity or both.

When considering water demand for men and women there are almost no differences visible between total amounts as seen in Fig. E11. The slight anomaly is caused by a difference shower water usage. In one of the final questions in the survey, the user had to indicate if he or she thinks that he or she uses more, the same or less water than the rest of the household. A histogram of these results is shown in Fig. E12. Interesting to see is that the average of these answers is approximately 1.

## WATER DEMAND / GENDER (L/D)

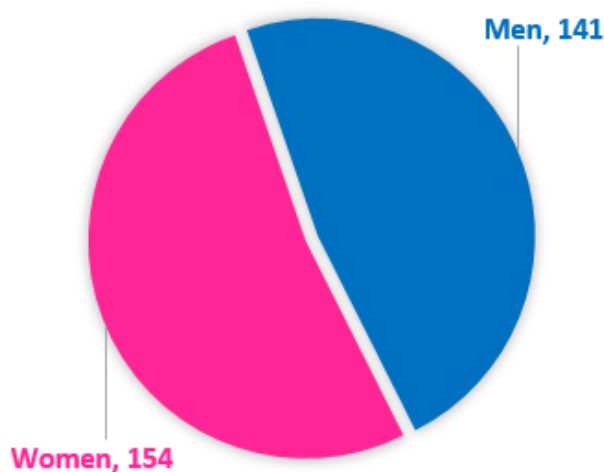


Fig. E11: Total water demand per gender in Liter per day

## MULTIPLIER MORE/LESS

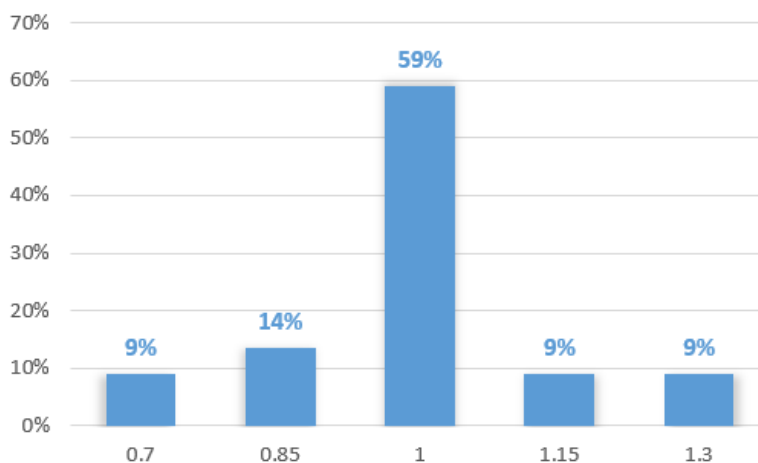


Fig. E12: Histogram of answers to 'I use more, the same or less water than the rest of the household'. A value of 0.7 means that the user thinks it uses up to 30% less water

The final question of the 'Water Demand' section there was a remark about the language of the questionnaire being in English and therefore did not reach only Burmese speaking citizens. While the commentary was

completely justified there was no way of getting around this fact easily. This means that results presented in this survey can be considered as not completely representative for the whole population of Yangon also considering that only 24 users were interviewed.

Generally there is a link between household income and water usage, which is not assessed in this survey, and sources such as (Munian, 2010) tend to find positive correlations between the two. However, the price of water in Yangon is only 0.07 USD/m<sup>3</sup> (JICA, 2014*a*) while surrounding countries have much higher tariffs; Bangkok 0.36 USD/m<sup>3</sup>; China 0.35 USD/m<sup>3</sup>; India 0.18 USD/m<sup>3</sup>; Bangladesh 0.19 USD/m<sup>3</sup>; Vietnam 0.30 USD/m<sup>3</sup> (IB-Net, 2016). Not only is there a low tariff, but there is also a significant amount of non-revenue water delivered (Mon et al., 2013). Therefore it is fair to assume that the water demand is more dependent on availability of water rather than the price of it or the income of the users.

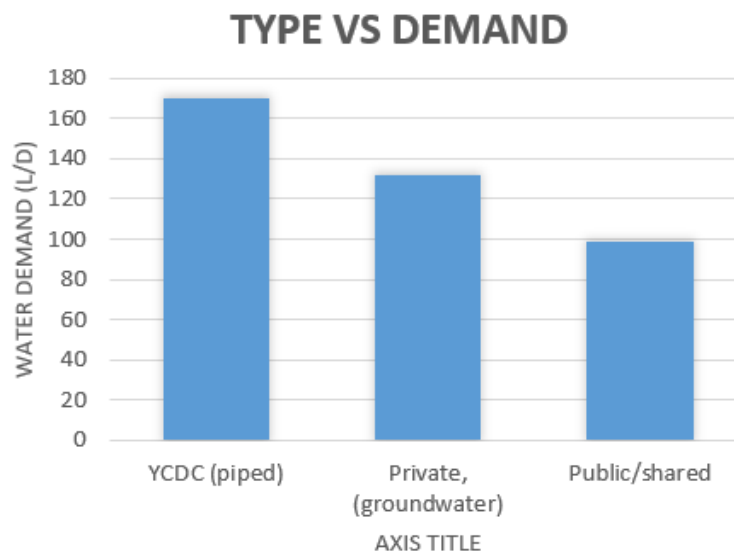


Fig. F.13: The average water demand per category showing the relation between convenience of delivery and water usage. Three categories are considered: YCDC piped water, private groundwater extraction, and public or shared sources. The average water demand in L/p/d per category is shown in each of the labels.

To assess that last assumption that water demand is correlated with the ease to which users receive their water, the demand values are split into three categories: The YCDC piped water, private groundwater extraction, and public or shared sources. In Fig. F.13 the average water demand per category is shown. Clearly there is a very strong relation between the type of delivery and the amount of water that is used on a daily basis.

